Title
PRECISION MEASUREMENT OF THE NEGATIVE PION MASS FROM ITS RADIATIVE ABSORPTION IN HYDROGEN

Author
Crowe, Kenneth Morse.

Publication Date
1952-12-18

UCRL-2050

UNCLASSIFIED

UNIVERSITY OF CALIFORNIA

Radiation Laboratory

Contract No. W-7405-eng-48

PRECISION MEASUREMENT OF THE NEGATIVE PION MASS FROM ITS RADIATIVE ABSORPTION IN HYDROGEN

Kenneth Morse Crowe

(Thesis)

December 18, 1952

Berkeley, California

DISCLAIMER

TABLE OF CONTENTS

PRECISION MEASUREMENT OF THE NEGATIVE PION MASS FROM ITS RADIATIVE ABSORPTION IN HYDROGEN

Kenneth Morse Crowe

Radiation Laboratory, Department of Physics
University of California, Berkeley, California

December 18, 1952

ABSTRACT

The gamma ray spectrum of the reaction

$$\pi^- + P \longrightarrow N + \gamma$$

has been remeasured with an improved design of the high energy pair spectrometer. This design has taken advantage of one of the focusing properties of a 90 degree wedge shaped magnetic field to minimize the effect on the resolving power of multiple scattering of the pair fragments in the converter. The theory of the spectrometer is developed in detail. The accuracy of the energy scale depends on magnetic field measurements and the calculation of orbits, aberrations, and resolving power. The error apart from counting statistics for the energy scale is approximately 5 parts in 10^4. By the determination of the mesic absorption gamma ray energy, a precise mass value for the negative pion has been found.

$$m_{\pi^-} = 273.5 \pm 0.5 \text{ electron masses}$$

From the mass differences already obtained for the neutral pion by Panofsky, Aamodt and Hadley[1] and negative muon by Lederman, Tinlot and Booth[2], it is possible to improve the mass values for the π^o and the μ^- mesons.

$$m_{\pi^o} = 262.9 \pm 2.1 \text{ electron masses}$$

$$m_{\mu^-} = 207.5 \pm 3 \text{ electron masses}$$

If one assumes that the positive and negative pions have the same mass, the mass of the positive muon can also be deduced from the work of Birnbaum, Smith and Barkas.[3]

$$M_{\mu^+} = 207.0 \pm 0.5 \text{ electron masses.}$$

PRECISION MEASUREMENTS OF THE NEGATIVE PION MASS FROM ITS RADIATIVE ABSORPTION IN HYDROGEN

Kenneth Morse Crowe

Radiation Laboratory, Department of Physics
University of California, Berkeley, California

December 18, 1952

I. INTRODUCTION

A. Survey of Meson Mass Measurements

The discovery of the intermediate particle of mass between that of the electron and proton in both cosmic ray[4] and accelerator studies was based on the determination of its characteristic mass.

The techniques of identifying mesons by measuring masses have also evolved into experiments whose object is to make precision determinations of various meson masses. In this type of experiment, the masses of the three pions and two muons have been determined.

The energetics of the production and interaction reactions of pions provide methods of determining masses, if one is assured that the particles involved are properly identified. The production of positive mesons from proton-proton collisions and the radiative capture of negative mesons by hydrogen have yielded independent accurate mass measurements of the pions.

The energetics of the decay reactions of pions and muons also furnish relations between the masses. It should be remarked that these experiments have a dual interpretation. If the reaction is assumed to be known, the mass relations are determined. On the other hand, if one assumes the masses to be known one can study the assumptions involved in describing the reaction. In most cases it is necessary to make both analyses. The justification for this procedure is, of course, connected with the consistency of the mass measurements as obtained in all of these experiments, as will become apparent in the following discussions. We shall discuss these measurements in the following section in some detail.

The theory of elementary particles on the other hand, has yet to predict the particle masses with corresponding accuracy although several interesting attempts will be discussed briefly.

There are a number of techniques used in the identification of pions and muons, from which estimates of masses are obtained, that involve only the electromagnetic interactions of the mesons. The unique dependence of momentum, range, multiple scattering and ionization loss on the mass and velocity indicates that any pair of these quantities would be sufficient to fix the mass. In practice however, only a few combinations have yielded precise mass measurements.

Experiments by Brode and collaborators,[5-7] using cloud chambers in connection with cosmic ray studies, measure masses by the simultaneous determination of momentum and range. The arrangement is shown in Fig. 1. A particle enters the experimental apparatus from above, passes through the counters A, B, and C, is deflected by the magnetic field in the top chamber and stops in the second cloud chamber, where absorbers are placed. The cloud chambers are expanded when a coincidence of Geiger tube pulses occurs. Photography of the tracks gives a determination of the radius of curvature ρ and the range of the particle R.

The momentum

$$pc = \frac{Mc^2}{\sqrt{1 - \beta^2}} = ze\,H\rho \qquad (1)$$

The alternative method of determination is in the measure of the deflection angle θ due to the magnetic field located between the cloud chambers at D.

$$\Delta\theta = \frac{\int H ds}{H\rho} \qquad (2)$$

The range can be calculated from the ionization loss

$$R_{M,z}(E) = \int_{Mc^2}^{E} \frac{1}{-\left(\frac{dE}{dx}\right)}\, dE = \int_{o}^{\beta} \frac{1}{\left(-\frac{dE}{dx}\right)} \frac{dE}{d\beta}\, d\beta \qquad (3)$$

$R_{M,z}$ is the range of a particle of rest mass M and charge z, whose relativistic energy is E.

$$\frac{dE}{d\beta} = Mc^2 \gamma^3 \beta \qquad (4)$$

Where β is the relativistic velocity, Mc^2 is the rest energy of the particle, and

$$\gamma = \frac{1}{\sqrt{1 - \beta^2}}$$

The ionization loss is, apart from small corrections

$$\frac{dE}{dx} = \frac{4\pi e^4 z^2 NZ}{mc^2\beta^2} \left\{ \log \frac{2mc^2\beta^2}{I_o(1-\beta^2)} - \beta^2 + \ldots\ldots\ldots \right\} \qquad (5)$$

$$= z^2 f(\beta) = z^2 f'\left(\frac{E}{M}\right)$$

NZ is the number of electrons per unit volume of the stopping material. I_o is the mean ionization potential in the material. mc^2 is the electronic rest energy. The constants which do not involve the particle being measured are lumped in $f(\beta)$

$$R_{M,z}\left(\frac{E}{M}\right) = \frac{M}{z^2} \int_o^\beta \frac{\gamma^3 \beta}{f(\beta)} = \frac{M}{z^2} F(\beta) = \frac{M}{z^2} F'\left(\frac{E}{M}\right) \qquad (6)$$

From the range-energy relation, one can solve for the range in terms of the curvature for various masses of particles by elimination β between Eqs. 1 and 6.

One cloud chamber event can be represented by a point in a plot of R vs. ρ and this relation in principle uniquely determines the mass. All the points should lie on a line for a given mass. The uncertainties in both ρ and R lead to considerable straggling as seen from the actual data, shown in Fig. 2. The main sources of this straggling are the uncertainties of the momentum due to the distortion effects of

turbulence in the cloud chambers, multiple Coulomb scattering along the path,[8] and errors of photography. The uncertainty in the range is minimized by using many thin adsorber plates. The results obtained by different experimenters are listed in Table I.

A series of experiments by Gardner and his collaborators,[3, 9-13] using the Berkeley 340 Mev proton synchrocyclotron, furnished the early mass data of the artificially produced pions as well as the muons. The method is similar in principle to the cosmic ray muon mass determination. Positive and negative pions are produced by the internal proton or alpha beam striking a small target, usually carbon. Positive pions which stop in the target give rise to positive muons. These mesons are bent in the cyclotron magnetic field through a channel which is designed to allow particles of a small momentum range to come from the target and enter the nuclear emulsion plates. Figure 3 shows a typical target arrangement. The early experiments consisted of measuring the range of these tracks in the plates, and by knowing the entrance angle, the field, and the geometry of the apparatus, one ascertains the momentum of the meson. From Eq. 6 the relation between the range and energy can be written

$$R = \frac{M}{z^2} F''\left(\frac{T}{M}\right) \tag{7}$$

where T is the kinetic energy. Expressing this as a power law over a small range in energy

$$F''\left(\frac{T}{M}\right) = K\left(\frac{T}{M}\right)^{1/n} \tag{8}$$

one can write equation 7 as

$$T = K M^{1-n} R^n z^{2n} \tag{9}$$

The constants n and K can be determined by measuring the range in the emulsions of protons of the corresponding known velocities. n is

approximately 0.581. The energy in terms of an equivalent radius of curvature ρ from Eq. 1 is, in the non-relativistic approximation:

$$T = \frac{(pc)2}{2Mc^2} = \frac{1}{2}\,\frac{z^2e^2}{Mc^2}\,(H\rho)^2 \qquad (10)$$

Solving these two equations for M one obtains:

$$M = z^{\frac{2(1-n)}{2-n}} \left[\frac{(eH\rho)^2}{2KR^nc^2}\right]^{\frac{1}{2-n}} \qquad (11)$$

If one assumes the charge to be equal to the electronic charge, the mass can be evaluated by determining the equivalent radius of curvature of the particles' orbit and its range R in the emulsion.

The early experiments of this type were subject to considerable uncertainty in the calibration of the meson ranges due to emulsion shrinkage, moisture content, etc. The range-energy relations had been calculated using the known composition of the emulsion. Although the experimental range-energy calibration in photographic emulsions have been measured in the range in question, the error of these relations appeared as contributing to the systematic error in the mass.

A refinement of this method was made by using an additional target as a source of protons of nearly the same velocity as the meson being selected so that there would be no specific dependence upon range-energy relations. The experimental set up for this later method is shown in Fig. 5. The meson and proton trajectories are shown passing through separate entrance collimators. The method can be adapted for measuring the ratio of masses of positive pions and muons by again choosing the same velocity for each type meson coming from different targets. The positive muon is assumed to decay from pions at rest in the muon target.

The procedure for handling the data shows the main features of the experiment. Equation 6 can be rewritten in terms of momentum

as follows:

$$\frac{R_\pi}{M_\pi} = K' \left(\frac{p_\pi}{M_\pi}\right)^q \tag{12}$$

$$K' = \left(\frac{1}{2K}\right)^{\frac{1}{n}}, \quad q \doteq \frac{2}{n} = 3.44 \pm 0.05$$

In order to determine the constant K', the equation can be solved for K' with the range and momentum values from the proton tracks.

$$K'_i = \frac{R_{P_i}}{p_{P_i}^{-q}} \; M_{P_i}^{q-1} \tag{13}$$

The distribution of K' will be the range straggling distribution together with the uncertainties introduced from determining ρ. The r.m.s. width of the proton distribution is ~2 percent. From the value of K' obtained over a small region of the plate the pion mass can be calculated from Eq. 12:

$$M_{\pi_i} = \left[\overline{K}' \frac{p_{\pi_i}^{q}}{R_{\pi_i}}\right]^{\frac{1}{q-1}} \tag{14}$$

The r.m.s. width of the range distribution in R_π is ~ 4 percent.

From this one can see that the mean value of the mass is

$$\overline{M}_\pi = M_P \left[\frac{\overline{R}_P}{\overline{R}_\pi} \; \frac{\overline{p}_\pi}{\overline{p}_P}^{\,q}\right]^{\frac{1}{q-1}} \tag{15}$$

For orbits in a magnetic field the momentum ratio is independent of the absolute value of the field in the approximation that the uniformity of the field does not vary rapidly. For the mass ratio, the uncertainty in the experimental value of q is also not a significant source of error.

This method is limited fundamentally only by the range straggling of the meson which is due to statistical fluctuations in the ionization loss.

The distribution of track lengths for μ endings from π-μ decays in the emulsion can be compared with the meson range distribution. The fit of the range distribution serves to check the influence of background mesons which do not originate from the assumed target point. The histograms of track endings are shown in Fig. 5. The ratios of π^+/P and π^-/P and the ratio of π^+/μ^+ derived from these experiments are given in the mass table.

The other general methods[14] which have as yet yielded at best approximate mass information are the range ionization method or grain counting technique[15,16] of nuclear emulsion and the range-multiple scattering method.[17] The results of these methods are included for comparison in the mass table. (Table I.)

The energetics of the π^+-μ^+ decay at rest

$$\pi^+ \longrightarrow \mu^+ + \nu$$

allows a precise evaluation of the π^+-μ^+ mass difference if one assumes the third particle to have zero rest mass. The kinetic energy or in this case the momentum of the μ^+ meson can be determined in the same experimental plates that the π^+/μ^+ ratio is measured. One can solve for the π^+-μ^+ mass difference

$$M_\pi c^2 - M_\mu c^2 = 2\, p_o C \left(\frac{1}{1 + \frac{M_\mu^+}{M_\pi^+}}\right) \qquad (16)$$

where p_o is the decay momentum and the mass ratio M_μ^+/M_π^+, is measured in the comparison method, Eq. 15.

To determine the momentum of the μ^+, the following procedure can be followed. The distribution in range of the meson decay in the plate, R_{p_o}, is measured and the mean value obtained. Equation 12 shows that if we solve for the ratio of R_{p_o} to the range R_{p_i} a meson of momentum p_i which comes from the target where $p_i \leq p_o$, we have

$$\frac{R_{p_o}}{R_{p_i}} = \left(\frac{p_o}{p_i}\right)^q \text{ or } p_o = p_i \left(\frac{R_{p_o}}{R_{p_i}}\right)^{\frac{1}{q}} \qquad (17)$$

This is true providing we take events in the same portion of the plate so that $K_{p_i} = K_{p_o}$ and that R_{p_i} is not very much less that R_{p_o} so that the uncertainty in the value of q is not a significant source of error. The basic accuracy of the value p_o obtained depends in this case upon the distributions of both R_{p_o} and R_{p_i} as well as the analysis of the orbit in the magnetic field. The π^+-μ^+ difference has been obtained to high accuracy as shown in Table 1. The effect of the finite mass of the neutral particles in the decay reaction has been examined, and it is possible to set an upper limit of a few electron masses. The latest limit for the ν mass is given in Table 1.

The application of the Gardner technique to negative μ's is limited due to the predominance of pion capture over decay in most target materials as well as the reduced negative pion yields in the proton beam. However, the μ^- mass has been determined accurately in an experiment of Lederman and collaborators.[2] Here the decay of π^- in flight is studied in a cloud chamber with a magnetic field. From the momenta and the angle of the decay, the pion-muon difference can be obtained. The relation is as follows:

$$M_\mu c^2 = \Big\{ M_\pi^2 c^4 + 2 p_\pi^2 c^2 - 2 p_\pi c p_\mu c \cos\theta - 2\sqrt{(M_\pi^2 c^4 + p_\pi^2 c^2)(p_\pi^2 c^2 + p_\mu^2 c^2 - 2 p_\pi^c \cos\theta)} \Big\}^{1/2}$$

The value of the mass obtained in this manner agrees favorably with the positive muon accelerator results and cosmic ray values.

The decay of the μ meson proceeds as follows:

$$\mu^+ \longrightarrow \beta^+ + 2\nu \qquad (19)$$

Since the energetic upper limit, W, is determined by the rest masses of the particles, it is in principle possible to determine the μ^+ mass in a precise manner, if one assumes the neutral particles to have zero rest mass.

$$W = \frac{M_\mu^2 - m^2}{2 M_\mu} \qquad (20)$$

The β spectrum when measured with any finite resolving power spectrometer will have its end point shifted an amount which depends upon the detail of the spectrum at the high end. Tiomno and Wheeler,[18] Michel,[19] and others, have discussed the theoretical values for this intercept, and it is clear that the values quoted as μ^+ mass measurements must be qualified until better data exists.[20] The effects on the mass of this type are easily of the order of a few percent with the resolutions used. The effect of a finite mass M_ν for one of the neutral particle is to reduce W by an amount $\sim M_\nu^2/2M_\mu$. It is apparent that the limits on M_ν obtained experimentally are extremely wide.

Richman and Cartwright,[21] and independently Peterson, Iloff and Sherman,[22] in the study of the energetics of the reaction

$$P + P \longrightarrow \pi^+ + D \qquad (21)$$

have obtained the positive pion mass.

The Q of the reaction is measured by determining the kinetic energy of the pion and the bombarding proton energy. Mesons produced by the external proton beam of the Berkeley cyclotron were used by these groups. The energy spectrum measured at zero degrees Lab angle is shown in Fig. 6. The energy of the proton beam was measured in two ways. For Cartwright's experiment, Mather measured the velocity of the proton beam by using its Cerenkov radiation. Peterson used the range of the beam in copper, as measured with an ionization chamber. These two methods have been cross checked by Segrè and Mather,[55] and the range energy relation of both mesons and protons have been corrected accordingly. Therefore the accuracy of both measurements of proton energy rest on a Cerenkov method. The experimental details of the two measurements were different. Cartwright used polyethylene targets with mesons coming off at 0° in the Lab. system. They are bent through ~90° and enter aluminum absorbers in which emulsions have been embedded. Peterson used liquid H_2 targets with mesons coming off at 18° in the Lab. system. The magnet separator was designed for an angle of 20° and the emulsions are embedded in copper absorbers. The position of the track ending is used to determine its energy within the range straggling.

The spectrum has been analyzed to determine the expected shape. Within the statistical accuracy, the workers claim that one obtains a good fit when beam spread and range straggling have been included and that the effect of the reaction

$$P + P \longrightarrow \pi^+ + N + P \qquad (22)$$

has a negligible effect upon the π^+ mass determination. Details of the peak are shown in Fig. 8.

The results of both determinations are listed in Table 1.

The π^- capture gamma ray in hydrogen provides another independent measurement of the meson mass.[1] In this experiment, negative pions produced by the cyclotron are slowed down and captured from the K shell in hydrogen. The "excited state" of the neutrom emits a gamma ray of ~130 Mev. The gamma ray is related to the meson mass by the relation:

$$E_\gamma \doteq M_\pi c^2 - \frac{E_\gamma^2}{2 M_N c^2} - (M_N - M_P) c^2 \qquad (23)$$

The gamma ray energy is measured by use of a pair spectrometer. This instrument consists of a converter to produce electron positron pairs, a magnetic field to separate and sort the pairs by the momentum of the fragments, and suitable counting apparatus to record the events and classify the energy. The first measurements of this event were done with extremely broad resolution 22.5 percent width at half maximum. Since the pair fragments come within an angle mc^2/E, the angular divergence of the pair fragments is determined primarily by multiple scattering in the converter. One can consider the field as providing an angular bend of the pair fragments from the beam direction. The early spectrometer used was a small square with a bending angle $\phi = 90^o$. A set of proportional counters served as detectors, and a multi-channel coincidence circuit served as sorter and recorder. The results of the early instrument yielded an apparently continuous spectrum as the magnetic field was raised, as shown in the spectrum, Fig. 9. We shall

in the following sections consider the various improvements of this experiment in detail, the present research being the most recent attempt.

The measurements of γ-rays which results from the supposed decay of π^o mesons have led to several mass values for the neutral pions.

Carlson, Hooper and King,[23] have measured the energy of γ-rays in cosmic ray stars at high altitudes by looking for gamma ray produced pairs in emulsions close to the stars. By measuring the multiple scattering of these pairs, they obtain the energy of the gamma ray.

The spectrum of these events allows an estimate of the neutral pion mass as a result of the following analysis. The Doppler effect of the γ-ray emitted at an angle θ_c in the pion rest frame moving at a velocity β produces an energy shift so that in the laboratory the energy

$$E_L = \frac{M_{\pi^o} c^2}{2} \gamma (1 + \beta \cos \theta_c) \qquad (24)$$

Assuming that the spontaneous decay of neutral pions is isotropic in the pion rest frame, one observes in this frame the number of gammas per pion in an angle $d\theta_c$

$$dN = \frac{2d\Omega}{4\pi} = 2 \frac{\sin \theta_c}{2} \, d\theta_c \qquad (25)$$

However, the energy increment of the gamma rays from a monochromatic pion beam in the same angle $d\theta_c$ is

$$dE_L = \frac{M_{\pi^o} c^2}{2} \gamma \beta \sin \theta_c d\theta_c = \frac{\gamma\beta}{2} M_{\pi^o} c^2 \, dN$$

$$\frac{dN}{dE_L} = \frac{2}{\gamma \beta M_{\pi^o} c^2} \qquad (26)$$

That is, the intensity will be independent of the angle of decay. The energy spectrum will be flat if it is obtained by integrating the intensity spectrum over all the π^o decay angles. The last condition is automatically fulfilled if the π^o's are isotopically produced. The spectrum will go from

$$E_{min} = \frac{M_{\pi^o} c^2}{2} \gamma (1-\beta) \text{ to } E_{max} = \frac{M_{\pi^o} c^2}{2} \gamma (1+\beta) \qquad (27)$$

From this one has a simple relation that

$$E_{min}\, E_{max} = \left(\frac{M_{\pi^o} c^2}{2}\right)^2 \gamma^2 (1-\beta^2) = \left(\frac{M_{\pi^o} c^2}{2}\right)^2 \qquad (28)$$

Thus one can imagine the spectrum of γ-rays as a composition of rectangles whose end points satisfy this equation, the height of which depends upon the velocity spectrum of neutral mesons produced. If one has such a spectrum, one can measure the neutral pion rest mass by computing equation 28 for each velocity group. The constancy of the value is a measure of the purity of the source as well as a check of the method. The spectrum obtained from cosmic rays is shown in Fig. 10.

It is necessary to know the low energy points with high accuracy to obtain a mass value. Clearly the statistics of this edge is extremely important for establishing an error of the mass measurement. The value obtained in the cosmic ray work $M_{\pi^o} = 295 \pm 20$ electron masses has been considered to be evidence for the similarity of the observed events with the results obtained with artifical mesons.

A measurement of the spectrum of gamma rays from 340 Mev protons on various targets has yielded a mass value for the π^o which depends upon the analysis of the neutral meson produced in the target which decay into two photons. A pair spectrometer was used in this work and the description of the instrument is found in Section I-B. The data are shown in Fig. 11. This value by recent measurements of Crandall,[24] under this assumption, given $M_{\pi^o} = 280 \pm 10$ electron masses. The discrepancy between this mass value and one obtained by a more accurate method implies that at least a small fraction of the γ-rays are due to other sources.

In the case of the absorption reaction of slow mesons,

$$\pi^- + P \longrightarrow N + \pi^o \qquad \pi^o \rightarrow 2\gamma \qquad (29)$$

it has been possible to establish that the energy spectrum agrees with the predicted result and that two gamma rays are produced in coincidence with the meson coming to rest in the hydrogen. Sachs and Steinberger

have shown that the angular correlation also agrees with the expected result.[25] It therefore seems that the gamma ray spectrum analysis from this process very probably arises from the assumed reactions. From the kinematics it has been shown that the width of the spectrum is extremely sensitive to the difference of the negative and neutral pion rest masses. The spectrum has been measured with the pair spectrometer that is considered in detail in Section I-B. The mass difference obtained is to a large extent independent of the precise energy scale and the uncertainty in the value predominantly statistical. It is clear that with the improved value of the negative pion mass, an improved measurement of this spectrum would be desirable. Figure 12 shows the composite spectrum of the best single gamma ray spectrum and previous neutral meson decay spectrum of Panofsky and co-workers.[1]

A comparably accurate value of the $\pi^- - \pi^o$ mass difference can be made by a precise measurement of the angular correlation of the two gamma rays from the exchange capture reactions. (Equation 29.) This arises since the relativistic abberation of the decay photons is also sensitive to the pion kinetic energy and hence the mass difference. The maximum abberation angle is approximately 22^o.

It should be remarked at this point that in all considerations involving electromagnetic interactions the charge of the mesons has been assumed to be the electronic charge. There are two direct experiments bearing on this point and a number of indirect but general arguments with support this assumption. From the ratio of drop counts obtained from cloud chamber tracks of minimum ionization mesons and electrons, the charge can be evaluated:[26, 27]

$$z = 1.02 \pm 0.03 \text{ in hydrogen}$$

$$z = 1.005 \pm 0.02 \text{ in helium}$$

$$z = 1.017 \pm 0.03 \text{ in argon.}$$

The charge can be determined also by comparing mass values obtained by methods which have a different dependence upon

charge. Bowker's[28,13] grain counting method and the Gardner method can be compared to show:

$$z = 0.99 \pm 0.03$$

The more general arguments involve the conservation of charge in all of the reactions in which mesons are involved. The possibility of a light particle with a small charge being involved with pion reactions is most unlikely since the excitation energy observed, for example in π^- stars, is of the order of the rest energy of the pion. An additional particle would reduce the excitation as is evident in μ^- stars where the average excitation is of the order 10 percent of the rest energy. One would certainly have difficulty constructing, for the two body process, a consistent alternative which involves a third particle, i.e.

$$\pi^- + P \longrightarrow \gamma + N + \text{"}\gamma\text{"} \qquad (30)$$

for which the gamma ray spectrum would still be sharply peaked. One can compare directly the mass obtained in two body reaction with the latest results of the Hρ range comparison of Smith, et al.[12] in which the charge appears directly. The result indicate that

$$z = 0.991 \pm 0.007$$

This would, on the surface, be an impressive improvement on the limit for the deviation of the charge from the electron charge. The limit is, however, not free from the logical criticism that in evaluating the mass from the capture gamma ray energy we have assumed that the reaction is a two particle reaction, where with the exception of the meson the charges are all known. Although the consequences of assuming other possible reactions have not been thoroughly investigated, it is maintained that this limit should receive some weight in the consideration of the charge. Further, one can argue that the energetics and line width of the capture gamma ray process alone should also be taken as evidence that the reaction proceeds in the manner assumed.

B. Previous Meson Capture Gamma Ray Work

The experiment of Panofsky, Aamodt, and Hadley,[1] on the gamma ray spectrum resulting from capture of negative pions in hydrogen and deuterium, provides an accurate method of measurement of the negative meson mass. The geometry of the experiment can be seen from Fig. 13. The 330 Mev proton beam produces negative pions at the wolfram target. The negative pions come to rest in the high pressure hydrogen vessel and the capture gamma rays are observed. It is assumed that the reaction studied is:

$$\pi^- + p \longrightarrow N^* \longrightarrow N + \gamma \qquad (31)$$

If the pion is captured from the K shell

$$E_\gamma = M_{\pi^-}c^2 - \left[\frac{E_\gamma^2}{2M_N c^2} - \frac{1}{8}\frac{E_\gamma^4}{(M_N c^2)^3}\cdots\right] - \frac{\alpha^2}{2} M_\pi c^2 - (M_N - M_P)c^2 + \cdots \qquad (32)$$

where the second term takes into account the recoil energy of the neutron. The third term is the energy of the pion in the mesonic Bohr orbit, K shell, which is negligible for this work. The fourth term comes from the N, P mass difference the value of which is well known. The purpose of this research is to extend the accuracy of the method to provide a precision measurement and to search for any fine structure present in the line. The previous gamma ray measurement is similar in many respects to the method used in the current determination. The difference between the two experiments lies in the design of the spectrometer. In order to compare the results, we will first consider the major features of the previous design.

The pair spectrometer used is shown schematically in Fig. 14. The γ-rays produce pairs at the tantalum converter. The energy of the electron and positron is determined by measuring their momenta by recording the Geiger channels through which the particles pass. The energy calibration is made from the measured magnetic field and calculated orbits. The data is combined using the known fragment distribution, and the geometrical counting efficiencies for various gamma energies.

The gamma ray measurement included the following main sources of error.

1. Statistics in the fit of the spectrum ± 2. 2 em or
2. Field and geometry uncertainties ±1. 2 or total of ±2. 5 em.

For a given number of counts the size of the statistical error is given in terms of the resolving power of the pair spectrometer.

Figure 15 gives the data and theoretical resolving power of the instrument adjusted for the central value pion mass.

It is clear that if it were possible to reduce the width of the resolving power a reduction of the percentage error in the determination of the determined meson mass would be possible. The resolving power of the spectrometer was due to three major effects: 1. The finite channel width. 2. Multiple scattering of the pair fragments in the converter. 3. The radiation of the electrons in the converter.

We shall discuss each of these briefly.

The channel width resolution results from the finite size of the Geiger tubes which form the energy channels. The effect on a monochromatic γ-ray would be to produce a triangular resolution of width at half maximum equal to the energy width of the counter. (Fig. 16.)

The multiple scattering[29] in the converter of the pairs produces an energy broadening due to the geometry of the orbits in the spectrometer. One can show that

$$\Delta E_{RMS} = K\rho\, \Delta\theta_{RMS} = E \cdot \frac{21}{E}\sqrt{\frac{t}{t_o}} = 21\sqrt{\frac{t}{t_o}} \qquad (33)$$

is the mean scattering width independent of energy, and of the order 2. 5 Mev in the previous work. Actually, the pairs produced at different thicknesses have different resolving widths so that by combining the Gaussian scattering for increments in t one obtains a peaked curve as shown in Fig. 17.

The radiation[30] of electron pair fragments also tends to decrease the observed gamma ray energy which has the effect on the resolving power as shown in Fig. 18. When one combines these successively, one obtains the resolution curve shown in Fig. 19.

The actual method of computation of these steps will not be dealt with here, since the basic method is carried out in detail for the focusing spectrometer case in Section V-C.

It will be seen that in the table of masses, Table 1, the entry for Panofsky's method has been entered twice. The first value, 275.2 ± 2.5 electron masses, is the one stated in the paper. The second value, ~ 278 electron masses, has been deduced from the same data with several small corrections which have been found in the process of analysis of the focusing spectrometer. The major error was the omission of the effect of ionization loss of the outgoing pair fragments.

In applying the corrections, such as the ionization loss correction, which are dependent upon the thickness of the converter, the effective thickness is reduced due to losses arising from multiple scattering in the vertical direction. This will again become apparent in the analysis of the precision spectrometer. The effect upon the mass can be estimated from the results obtained in the present work and the effective converter thickness is approximately 15 percent less than the total converter.

The higher order effects due to the non-uniform magnetic field cannot be easily estimated in this experiment. On the basis of the calculation for the precision spectrometer one would estimate a maximum positive correction to be~0.5 Mev or~1.0 electron masses. This correction has not been applied in the table for the following reasons. The pole tip and hence the field for which this correction was calculated was not used in the early measurements. The one used was different in two respects. The gap was changed (Panofsky, et al.[1] 3-1/2", Crowe 4"). In addition a set of magnetic shields were used to shield the Geiger tubes. Without remeasurement of the field it would be difficult to estimate the field gradients in the region of these shims.

The uncertainty of this correction is certainly of the order of the correction itself.

C. The Theory of Meson Masses

From the historical point of view the prediction of the meson by Yukawa[31] was based upon an attempt to explain short range nuclear forces. By application of the relativistic wave mechanics to the nuclear force field, it can be shown that the range $\lambda\!\!\!^{-}$ in potentials of the form

$$V(r) = \frac{g^2}{r} e^{-r/\lambda\!\!\!^{-}} \tag{34}$$

can be identified with the Compton wavelength of a meson of mass M.

$$\lambda\!\!\!^{-} = \frac{\hbar}{Mc} \tag{35}$$

If these heavy quanta of the potential field are associated with pions, one would expect that the pions rest mass should be a fundamental parameter of a successful theory of nuclear forces.

The proton-proton scattering data, for example, when analyzed with the Yukawa potential gives an equivalent meson mass[32] 333 ± 2 m. The n-p data[32], on the other hand, gives a mass in the singlet and triplet interactions.

$$M_T = 274 \pm 12 \text{ m} \qquad M_S = 365 \pm 80 \text{ m} \tag{36}$$

Hart and Hatcher[33] have recently attempted to adjust the p-p potential with a potential of the form

$$(1 - e^{-\frac{r}{r_o}}) \left(\frac{e}{r} - \frac{g^2}{r} e^{-\frac{r}{\lambda\!\!\!^{-}}}\right) \tag{37}$$

where it turns out by choosing the constant γ_o to be the classical electron radius, the equivalent meson mass can be lowered to 274 m.

The method of formulating a unified theory for the many masses of elementary particles has been the subject of preliminary theoretical investigations. Born summarized the futility of the situation by remarking that one cannot continue inventing new field equations if it is probable that there is an infinite number, which seems to be not an extravagant extrapolation. The problem then involves building a theory for quantizing the mass values which may be used to predict the mass spectrum that is being discovered.

The usual procedure in this work is to assume that when the distances under consideration are less than r_o, the classical electron radius, the usual equations of relativistic quantum mechanics are inadequate and that they must be modified or generalized. The problems involved are for the most part building a formalism of interactions in which several masses of particles appear consistent with the known facts. In the following summary, only the conclusions or predicitions of the various workers will be stated.

From the theory of special relativity the invariant length of the energy momentum tensor reduces to the rest mass in the rest frame of a particle.

$$p^i p_i = Mc^2 \tag{38}$$

By the correspondence principle one is led to a wave equation

$$\left[\frac{\partial^2}{\partial x_i^2} - \left(\frac{Mc}{\hbar}\right)^2\right] \psi = g \tag{39}$$

where g is the source strength or density to conform to the usual notation

$$\Box = \Sigma \frac{\partial^2}{\partial x_i^2} \quad \text{and} \quad k = \frac{Mc}{\hbar} = \frac{1}{\lambda\!\!\!^{-}} \tag{40}$$

$\Box$ represents the d'Alembertian operator and k is the reciprocal

compton wave length. The equation which results is the Klein-Gordan equation

$$(\Box - k^2)\psi = g \tag{41}$$

One might analogously consider the generalized equation of the form

$$F\left[\Box, K_i\right]\psi = \rho \tag{42}$$

to be a description of the mass sources ρ where the K_i would be proportional to the rest masses. Depending upon the chosen properties of F, various mass spectra may be predicted. The reciprocity theory of Born[34] assumes that the laws of nature are invariant under the transformation:

$$\begin{aligned} x_k &\longrightarrow p_k^* \\ p_k &\longrightarrow -x_k^* \end{aligned} \tag{43}$$

For illustration we see that by factoring the Planck constant into two parts

$$\hbar = ab \qquad a = \eta \frac{e^2}{mc^2} \tag{44}$$

where a is a length of order of the electron radius, $\eta \sim 1$, and the quantity b is a characteristic momentum. This quantity can be introduced into the formalism to be associated with the meson mass.

In order to arrive at a dimensionless equation, let us assume that distances are measured in units of a

$$X_i = \frac{x_i}{a} \tag{45}$$

One can write the Klein-Gordon equation in dimensionless form

$$\left[\Sigma \frac{\partial^2}{\partial X_i^2} - (ak_j)^2\right]\psi = \left[\Box - K_j^2\right]\psi = \rho \tag{46}$$

$$ak_j = K_j = a\left(\frac{Mc}{\hbar}\right) \qquad (47)$$

The mass M would therefore be related to the eigen value K_j of Eq. 46

$$M = K_j\,(\hbar/ac) = \frac{K_j}{\eta}\,\frac{m}{e^2/\hbar c} = \frac{K_j}{\eta}\;137\;m \qquad (48)$$

Born is led to a series of values for the constants K_j and η. K_j varies around 1.41 and the values it turns out, are related to the roots of the associated Laguere polynomials. There are of course an infinite number of meson masses from which to select a model for the pion, and one would hope that as more particles are measured the various consistent choices would be reduced. There are however major difficulties in this theory since the nucleon mass fixes η to be 1.025 whereas the electron mass as given fixes η to be 0.846. There are many arguments in favor of the theory for which one should refer to Born's work.[34]

Pais and Uhlenbeck[35] have investigated in general terms the significances of the multi-mass theory such as Born's and they concluded that the convergence, casualties and positive definite requirements are fundamentally severe restrictions in all theories, and that this approach to the problem of the elementary particles would appear to be inadequate.

On the other hand, Bhabha[36, 37] showed that for a particular model their conclusion does not apply and apparently he feels a solution of the multi-mass problem should not be considered as ruled out solely on these accounts.

The mass theories of Darling[38] and Zilsel[39] are constructed by postulating the elementary particle to be associated with an "inherent irreducible" volume of space time. The application of the wave equations in a finite difference representation leads to a constant of dimensions of length. The mass spectrum of such a theory is quantized and the first value of the spectrum is approximately 218 and succeeding steps are separated by $\sim$315 m. The roots are given in terms of the zero's of the Bessel functions. By fixing the mass of the proton as the thirteenth

spin 1/2 particle the fundamental length

$$a = \eta \frac{e^2}{mc^2} \quad \text{yields} \quad \eta = 1.610 \tag{49}$$

With this length one obtains the μ mass and π masses

$$M_\mu = 218.76\ m \qquad M_\pi = 271.5\ m \tag{50}$$

The authors suggest that the discrepancy between their predicted values and the experimentally determined masses is due to a small positive electromagnetic self energy correction. For the spectrum of masses, the reader is referred to their work.

One of the earlier and ostensibly simplest attempts to approach the problem of the intermediate mass particle was made by Bohm and Weinstein.[40] They considered the non-relativistic oscillation of a finite electron assuming the energy of excitation as being supplied externally. Although the value of the excitation depends upon the shape of the electron model and the entire formulation is not relativistically invariant, the result is certainly suggestive.

For a spherical shell, the frequency of oscillation

$$\omega = n\pi \left(\frac{c}{r_o}\right) \tag{51}$$

$$\Delta E = \hbar\omega = n\pi \left(\frac{1}{e^2/\hbar c}\right) mc^2 \tag{52}$$

where n is an integer. The first excited state would thus correspond to a rest mass of

$$\pi\,(137)\ m \doteq 430\ m \tag{53}$$

The rigorous solution of the electronic model, it was suggested, may show that the intermediate mass particles are really excited states of electrons.

In summary of the meson mass theory one must admit that, with the exception of the original work of Yukawa, very little new information or predictions of the expected particle spectrum have resulted from the theory. The theoretical values for the most part are not even suppose to be more than approximations due to higher order renormalization effects which have not been calculated seriously. For example, the $\pi^- - \pi^o$ mass difference, which has been known for some time, seems to have no quantitative theoretical explanation as yet. On the other hand, the problems which have slowed progress in finding a solution to the elementary particle mass problem are presumably tied primarily to the general oversupply of "elementary particles" and quantitative inadequacy of the field theories as applied to meson phenomena. In analyzing the mass data of the present work, no attempt has been made to compare the theoretical results and the experimental results due to the tentative nature of all the theoretical considerations.

II. THE DESIGN PRINCIPLES OF THE FOCUSING PAIR SPECTROMETER

In the design of a pair spectrometer, there are a few general remarks which are necessary in order to appreciate the design problems for high energy instruments.

From the historical point of view, the first pair spectrometer was that of Walker and McDaniel.[41] Their spectrometer is designed for an energy range of approximately 5-20 Mev, where the effect of multiple scattering of the outgoing pairs is so large that it is essential to provide that the scattering in the horizontal plane can be focused at the point where the detectors are located. For this reason the angle of deflection of the fragments is 180 degrees. The constant energy channels have the sum of the radii equal for various pair energy divisions.

This design has also the property that pairs which are produced in the median plane at various positions in the converter will be recorded in the same energy channels as the central pair. This will be referred to as width or lateral width focusing.

There will be abberations which result from multiple scattering in both horizontal and vertical planes that are proportional to the mean square angle.[29]

$$\left(\frac{\overline{\Delta E}}{E}\right) = (1 - \cos\theta) \doteq \left(\frac{21}{E}\right)^2 \frac{t}{t_o} \qquad (54)$$

t/t_o is the converter thickness in radiation units.

The ionization loss[29] of the pair fragments is usually unimportant except in the cases where the resolution is high.

$$(\overline{\Delta E})_{\text{ionization}} = \left(\frac{dE}{dX}\right)_{\text{ionization}} \Delta t \quad q = \text{constant} \cdot \frac{1}{Z} \left(\frac{t}{t_o}\right) \qquad (55)$$

where dE/dX is the ionization energy loss in material with atomic number Z. The higher the value of Z for the converter the lower this abberation becomes for the same yield.

The radiation loss is also small for most resolutions. The tail of the straggling due to radiation goes roughly as $1/E$ so that the resolution will appear to have a shift of the center and long low energy tail. Because of this tail, the energy shift due to this effect increases as the resolution becomes broader. The radiation loss is of course almost independent of the material for the same yield.

For very high energy gamma rays it becomes apparent that the 180 degree design would involve a magnet of considerable proportion. In fact one would need a magnet of approximately three times the weight of the 90 degree type spectrometer, other things remaining the same.

There have been several spectrometers which have used other than 180 degree apex angles. For example Lawson[42] has used an apex angle which varies from energy to energy.

The choice of the magnetic field at which to run a pair spectrometer is governed by many factors. For instance, if one considers the problem of maximizing the yield by using various pole tip inserts, one can show the main effects from the following type of analysis.

For a given conversion efficiency, the detecting efficiency of the spectrometer is determined by the fraction of the pair fragments which pass through the counting area of the detectors. This fraction is limited by the multiple scattering in the vertical plane of the particles leaving the converter which causes them to strike the pole tips. In the horizontal plane the energy acceptance of the detector bank also reduces the number of events recorded. Let us hold the vertical loss factor constant on the yield and on the resolution and assume a converter height equal to the gap. The yield Y is given as follows:

$$Y \propto gt \propto g\,(Hg)^2 \propto (NI)^2\, g \qquad (56)$$

where H is the magnetic field, g is the gap and NI is the ampere turns. For the same ampere turns on the magnet, the yield increases proportionally to the gap. This means that the yield of a large area, low field, and big gap is higher if the available ampere turns are fixed for example by the power of the current source or by the heat dissipation of the coils.

This condition also optimizes the channel width for a given width detector. On the other hand, if the channel resolutions is unimportant, the higher the ampere turns the higher the yield. This implies that the best design for yield would be a high field and a wide gap. The field is limited in an iron core magnet by saturation and if the field must be varied to cover a wide energy spectrum, it is usually better to keep in the linear regions of the magnetization curve to minimize the changes in uniformity of the field. The maximum size of the gap is limited by the divergence of the beam, although a compromise must be made between the yield and resolution on this account. The other limiting factor in the choice of gap is the availability of detectors in a multi-channel instrument. The number of channels in the design depends on the same factors. For a single, well resolved line, one can also show easily that the data rate is proportional to the number of channels and the square of the detecting efficiency and the counter heights.

If one is not limited in beam intensity or by counting losses, it is apparent that the resolving power requirement can always be met by reducing the converter thickness until the conversion from other parts of the spectrometer becomes excessive. In most respects, the pair spectrometer is similar to most precision beta ray spectrometers with the addition of size, weight, and multi-channel requirements. The design of the focusing spectrometer has been made with the purpose of combining the better resoltuion of the 180 degree spectrometer with smaller 90 degree magnet.

The main features of the focusing spectrometer can be examined in the simplified case where the effects of the fringe fields have been neglected. Figure 20 shows the 90 degree wedge with the orbits showing the effect of small angle scattering from the central orbit. The effect of the edge of the magnet is to produce a horizontal focus along the line as shown. It is easy to show that the distance from the edge of the magnet to the focus line is equal to the radius of curvature of the particle in the homogenous portion of the field. Figure 21 is intended to show the effect of the lateral converter width. In the 90

degree spectrometer, with the counters placed along the edge of the wedge, the lateral width abberation is not present in the first order theory, since there is an approximate focus for all particles of the same energy which come out normal to the converter. On the other hand, in the 180 degree apex angle design, the effect of lateral width is cancelled since the sum of the radii is independent of the origin of the pair. This latter effect is responsible for a partial cancellation of the width abberation for the present spectrometer. In the analysis of the remaining lateral width effect, it is convenient to analyze the orbits on one side of the magnet by noticing that for determining the sum of electrons and positron energies the effect is the same as if one orbit was reflected by changing the sign of the initial displacement at the converter. For the orbits of Fig. 21 one sees that the energy abberation due to width depends primarily on the angle of intersection of the orbits with the focus line among which the detectors are placed, and will therefore depend on the counter layout and the detailed orbits.

The next approximation to the actual instrument was a model which included the fringe field which was present due to the step in the pole tip. Figure 22 shows that there is an effective increase in the focal length although the change does not materially alter the focusing properties of the wedge.

For the design of the focusing spectrometer the procedure was as follows. With the fringe field model as a starting design, the region of the interest was mapped out and a preliminary set of field measurements were made to provide a more realistic model. A series of orbits were calculated on one side of the magnet, in a manner similar to the final precise orbits, Sec. V-A. By choosing a set of initial conditions corresponding to the various possible abberations in the median plane, it was possible to determine the focus line, make a calibration of the energy scale with sufficience accuracy to locate the counters, and investigate the various sources of error in both the magnetic measurements and the orbit calculations. The region of use was restricted to minimize the second order effects

which were apparent from the calculations. The magnetic measurements were started with the object of providing a precise energy calibration. With the preliminary field data and central orbits, it was possible to use a perturbation method using the differential analyzer to calculate the first order theory for the various abberations. (See Sec. V-B.) These results agreed closely with the more laborious calculations. This completed the preliminary design from which the experimental apparatus was built.

III. THE EXPERIMENTAL EQUIPMENT

Most of the equipment of the present work has been developed from that used by Panofsky and co-workers,[1] for the previous measurements of the meson capture gamma rays. Figure 23 shows the general layout of the apparatus. The high pressure gas target is shown in detail in Fig. 24. As in the previous work, no attempt is made to define the meson beam which is produced in the wolfram target. A small fraction of the mesons come to rest in the gas target. Due to the large uncertainty in the production cross sections, the internal beam current and the target penetration by the 330 Mev protons, we are not able to predict the yield of stopped negative mesons within a factor ten of the observed number of events. We observe less events than predicted. The discrepancy seems to be in the calculations rather than in the assumed processes since the work of Sachs and Steinberger[25] on the neutral meson decay gamma ray coincidences, and the electron positron gamma branching ratio shows no large deviation from the expected yields for the same capture processes, although it should be noted that the calculations of absolute yields are quite difficult. The origin of the effect seems well established. However, the existence of other modes of decay of the "excited neutron" may warrant further investigation.

The major collimation problem arises from the decay gamma rays from neutral mesons produced in the primary target in large quantities. The ratio of these background events to the stopped mesons is approximately 10^3 - 10^4.

A series of collimators both inside and outside the cyclotron vacuum chamber were aligned with the hydrogen vessel in place. The collimation is shown in Figs. 25 and 26.

The gas handling equipment for pumping the hydrogen into the vessel at 2700 psi was the same as in the preceding work.[1] The time for filling, dumping, or changing gases was reduced to less than 30 minutes per operation. The pressure and temperature of the hydrogen vessel was monitored continuously for safety purposes.

The 17 ton pair magnet was carefully aligned so that the center of the target was within 1/16" of the centerline of the collimating system. The magnet pole tip insert was accurately pinned to the magnet and all positions were measured relative to a large machined template that could be fastened directly to the insert pole tip. The precision template was bored with a series of holes and slots which formed the grid for the magnetic measurements. The tolerances were held so that the error of the magnetic measurements due to the position of the template would be less than 1 part in 10^4 in the region of maximum field gradient. The target location, counter location and alignment were also made relative to the template.

Figure 27 shows the layout of the counters on one side of the magnet, and several sets of orbits. In order to increase the active volume of the Geiger counter detecting channels, Geiger tubes were paralleled so that 4-1/2 inch length was obtained. The beam view of the vertical aperture is shown in Fig. 28. To reduce the channel width the number of tubes was increased to 54, and a coincidence overlap channel system was used. Using the energy scale from the preliminary design calculations, the centers of the tubes were located such that 1.5 Mev separated the tubes. The channels defined by the coincidence between adjacent tubes served to further reduce the channel to approximately 0.75 Mev. Due to variations in the energy scale the overlap and non-overlap tubes had slightly different geometrical apertures. Since the energy scale was improved by later calculations, the resulting channel width was really slightly larger than the design value. (See Sec. V-C.) The channels with paralleled tubes were placed in four equally spaced rows, and centered about the focus line to allow for sockets and wiring. Corrections were made in each tube location for the angle of the intersection of the orbit with the focus line and for the small residual curvature due to the fringe field along the counter lines. In the reduction of the data, the weights assigned to the overlap channels were determined experimentally to be very closely the same as the non-overlap channels. In the background run the spectrum was found to be smooth.

Although the data was not sufficiently accurate to compare the density of counts for each channel, the average effect was found by adding up the counts in all overlap channels and determining the ratio to the total counts. This was also done for the hydrogen and deuterium gas runs for energies outside the signal region. The conclusion of these reductions is that a 5 percent difference in weight would have been detected. Since this is a very complicated process, which is sensitive to individual tube efficiencies and counting losses, a further theoretical analysis of purely geometrical effects would be unjustified. There is, however, no appreciable error in the energy scale or the resolving power introduced by the assumption of equal weights due to the small size of the channel width resolution and the averaging effect over all the channels.

The electronics used to record the events is shown in block form in Fig. 29. In order than an event be recorded, the following requirements were made. A quadruple coincidence between the four proportional counters must occur within two microseconds. The cyclotron beam must be near full radius. One or more Geiger tubes must be fired on each side, as indicated by a set of neon bulbs at the recording position. Any events with more than four tubes firing was excluded and some events were rejected in which two tubes were fired that were not adjacent; a result of either a random coincidence or a large scatter of a pair fragment. For the maximum rate of data gathering of about 20 counts an hour in these experiments, it was possible for one man to record the data without losing more than 10 percent of the events. Whenever possible, two recorders were taking data. Since none of the energies are easily recognized during the recording of the channels fired, those events which were lost due to flurries of counts were probably a random sample of the entire spectrum. Whenever any doubt as to the time sequence or channels involved was expressed, the data was dropped. It is possible that a few coincidence events due to overlaps may be rejected due to the higher probability of confusion in recording. In early runs, a slow speed camera was used to record all the events. This additional method it was found, was capable of resolving much higher data rates than were necessary for the present work. Visual observation proved to be entirely adequate. Any electronic device which could perform the function outlined above was considered at the time to be completely out of the question.

IV. MAGNETIC FIELD MEASUREMENTS

A. General Method and Requirements

Figure 30 shows the shape of the field with the approximate equal magnetic field contours indicated. The field measurements were divided into separate regions because of the various field gradients and the accuracy requirement that was necessary. Figures 31 and 32 show the complete set of measurements with the method used.

The size of the field gradient divides the field into two parts. The region where the magnetic field is homogenous can be measured accurately using the nuclear induction technique.[43] The area shown as A was measured in this manner. The remaining field was measured by the use of a high sensitivity fluxmeter and search coil. The system used was as follows: A grid was laid out to cover the entire region. The search coil was moved from point to point in the field and the resulting deflection measured. This data is referred to as slip data. At a field value approximately one percent of the maximum field, another search coil was flipped and the deflection was recorded. The area and sensitivity of the fluxmeter were determined with reference to the proton moment. This data is called the flip data.

This procedure would in principle be sufficient to determine the field to the desired accuracy in the following manner. Knowing the field by the proton moment data at approximately 99-100 percent field, and at approximately one percent field, one compares the change in field with the total deflection of the slip measurements summed over any continuous path linking these two. This gives the conversion sensitivity of the slip data which can then be used to map the entire horizontal plane of the magnet. The accuracy, however, requires the conversion sensitivity to be accurate and constant over the region. It was found that this conversion sensitivity varied from path to path in an amount which although entirely consistent with the accumulation of reading errors was larger than desirable. For this reason, an alternative system of measurement was developed for the purpose of

elimination of the accumulated errors due to these fluctuations. The measurement consisted of the rotation of two coils, one of which is in the spectrometer magnet, and the other in a slave magnet which has a uniform field measurable with the proton moment. By adjusting the slave magnet with the coils connected bucking, it is possible to balance the flux using the fluxmeter as null indicator. Using this cancellation technique, a set of points were measured in the regions where accuracy was required. The slip coil data was joined to these points in the following manner. Several slip runs were made between cancellation points establishing a coarse net which is essentially free from effects due to accumulation of reading errors. The values obtained were used as intermediate check points. In important regions, the error of closure was effectively distributed by determining the conversion sensitivity over each small region. Although the adjustments from the values obtained independent of cancellation measurements were small, the cancellation method outlined yields a more accurate net for field values.

B. Proton Moment Data

The instrument used was the Varian Associates Nuclear Induction Flux Meter. The frequency standard used was a General Radio Signal Generator, which has an operational reading accuracy of approximately ± 0.003 percent. The crystal standard has been checked indirectly against WWV and is stable to better than $1/10^5$. Limitation in the frequency measurements here consisted of the strength of the fluxmeter oscillator output, pulling of the fluxmeter oscillator due to the frequency meter, and slight misalignment of the interpolation metering circuits, none of which were large enough to contribute appreciably to the error of these measurements.

There were 248 measurements made in a region where a sufficiently small field gradient permitted use of the proton moment method. Of these, about 1/3 were omitted, using in preference the slip measurements which overlapped the region. The proton moment head was mounted in a brass block which could be adjusted for centering

the hydrogen sample. The effective electrical center of the sample was positioned by measuring the field with the sample located in a region of medium gradient; that is for a point where the proton moment data would be normally discarded due to the width of the signal. The sample was then rotated about the locating hole. The shift of the signal was minimized by adjusting the sample relative to the locating pin. This method although extremely crude, was found to be sufficient to reduce this source of error to well below $1/10^4$.

The major source of error for these measurements was in the location of the center of the nuclear induction pattern. No attempt was made to shim the field so that the region where the measurements were required the field was inhomogenous in varying degrees. The region of overlap between the slip data and the proton data furnish a convincing check upon the consistency of the results for various gradients. The disagreement is the combination of errors of both measurements and it was found that the spread is less than $2/10^4$.

The regulation of the magnetic field played a roll in increasing the spread of values during some of the measurements. This was especially true for the slave magnet measurement, since the requirement of $1/10^4$ over the whole range of the regulator was desired. The field regulator[44] was designed originally to hold $1/10^3$ over long periods and transient changes of $2\text{-}4/10^4$ were apparent in some situations. In fact, for the best combination of generator and regulator regulation, considerably better than $1/10^4$ was obtained for long periods. No field measurements were made when any oscillations of the field greater than $2/10^4$ were observed. Jumping of the regulator was noticeable which made it necessary to monitor the field continuously during the cyclotron run.

C. Slip Data

The main bulk of the field measurements were made with a search coil and fluxmeter. The search coil was selected with the maximum permissible area and mounted in an elaborate positioning

block. The block was made so that adjustment could be made in both directions relative to the positioning pin, as well as both rotational axes. The adjustments were made by rotating the coil holder about a vertical axis which passed through the center of the positioning pin. The rotation was made near the maximum field gradient, and the deflection on the fluxmeter was reduced to a minimum by the translational adjustements. The deflection sensitivity was sufficient to detect an error of a few thousandths of an inch of the electrical center from the rotation axis. The error due to the finite size of the search coil was less than $1/10^4$. The reading sensitivity was chosen to be as high as possible without introducing errors due to the instability of the meter. Although it is difficult to determine the exact cause of drifts, the behavior suggests that it arises from thermal effects. Since careful compensation of the fluxmeter was made for all measurements, this effect was a negligible source of error. In general, the drifts were measured by always returning to the starting point for each set of runs and the error of closure was spread equally throughout the run. No data was included when the accumulation of drift exceeded a millimeter deflection.

There were two methods of checking the measurements for internal consistency. A series of cross runs were made to eliminate the accumulative errors. By determining the errors of closures, it was possible to check the accumulation effects severly for both gross errors of drift and genuine statistical fluctuations due to the reading accuracy. Each series of runs was made to overlap by one step. These steps are sensitive to the drift compensation for a run, since the entire error of an incorrect drift correction is applied to the last measurement of a run, and very little correction is made to the first measurement of the next run. These results show that the error is on the average biased in one direction, and from these checks several sets of runs were rejected and repeated until the drift error was reduced. The reproducibility of many measurements has also been analyzed statistically with satisfactory results. It should be emphasized that most of the errors of these results occur during the high

gradient measurement. Therefore, one must use considerable judgment in assigning a weighted probable error for these measurements. This problem is examined in Section V-B.

D. Flip Data

At a value of about one percent of the maximum field, the search coil used in the cancellation data was flipped. The fluxmeter sensitivity and coil area were calibrated indirectly in terms of the proton moment standard. These standardizations have been cross checked in many ways, and are reliable to better than a part in 10^3. For this measurement, the entire uncertainty arises from the fluxmeter deflection and its sensitivity calibration.

E. Cancellation Data

From the preceding sections, the fact that most of the errors of the field occur due to accumulation of gradient dependent effects has been emphasized. Due to the many steps in the Slip Data from the high field to the low field, both of which are well known, considerable care must be taken to eliminate random and systematic errors properly.

There are several widely used techniques of measuring strongly inhomogeneous fields. The accuracy depends largely on factors which include accurate locations, sensitivities, etc. The method used as an overall master grid for the slip measurements was developed using two bucking search coils. The probe coil and the slave coil are placed in series with a sensitive fluxmeter such that when they are rotated simultaneously by means of manually driven geared selsyns the fluxmeter records the difference between the flux linked by each coil. When the difference is zero or near zero, the field in the slave magnet is determined by the use of the nuclear induction fluxmeter. By measuring the ratio of the areas of the coils the field at the probe coil can be calculated.

The set up for these measurements became more elaborate as the various behaviors of the system were understood. The search

coils were chosen to have approximately the same areas, and were selected to maximize the fluxmeter sensitivity as in the Slip Data measurements. These coils were mounted in brass blocks that were positionable; that is a number of degrees of freedom were provided to allow the electrical center of the coil to be positioned empirically over the centerline of the template grid hole as in the other adjustments. The design of the rotating mechanism required close mechanical tolerances, rigidity and portability. The positioning was done with a sensitivity twice as high as that used on the runs since fluxmeter stability could be sacrificed. The rotating parts of the coil holder close to the coil were insulators to reduce eddy current effects.

The planes of the bucking coils were aligned by rotating them and adjusting the relative phase angle to minimize the signal due to the phase error. Microswitches on the shafts were positioned to record the endpoints of the flip. The slave magnet was regulated and controlled by the fluxmeter observer. Its field was just uniform enough to allow its use. Most of the reading error of the nuclear fluxmeter was due to the slight field gradient. The sensitivity of the fluxmeter was measured by varying the slave magnet between two field values monitored by the proton moment fluxmeter. The error signal was kept low enough to prevent any noticeable error due to this calibration. The ratio of the two coil areas was also determined using the nuclear fluxmeter by placing the probe coil in a uniform field region. Both fields were measured simultaneously by switching the nuclear fluxmeter from one magnet to the other during the flip. Finally, the uniformity variation in the slave magnet was measured and the monitoring probe placed in the most uniform region. It remained in the same position during all the measurements.

The time required for a single measurement once the equipment was properly aligned was 15 minutes on the average. The rotation speed was approximately 15-20 seconds per flip. The speed was

varied to detect any eddy current effects and none were observed. Since the fluxmeter compensation for a long flip was somewhat critical, the flip was made from 0 to 180 degrees and the direction reversed back to 0. The average of the deflections was used when the error of closure was less than two millimeters. A minimum of three flips were averaged during which any slight drifts in the slave magnet regulation were observed with the nuclear fluxmeter. The spectrometer field was also monitored in one spot by the nuclear fluxmeter, held constant against slow drifts due to temperature changes. The spectrometer magnet was sufficiently stabilized against short time drifts since the regulation electronics could be adequately adjusted for a fixed field. The slave field however was varied over a factor of three during the measurements so that some compromise in regulation accuracy was necessary to allow for the wide range covered. In order to check the reproducibility of the measurements, several points were repeated immediately preceeding the determination of the meson mass after which the pole tip was not disturbed. The agreement between these measurements and the main field determination was satisfactory. The ratio of areas and fluxmeter sensitivity were both checked during different sets of measurements.

By using the methods outlined in Section IV-A for analysis of the Slip Data there is an additional chance to check both measurements. One can compute an average sensitivity for the slip measurements without reference to any cancellation data. The field can be mapped assuming this value to hold everywhere and the values obtained can be compared with the method using the cancellation data. There are several instances out of the thirty points where the disagreements obtained appear to be slightly larger than the combined errors assigned to either method. A careful study, including more measurements, was made to investigate if these were really significant. It was concluded that the accumulated statistical error of the slip coil data was in all cases sufficient to explain the deviations. Table 2 lists the various checks with limits of accuracy.

F. Summary of Accuracy

The assignment of the error of the field measurements depends upon the relative weights assigned to the regions shown in Fig. 30. The following remarks are intended to show where the main errors are introduced from the field values alone.

The error in the end position of the orbits can be understood in terms of the angular bend which the field produces. When a small error is made in the field, this corresponds to an impulse or perturbation in the orbit. This problem has been treated in the following section, V-B. Figure 33 shows the solution for small displacements along the arbitrary length which may have been caused by errors in the field. The impulses which produce the largest effects are those which occur at defocusing positions, i.e., near the middle of the orbit, small errors of the initial field values will be focused out and errors in the final field values will not have sufficient lever arms to produce any displacement along the detector line. Of course the impulse due to a number of succesive errors can become serious so that the weight of the region depends on its relative position and its relative length.

Table 2 summarizes the contributions to the energy scale error from the errors of the various typed of data.

The main errors of the field measurements come from the uncertainty in the location of the proton moment signal and from the readings of the fluxmeter in the uniformity slip runs. The first of these depends upon the unfortunately wide signal due to the inhomogeneity of the slave magnet. The stability of the field regulation contributes a sizeable error due to the fact that it appears in a majority of the errors which compound in the absolute cancellation check points. The fluxmeter readings have been converted to field values in a manner which tends to minimize the accumulation of reading errors. Each value represents the average of three or more readings.

The entire grid of field values is given in Table 3.

V. THE THEORY OF THE PRECISION FOCUSING SPECTROMETER

A. Central Orbits

The energy scale of the spectrometer has been determined by a numerical integration method using the accurate field values. The differential equation for the radius of curvature of a charged particle in a magnetic field can be written in rectangular coordinates:

$$\frac{\frac{d^2y}{dx^2}}{\left[1+\left(\frac{dy}{dx}\right)^2\right]^{3/2}} = \frac{1}{R_c} \tag{57}$$

where R_c is given in terms of the magnetic field H(x, y),

$$R_c = \frac{pc\,10^8}{Hc} = \frac{E\left[1 - 1/2\left(\frac{mc^2}{E}\right)^2 + \ldots\right]10^8}{Hc} \tag{58}$$

where pc, E, mc^2 are in Mev, H is in œrsted, R_c is in cm, and c in cm/sec. The choice of the coordinate system for this integration was made to keep dy/dx always less than one. The numerical method was the Bessel central difference quadrature formula.[45, 56]

The coordinate system was chosen so that the independent variable steps of the integration are along one coordinate of the magnetic field grid. In regions of low gradient where fewer field measurements were necessary consistent with the required accuracy field values used for the integration were found by using Lagrangian interpolation tables.[47] The error due to neglecting higher differences in the four point interpolation was calculated to be a maximum of a part of 10^4 in the worst cases. The numerical work of the integration was to a large extent self checking. Five decimals were carried throughout to reduce the error of round off and differences as high as necessary were used to assure that no accumulative error other than rounding off was introduced by the step size. The orbits were started with independent variable steps

of 1/2 inch. It was necessary for some orbits to reduce the steps to 1/4 inch when the high differences became unmanageable. At the ends of the orbits the fields were considerably lower and the steps were increased to 1 inch. The integrations took from 75 to 100 steps per orbit.

Before analyzing the errors of the calculation, it is best to follow through the calculation steps in detail. The differential equations that are solved are:

$$\frac{d^2y}{dx^2} = \pm \frac{1}{R_o} \frac{H(x,y)}{H_o} \left\{1 + \left(\frac{dy}{dx}\right)^2\right\}^{3/2}$$
$$\frac{d^2x}{dy^2} = \pm \frac{1}{R_o} \frac{H(x,y)}{H_o} \left\{1 + \left(\frac{dx}{dy}\right)^2\right\}^{3/2} \qquad (59)$$

The quantity R_o is the radius of curvature at the converter that depends upon the energy of the electron whose orbit is being calculated. The beginning of the 49 Mev orbit is given for illustration in Table 4.

The notation on the sample calculation is as follows:

$$\frac{dy}{dx} = g \qquad \frac{d^2y}{dx^2} = G$$
$$\frac{dx}{dy} = f = \frac{1}{g} \qquad \frac{d^2x}{dy^2} = F = -\frac{G}{g^3} \qquad (60)$$

Thus, G or F is given by the differential equation in terms of the field at the point x, y and the estimate for the derivative g or f. The difference table is constructed from G or F, so that to the left the first sum 'G or 'F is related to the first derivative and the second sum "G or "F is related to the y or x coordinate. To the right the first and higher differences, Δ^1, Δ^2, refer to the third and higher derivatives.

The interpolation and extrapolation equations which constitute the Bessel central value quadrature method are as follows:

$$y_3 = \omega^2 \left\{ {}''G_3 + \frac{1}{12} G_3 - \frac{1}{240} \Delta_3^2 \cdots\cdots \right\}$$

$$g_1 = \frac{\omega}{2} \left\{ 2'G_1 - \frac{1}{12} 2\Delta_1 + \frac{11}{720} 2\Delta_1^3 \cdots\cdots \right\} \qquad (61)$$

$$g_3 = g_1 + 2\omega \left\{ G_2 + \frac{1}{6} \Delta_2^2 - \frac{1}{180} \Delta_2^4 \cdots\cdots \right\}$$

There are similar equations for F.

The quantity ω is the stop size. The formulas are derived in the references. They are used to extrapolate the difference table in a manner that converges rapidly and is not sensitive to errors in the unknown higher differences. In Eq. 61, the value for the appropriate odd difference is taken as the mean or central value for the step. Thus, for example,

$$2'G_1 = {}'G_{1/2} + {}'G_{3/2} \quad \text{etc.} \qquad (62)$$

The procedure for calculation of an orbit is as follows. The starting values of the difference table are obtained in an independent manner, as follows: By using the field values near the converted the orbit is constructed as a series of circular arcs over 1/2 inch steps. The radius of the arc is fixed by the field at the center of the arc. This approximation is valid to the required accuracy as long as the field is reasonably constant as it is near the converter. This permits the calculation of five steps and the table can be constructed as far as the dotted line. Next, one fills in the difference table by guessing until line opposite step No. 3 is complete to the number of entries necessary for the accuracy required which depends upon the relative size of the differences and extrapolation coefficients. y_3 and g_1 can be calculated using Eq. 61. G_1 is recalculated from the differential equation

$$G_1 = \pm \frac{1}{R_o} \quad \frac{H(x_1, y_1)}{H_o} \quad \left\{ 1 + g_1^2 \right\}^{3/2} \qquad (63)$$

These three steps are repeated adjusting the differences until the results are consistent with the starting values. g_3 is then calculated with Eq. 61. G_3 can be calculated from the differential equation

$$G_3 = \pm \frac{1}{R_o} \quad \frac{H(x_3, y_3)}{H} \quad \left\{ 1 + g_3^2 \right\}^{3/2} \qquad (64)$$

by interpolation of the field grid to determine $H(x_3, y_3)$.

If the independent variable is x, the steps are made with the magnetic field grid spacing equal to the step length so that interpolation is necessary in y only. Using the four values of the field centered about y, the value at y can be found by using the table of four point Lagrangian interpolation coefficients.

This allows the correction of the table that was filled in by guessing. Since the differences will change, it is necessary to recalculate y_3, g_3, and G_3 until G_3 remains unchanged. When this process converges, one is able to continue on to the next step, beginning with Eq. 61, and repeating the procedure as described above. This is, compute y_4, g_4 and G_4 and correct differences, etc. When g approaches 1, the independent variable is switched over to y, and Eq. 60 is used. The starting values for integral y values in the table for F are obtained by interpolating the table of y and G using five point Lagrangian interpolation coefficients and Eqs. 60. The integration proceeds as before. f will begin approximately 1 and will go to zero, as the edge of the field is reached. f then grows again slowly, until the end of the orbit at the focus line.

The error in the calculations was in all cases due primarily to the accumulation of the uncertainties in the magnetic field. Although the step size was determined to minimize the computational difficulty, the resulting number of steps was probably very close to the optimum value.

Orbits were computed for three energies 49, 65 and 81 Mev on each side of the magnet. One orbit was run at 57 Mev for the purpose of checking whether the three orbits were sufficient to determine the entire range used which extended from 44 Mev to 86 Mev.

Table 4 shows the results for the orbits calculated. The coordinates for the point of intersection of the orbit with the counter line are given. The angle ϕ listed is the angle of intersection. See Fig. 27 for the orbit plot.

B. Solutions for Small Deviations from the Central Orbit

The small displacements produced by the finite area of the converter and the initial angles at the converter due to multiple scattering can be treated similarly to the vertical and horizontal oscillations in the inhomogeneous cyclotron field. If ρ is the deviation in the median plane from the central orbit and Z is the vertical displacement the equations for the motion become:

$$\frac{d^2\rho}{ds^2} + \left(\frac{1-n}{R^2}\right)\rho = 0 \quad \text{or} \quad \rho'' + A(s)\,\rho = 0$$

$$\frac{d^2Z}{ds^2} + \left(\frac{n}{R^2}\right) Z = 0 \quad \text{or} \quad Z'' + B(s)\,Z = 0 \tag{65}$$

where $n(s) = \left[R(s)/H(s)\right]\left[dH(s)/d\hat{n}\right]$, $A(s) = \left[1 - n(s)\right]/R^2$, $B(s)$ $n(s)/R^2$, R = radius of curvature and (s) is the distance measured along the central orbit. $\hat{n}$ is the outward normal. For the case where n is not constant over the orbit the equation still holds as the first approximation. In this case the frequency or wavelength of the oscillation varies along the orbit. The terms neglected in this approximation are discussed in Sec. V-D.

The solution of the two equations for ρ and Z can be found easily by many methods. The application of a differential analyzer at the Radiation Laboratory[48,49] was chosen since the equations are a relatively simple matter to handle. The restoring terms were computed from the field data along each of the three major orbits and are shown in Figs. 34 and 35. The results for ρ and Z are shown in Figs. 36 and 37. The general solutions of the perturbation equations can be found in terms of the two particular solutions, ρ_I and ρ_{II}, from the initial conditions for the particle at the converter. The oscillation shows the focusing and defocusing action of the field as discussed in Sec. II. The focus against multiple scattering which appears for ρ_I occurs along an approximately straight line. The effect of the lateral width on the energy scale can be found from ρ_{II}. To determine the aberration in the first order theory, the initial conditions can be varied and the change in apparent energy at

the detector line calculated. This general procedure is followed for all types of abberations in the following sections dealing with the resolving power.

To evaluate the dependence of the energy scale upon the magnetic field values, the solution of the perturbation problem can be used. Consider the orbit of energy E_γ which has been perturbed in the ρ plane. The perturbation solutions are such that if, due to an error in the field, an angular error of $\delta\theta$ is produced at a position along the orbit corresponding to the arc length S, the orbit will be distorted to an orbit:

$$\rho(s) = a\,\rho_I(s) + b\,\rho_{II}(s) \tag{66}$$

Since the angle that the particle bends through as a result of a field H can be written as

$$\theta = \frac{Hds}{H\rho} \tag{67}$$

the change in the angle $\delta\theta$ is given by

$$\theta = \frac{\int \delta H ds}{H\rho} \doteq \frac{\delta H}{H}\ \frac{\Delta s}{\rho} \tag{68}$$

If this field error occurs at s

$$\begin{aligned} \rho(s) &= 0 \\ \rho'(s) &= \delta\theta \end{aligned} \tag{69}$$

since

$$\begin{aligned} \rho'(s) &= a\,\rho_I'(s) + b\,\rho_{II}'(s) = \delta\theta \\ a\,\rho_I(s) &+ b\,\rho_{II}(s) = 0 \end{aligned} \tag{70}$$

we have that

$$b\left(\rho_{II}'(s) - \frac{\rho_{II}(s)}{\rho_I(s)}\ \rho_I'(s)\right) = \delta\theta \tag{71}$$

However, the error of the energy is given in terms of the energy dispersion $dE/d\ell$ along the detector line ℓ, the angle ϕ of intersection of the orbit and the detector line and the displacement produced by the perturbation. Since ρ_I is zero at the orbit termination s_f, the coefficient b determined the displacement at the detector.

$$\delta\rho_f = b\,\rho_{II}(s_f) = \frac{\delta\theta\ \rho_{II}(s_f)}{\left[\rho'_{II}(s) - \frac{\rho_{II}(s)}{\rho_I(s)}\,\rho'_I(s)\right]} \tag{72}$$

Substituting for these quantities, we obtain:

$$\frac{\delta E}{E} = \frac{1}{E}\frac{dE}{d\ell}\,\delta\rho_f = \frac{1}{E}\frac{dE}{d\ell}\,\frac{1}{\sin\phi}\,\frac{\delta H}{H(s)}\,\frac{\Delta s}{\rho(s)}\,\frac{\rho_{II}(s_f)}{\left[\rho'_{II}(s) - \frac{\rho_{II}(s)}{\rho_I(s)}\,\rho'_I(s)\right]} \tag{73}$$

It is also true that if the field were off by a constant the error of energy would be:

$$\frac{\delta E}{E} = \frac{\delta H}{H} = \frac{\delta H}{H_o}\left(\frac{H_o}{H}\right) \tag{74}$$

The ratio of these two quantities is defined to be the weight:

$$w(s)ds = \frac{1}{E}\frac{dE}{d\ell}\,\frac{1}{\sin\phi}\,f(s)\,ds$$

$$f(s) = \frac{\rho_{II}(s_f)}{\rho(s)\left[\rho'_{II}(s) - \frac{\rho_{II}(s)}{\rho_I(s)}\,\rho'_I(s)\right]} \tag{75}$$

and the total energy shift will be

$$\frac{\delta E}{E} = \int \frac{\delta H}{H}\,w(s)ds = \int \epsilon\, w(s)ds = \int \epsilon'\,\frac{H_o}{H(s)}\,w(s)da \tag{76}$$

$w(s)$ is the weighting function for an error of the field of $\delta H(s)/H(s) = \epsilon$; that is, the field is in error by an amount which is a constant fraction ϵ. However if the field is in error by a constant amount $H = \epsilon' H_o$ the weight is multiplied by H_o/H. The first case applies if the field varies as a result of change of the regulated current source, for example. The latter case holds when the source of error is a constant such as one that depends upon the reading sensitivity. Both of these weighting functions are shown in Fig. 33.

C. Resolving Power. First Order Theory

The resolution of the pair spectrometer is calculated by combining the various sources of line broadening. The main components are due to the finite size of the detector, the imperfect focus of multiple scattering in the converter, the ionization and radiation loss of pair fragments in the converter and the effects of higher order orbit corrections which are discussed in Section V-D.

The finite detector component is complicated due to the fact that the energy scale from which the counters were positioned was slightly in error.

If one specifies the pair of counters, the probability of counting a gamma ray pair for various energy gamma rays is defined to be the resolving power. If the detector windows are of equal width the result is a triangular resolution of base width equal to the sum of the detector widths. One can write it thus:

$$R(E_\gamma) = \int_0^\infty P(E_+)P(E_-)d(E_+) = \int_0^\infty P(E_+)P(E_\gamma - E_+)dE_+ \quad (77)$$

$P(E_+)$ and $P(E_-)$ are the probabilities of counting the position of energy E_+ and the electron of energy $E_- = E_\gamma - E_+$. For this simple case the resolution integral is recognized as the folding integral which is easily evaluated to yield a triangle. If the windows have unequal widths, the resulting resolution is a trapezoid. If the energy widths and the centers of all the detectors are known, the channel width resolution trapezoids can be constructed.

Table 5 shows the counter positions and the energy of the center of each channel.

The remaining problem of averaging over various channels was done using the trapezoids for various pair division intervals, weighted with the pair fragment distribution as given by Rossi-Greisen.[29] The uncertainties of these weights are of no consequence in the accuracy of the energy scale. The result is shown in Fig. 38. The dotted curve is the ideal resolution as predicted by the preliminary design.

In order to calculate the effect of multiple scattering on the resolving power, use was made of the differential analyzer results (Sec. IV B) for various cases. For a section of converter (at a given depth) from which pairs are produced, there is a distribution in the projected angle of either of the emergent particles which is nearly Gaussian with a r.m.s. width θ_M given by the relation:[29]

$$\theta_M^2 = \left(\frac{16}{E}\right)^2 t/t_o \tag{78}$$

where t/t_o is the path length in radiation units of the particles in the converter and E is their energy. From the distribution in angles as calculated at the converter, one can convert to a distribution in energy as measured by the four rows of counters which are spaced symmetrically about the focus line at a distance u. K is the ratio of the deviation angle at the detector to the scattering angle at the converter, obtained from the solution of the homogeneous ρ Eq. 65. ϕ is the angle of intersection of the orbit with the focus line and is the distance measured along the focus line.

$$\tan\theta = \rho_o' \doteq \theta$$

$$P(\theta) = \frac{1}{\sqrt{2\pi}\,\theta_M} e^{-\frac{\theta^2}{2\theta_M^2}} \tag{79}$$

From the geometry of the focus line

$$\Delta E = \frac{dE}{d\ell}\Delta = \frac{dE}{d\ell} u\left[\cot(K\theta + \phi) - \cot\phi\right] \tag{80}$$

Therefore the energy distribution will be

$$\frac{dN}{dE} = P(\theta)\frac{d\theta}{dE} = \frac{\sin^2(K\theta + \phi)}{2\pi\,\theta_M K \frac{dE}{d\ell} u} e^{-\frac{\theta^2}{2\theta_M^2}} \tag{81}$$

It is therefore possible to compute the distribution for a given energy due to pairs produced at a given depth in the converter by folding together the distribution for the two fragments. A typical result for a 65 Mev electron and a 65 Mev poistron coming from the first 30 percent

of the converter is shown in Fig. 39. The results for the different thickness increments are then averaged over the converter thickness.

It is clear that the results for the four separated detector lines are considerably narrower than for the resolution obtained in the previous type spectrometer. A factor of 40 in the half widths has been obtained, for the same converter thickness (compare Fig. 17 and Fig. 39).

The other effect of multiple scattering is to cause loss of particles in the verticle plane. The results of the Section IV-B can be applied to this problem in a manner similar to that for the horizontal case. If one wants to know what fraction of the particles is counted, one calculates the probability that a pair produced in a particular strip of the converter in the Z direction from a given depth will fall within the counting volume height h. If Z_I ($Z_o = 0$, $Z_o' = \theta_M$) and Z_{II} ($Z_o = 1$, $Z_o' = 0$) are the two solutions to the Z equations of Eq. 65, the general solution will be a linear combination whose coefficients will be given in terms of the initial conditions.

$$Z(s) = \left(\frac{Z'_o}{\theta_M}\right) Z_I(s) + \left(\frac{Z_o}{1}\right) Z_{II}(s) \tag{82}$$

For the final value of s, Z must be less than or equal to h. The height h of the detector is 2.25 inches. Thus, for a given Z_o the maximum initial angle Z_o' is determined by Eq. 82. Figure 40 shows the plot of Z_o against Z_o'. Only the region within the trapezoid will be counted in the detector. The distribution in angle of particles from various depths is given by Eq. 79. The probability of counting the two fragments simultaneously is an integral

$$I(t, Z_o) = \frac{1}{2\pi\, \theta_M^+\, \theta_M^-} \int_{\theta_1^-}^{\theta_2^-} \int_{\theta_1^+}^{\theta_2^+} e^{-\frac{1}{2}\left(\frac{\theta^+}{\theta_M^+}\right)^2 - \frac{1}{2}\left(\frac{\theta^-}{\theta_M^-}\right)^2} d\theta^+\, d\theta^- \tag{83}$$

where θ_1^+, θ_1^-, θ_2^+, θ_2^- are the limiting angles in Fig. 40. This must be integrated over Z_o to find the efficiency for detecting pairs from a given depth of converter.

$$W(t) = \frac{\int_0^{Z_{o\,max}} N(Z_o)\, I(t, Z_o)\, dZ_o}{\int_0^{Z_{o\,max}} N(Z_o)\, dZ_o} \qquad (84)$$

Where $N(Z_o)$ is the probability of producing a pair at height Z_o. This probability will be uniform if the collimation is properly alligned.

W(t) can be integrated to give the theoretical yield vs. thickness relation. Fig. 41 shows the result together with the experimentally determined points. All the resolution effects due to finite target thickness must be weighted with W(t) in a final average.

The energy loss in the converter due to radiation and ionization can be calculated in the usual way for each thickness increment of the converter.

The radiation probability is given in terms of the thickness and the energy as follows.[30]

$$P(E)\, dE = K \left[\log \frac{E_o}{E_o - E}\right]^{-(1-bt)} dE \qquad (85)$$

The constant b can be evaluated from the radiation probability[29] at the energy E_o with the corrections that have been observed in the Bethe-Heitler theory.[42] This correction amounts to about 7.5 percent in tantalum. The error of this correction is about a percent which fortunately does not contribute an appreciable error to the results. Figure 42 shows a typical radiation straggling probability curve.

The ionization loss of fast electrons is the major remaining source of resolving width in the first order theory. Since it is responsible for a skew effect as a result of finite target thickness, the calculation must be made carefully to eliminate any error in the location of the center of gravity of the resolution.

The mean ionization loss of electrons and positrons has been calculated[29] in terms of a mean ionization energy I_o. The results for both particles agree closely at this energy and in the following the electrons and positrons are treated as being equivalent.

The equation for the ionization loss from which the results were calculated was

$$\frac{dE}{dX} = -\frac{2\pi N Z e^4}{mc^2 \beta^2}\left[\log_c \frac{(mc^2)^2}{2I_o^2} + \log_e\left\{\beta^2\gamma^2\,\frac{E - Mc^2}{mc^2}\right\} - \left(\frac{2}{\gamma} - 1 + \beta\right)\log_e 2 + (1 - \beta^2)\right] \qquad (86)$$

$$\frac{dE}{dX} = -(0.1536)\frac{Z}{A}\left[20.39 + 3\log\frac{E}{mc^2} - 2\log Z\right]$$

when X is expressed in grams/cm^2 and $I_o = 13.5\ Z$.

In the calculations, the following corrections were made to Eq. 86. I_o was altered to agree with that measured by Segrè and Mather.[55] This amounts to an ~2.8 percent reduction in the ionization loss. The Halpern-Hall density effect[56] calculation was applied and gave ~13 percent ± 2 percent reduction in the ionization loss. The effect of straggling in the collision processes was taken into account by the use of the Landau distribution.[57] The effect of this correction on the width of the resolving power is by no means negligible since the most probable energy loss is 30 percent lower than the mean energy loss. There are at present only a few experimental verifications[58] of the Landau distribution. The Landau straggling does not introduce any error in the mean energy loss on which the mass depends. It is possible that an accumulation of errors in these corrections may produce an error of as high as 5 percent in the ionization loss and this uncertainty has been included in the error of the meson mass. Figure 43 shows the distribution of energies, resulting from the Landau effect, of the pair fragments which are produced in the center of the converter. Figure 44 shows the results of ionization loss alone averaged over the converter thickness. This resolution component can usually be approximated by a rectangular curve in cases where it is only a small fraction of the total resolution width.

The first order resolving power is found by folding each of the sources of width together and applying the calculated weights in averaging over energy and target thickness. Figures 45 and 46 show the composition of the first order resolution as averaged over converter thickness. The final result is shown with the data for hydrogen in Fig. 47.

The comparison shows that the line shape of the γ-spectrum is considerably broader than the resolution. It is apparent that the second order theory must be included in order to account for the width of the line.

The effects described so far are usually what is meant by the first order theory of the spectrometer.

The ionization loss of particles in air has also been calculated with the use of the solutions for small deviations from the central orbit (Sec. V-B). The result of the magnetic field deviation calculation can be used since the effect of loss of energy in air of the electrons is to cause a change in the radius of curvature. In fact, if we use Eq. 76, we can calculate the change in energy at the detector by integration of the energy loss over the arc length of the orbit. The quantity to be weighted by w(s) has accumulated a deviation proportional to s which we must insert as the deviation from the unperturbed orbit.

$$\frac{\delta\rho}{\rho} = \int_0^s \frac{1}{E}\frac{dE}{dx}\,ds = \frac{1}{E}\frac{dE}{dx}\,s = \epsilon$$

Substituting this in Eq. 76

$$\frac{\delta E}{E} = \frac{1}{E}\int_0^{s_f} \frac{dE}{dx}\,s\;w(s)\,ds$$

$$\delta E = \frac{dE}{dx}\int_0^{s_f} s\;w(s)\,ds \qquad (87)$$

The values from this integration have been obtained for the three energies and results indicate that the energy scale is shifted downward with no appreciable broadening of the distribution. The shift in the energy scale is included in Table 7.

The accuracy of the orbit calculation can be checked by determining that the area under the weighting function, for a constant fractional change in the field, is equal to one. The integration checks within a few percent.

The finite width of the converter appears to be in between the first and second order theory because although it depends on the first order orbit perturbations, the aberration is quadratic in the width. The effect can be seen to arise due to the angle of intersection of the orbits and the detector line. If the angle were 90°, the first order perturbation orbits would exactly cancel at the focus line similar to the situation with 180° focusing. From the geometry one can show that the change in $\rho_{II}(s_f)$ for a given initial $\rho_{II}(0)$ can be written in terms of the first order solution and the angle ϕ between the focus line and the central orbit. The net effect on the energy for the 64 Mev orbit is.

$$\Delta E = 2 \frac{dE}{d\ell} \frac{\rho_{II}(s_f)\, \rho_{II}'(s_f)}{\tan \phi} \tag{88}$$

In the first approximation for the perturbation $\rho_{II}(s_f)$ and $\rho_{II}'(s_f)$ are both proportional to $\rho_{II}(0)$, therefore $\Delta\rho$ is proportional to $\rho_{II}^2(0)$. If the starred quantities are those solutions obtained by the differential analyzer, the energy shift will be:

$$\Delta E = 2 \frac{dE}{d\ell} \frac{{}^*\rho_{II}(s_f)^*\, \rho_{II}'(s_f)}{\tan \phi} \left[\frac{\rho_{II}(0)}{{}^*\rho_{II}(0)}\right]^2 \tag{89}$$

$$= k(E)\, \rho_{II}^2(0)$$

The distribution in energies resulting from this shift is given by a calculation analogous to the scattering calculation.

$$P(\Delta E)\, d(\Delta E) = P\left[\rho(0)\right]\; d\left[\rho(0)\right]$$
$$P\left[\rho(0)\right] = \text{constant} = P_1 \tag{90}$$
$$P(\Delta E)\, d(\Delta E) = \frac{P_1 d(\Delta E)}{\frac{d(\Delta E)}{d\rho}} = \frac{P_1 d(\Delta E)}{2K\,\rho_{II}(0)} = \frac{P_1 d(\Delta E)}{2\sqrt{K\,\Delta E}}$$

The result indicates a distribution proportional to the reciprocal square root of the energy. The average over energy is made by combining the distributions for the various energies, weighting the results proportional to the pair fragment distribution. The final result is shown in Fig. 48.

D. Higher Order Effects on the Energy Scale

The solutions for a finite sized converter have been evaluated assuming that the first order solution for small deviations from the central orbits can be used. In order to investigate the errors or aberrations which are caused due to higher order effects, the second order terms of the equations of Section V-B have been investigated. Judd has shown that, assuming the median plane to be flat and in this case the plane of symmetry of the magnets, the equations are of the form:

$$\rho'' + \left[\frac{1+\beta_1}{R_c^2}\right]\rho = -\left[\frac{1+2\beta_1+\beta_2}{R_c^3}\right]\rho^2 + \left[\frac{\beta_1+2\beta_2+2R_c'^2-R_cR_c''}{2R_c^3}\right]Z^2$$
$$+\left[\frac{1}{2R_c}\right](\rho'^2 - Z'^2) + \left[\frac{R_c'}{R_c^2}\right](\rho\,\rho'+Z\,Z')$$
$$Z'' + \left[-\frac{\beta_1}{R_c^2}\right]Z = \left[\frac{2\beta_1+2\beta_2}{R_c^3}\right]\rho Z + \left(\frac{1}{R_c}\right)(\rho'\,Z') + \left[\frac{R_c'}{R_c^2}\right](\rho' Z - Z'\rho) \tag{91}$$

primes are differentiation with respect to arc length

$$\beta_1 = -n = \frac{R}{H}\frac{dH}{d\hat{n}} \qquad \beta_2 = \frac{R^2}{2H}\frac{d^2H}{d\hat{n}^2} \tag{92}$$

where $\hat{n}$ is always taken as the outward normal. These coupled equations can be solved and the second order result will be sufficient to indicate the aberrations to the fourth order. The third order terms will be largely cancelled, since they are always odd in the energy deviation similar to the first order terms.

The method used to solve these equations was a series of successive approximations using the differential analyzer. If we write the equations in the form

$$\begin{aligned} \rho'' + A(s)\,\rho &= R(s, \rho, Z, \rho', Z') \\ Z'' = B(s)\,Z &= T(s, \rho, Z, \rho', Z') \end{aligned} \tag{93}$$

the first order solutions will be those for which R and T are set equal to zero. These are the homogeneous equations of Section V-B. The second order solution can be determined by substituting the first order result in R and T. The ρ equation is then:

$$\rho_2'' + A(s)\,\rho_2 = R(s, \rho_1, Z_1, \rho_1', Z_1') \tag{94}$$

By subtracting off the homogeneous solution we obtain:

$$\delta\rho_2'' + A(s)\,\delta\rho_2 = R(s) \tag{95}$$

R(s) is computed for various initial conditions and run as an input driving term in the differential analyzer for a number of cases. The input functions and the solutions for the various initial conditions are shown in Figs. 49 to 56. The effect of linearizing Eq. 93 has been studied for the most critical cases and it was found that this approximation does not introduce any significant error. Table 6 shows the summary of the results of all cases run.

By examining the form of the perturbing term one can see that for a given initial condition assumed for ρ_1 or Z_1 of their derivatives ρ_1', Z_1' a family of solutions can be derived. If $\rho_1(0)$, $Z_1(0)$,

$\rho_1'(0)$, and $Z_1'(0)$ are the initial conditions at s = 0, that is, at the converter, the solutions have been obtained for cases corresponding to $*\rho_I(0)$, $*Z_1(0)$, $*\rho_I'(0)$, $*Z_1'(0)$ and various combinations. Consider, for example, the solutions for various widths of the converter, $\rho_1(0)$. One can see that since $\rho_I(s)$ and $\rho_1'(s)$ are linear in $\rho_I(0)$, the final displacement can be related to the initial displacement as follows. Let us write the general solution $\rho_I(s)$ in terms of a particular solution $*\rho_I$ which we have solved with the analyzer.

$$\rho_I(0) = \lambda *\rho_I(0), \quad \rho_I(s) = \lambda *\rho_I(s)$$
$$\rho_I'(s) = \lambda *\rho_I'(s) \tag{96}$$

The driving term can be written in terms of the known solution:

$$R(s, \rho_I(s), \ldots) = R(s, \lambda *\rho_I, \lambda *\rho_I' \ldots) = \lambda^2 R(s, *\rho_I, *\rho_I' \ldots) \tag{97}$$

This property of the driving term simplified the results considerably. Thus, if the solution is known for $*\rho_I$, the solution for ρ_I is given in terms of λ and $*\rho_I$.

$$\delta *\rho_2'' + A(s)\delta *\rho_2 = R(s\ *\rho_1, *\rho_1' \ldots)$$
$$\delta \rho_2'' + A(s)\rho_2 = R(s\ \rho_1, \rho_1' \ldots) = \lambda^2 R(s\ *\rho_1 *\rho_1' \ldots) \tag{98}$$

or

$$\left(\frac{\delta \rho_2}{\lambda^2}\right)'' + A(s)\left(\frac{\rho_2}{\lambda^2}\right) + R(s, *\rho_1\ *\rho_1' \ldots)$$

it follows that the solution $(\delta \rho_2/\lambda^2)$ satified the same equation as $\delta *\rho_2$.

$$\delta \rho_2 = \lambda^2\ *\delta \rho_2 \tag{99}$$

Therefore the solution $\delta \rho_2(s_f)$ evaluated at the focus line is proportional to λ^2 evaluated by using (96).

$$\rho_2(s_f) = \lambda^2\ *\rho_2(s_f) = \left[\frac{\rho_1(0)}{*\rho_1(0)}\right]^2\ *\rho(s_f) \tag{100}$$

The energy change resulting from this final displacement is

$$\Delta E = \frac{dE}{d\ell}\ \delta\rho_2(s_f) = \frac{dE}{d\ell}\left[\frac{\rho_1(0)}{*\rho_1(0)}\right]^2 \delta *\rho_2(s_f) = K(R,E)\rho_1{}^2(0) \qquad (101)$$

Here we have included the dependence of the constant K on the analyzer case R for a particular energy E. From this one can obtain the energy distribution resulting from the initial width of the converter due to second order perturbations. The method is identical to the first order finite width correction which was calculated in the resolving power. With the distribution one calculates the mean value of ΔE and in this case

$$\overline{\Delta E} = \frac{\int_0^{\rho_1(0)_{max}} K\ \rho_1{}^2\ P\ [\rho_1(0)]\ d\rho_1}{\int P\ [\rho_1(0)]\ d\rho_1} = \frac{1}{3} K\ \rho_1{}^2(0)_{max} \qquad (102)$$

The shift can then be averaged over energy and the average shift applied to the data.

The second order horizontal effects which correspond to initial angles $\rho'(0)$ at the converter, are calculated in an analogous manner.

The energy shift is expressed in terms of the initial scattering angle $\rho'(0)$.

$$\Delta E\ \rho_1{}'(0) = K(R,E)\ \left[\rho'(0)\right]^2 \qquad (103)$$

The mean multiple scattering angle θ_M is given in terms of thickness

$$\rho'(0)_{rMs} \doteq \theta_{rMs} = \frac{16}{E}\sqrt{t/to} \qquad (104)$$

It follows from Eq. 103 that

$$\Delta E_{rMs} = K'(R,E)t. \qquad (105)$$

Hence the energy corresponding to the mean of the energy distribution due to scattering is proportional to t. For this second order effect one should, therefore, average over the converter thickness using

Eq. 84.

$$t_m = \frac{\int_o^t t\, W(t)\, dt}{\int_o^t W(t)\, dt} \qquad (106)$$

This procedure is only approximate for the distribution. However, the errors introduced in the mean value are sufficiently small to make it unnecessary to follow an averaging procedure similar to the first order calculations of resolving power.

In the previous discussion which derived the weighting function (Eq. 84) or loss function, the only concern was with the losses due to vertical scattering. There is an additional loss that enters through the radiation straggling distribution because the analysis of the data is made over a limited energy range. In principle one could calculate the spectrum or resolution to zero energy in which case there would be error in the mean of the resolution. In studying a line spectrum, however, it is convenient to cut off the tail of the straggling curve at an energy which corresponds to an intensity well below that useful in calculating the moments. The treatment of the first order resolution avoided the radiation straggling loss mentioned above. The radiation straggling distribution was cut off but was not renormalized before folding. In this way the final resolution function reflects the same loss as does the actual data. The treatment of the second order resolution, however, does not reflect this loss unless this effect is included in the averaging procedure. W(t) therefore should include both the scattering loss and the radiation loss. The latter amounts to a 6 percent reduction of the effective converter thickness if the integration range is ±6 Mev. In the measurement of an integrated continuous spectrum it is, of course, true that the radiation loss does not enter into the yield efficiency for various depths, providing the energy integration range is broad. Thus the comparison of the π^o spectrum with the scattering losses in Fig. 41 is valid.

Since the multiple scattering is statistically independent, we can approximate the pair by one particle with a scattering angle $\sqrt{2}$ times that of one member. The form of distribution is as follows.

$$p(\Delta E)\, d(\Delta E) = K_1 \frac{e^{+K_2(\Delta E)}}{(-\Delta E)^{1/2}}\, d(\Delta E) \qquad (107)$$

(ΔE is negative)

K_1 and K_2 are known constants derived from Eqs. 105 and 106 and include the 6 percent correction above. This distribution is derived from the gaussian angular distribution of the initial angle ρ' and the constants depend upon the analyzer results, and the mean converter thickness.

From the gaussian property of the primary distribution the shift in the energy scale will be the same as the energy change of one particle starting at the converter with twice the mean squared angle. The distribution is shown in Fig. 57. The distribution has been folded into the resolution.

The cross terms in the horizontal plane between ρ and ρ', which are obtained from the calculations on the analyzer, are a small effect and for the purpose of getting the correct shift of the energy scale an average was made over the first four cases and then averaged over the three energies. The solutions in the horizontal plane are subject to a check which verifies the main effects. The results obtained by preliminary long hand calculations made similarly to the precise orbit calculation are available for these two effects. Also the results as calculated for the spectrometer with a uniform field up to the edge of the pole tip can be compared to the case examined at a point on the edge of the tip. In both cases, the agreement is satisfactory within the accuracy of the preliminary results. The second order of refocusing of the lateral width effect is clearly indicated, and the magnitude of the scattering effect is also verified.

The calculations of the effects of vertical scattering and the finite height of the converter are inherently more complicated for the

following reasons. The main effect in the vertical perturbations is due to the field lines which are crowded together at the edges of the pole tip. Therefore, if the orbit starts out in such a direction so as to pass close to the top or bottom of the pole tip as is leaves the magnet the perturbing effect on the energy will be severe. This means that the Z and Z' separation is not likely to be at all satisfactory. The addition of the requirement that the particle arrive at the detector is similar in its cross coupling of Z and Z'. The situation is considerably simpler analytically if we begin by making the approximation that we may replace the pair by one particle with twice the mean square scattering angle.

The results of the analyzer for second order energy perturbations due to Z motion can be summarized by an empirical formula which fits a majority of the cases within a few percent.

$$\Delta E = A\, Z^2(0) + B\, Z'^2(0) + C\, Z(0)\, Z'(0) \qquad (108)$$

The constants A, B, C can be found by suitably averaging over the analyzer cases 5-10 involved, Table 6. A and B are seen to be cases 5 and 6. The coefficient C turns out to be nearly a constant for a set of cases whether Z' or Z changes its sign, cases 7 - 10.

The solution of the problem then involves a type of folding operation which is easily generalized from the previous illustration.

The energy ΔE can be written in a functional form

$$\Delta E = f(Z, Z') \qquad (109)$$

and the probabilities $Q(Z)$, and $S(Z')$ of finding Z and Z' are known. Since Z and Z' are statistically independent, the probability of occurrence of Z and Z' is

$$T(Z, Z') = Q(Z)\, S(Z') \qquad (110)$$

This distribution may be expressed in terms of ΔE and Z'.

$$T(Z, Z')dZdZ' = Q\left[Z(\Delta E, Z')\right] S(Z')\, J\left(\frac{Z, Z'}{\Delta E, Z'}\right) d(\Delta E)dZ'$$

$$= \rho(\Delta E, Z')\, d(\Delta E)dZ' \qquad (111)$$

From the form of $f(Z, Z')$ Eq. 108, the Jacobian is

$$J\left(\frac{Z, Z'}{\Delta E, Z'}\right) = \frac{1}{\sqrt{K_1 \Delta E + K_2 Z'^2}} \tag{112}$$

where K_1 and K_2 are given in terms of A, B and C.
If the illumination is uniform

$$Q(Z) = \text{constant} \tag{113}$$

Now $S(Z')$ is a gaussian of width θ_M

$$S(Z') = \frac{1}{\sqrt{2\pi}\ \theta_M}\ e^{-\frac{1}{2}\left(\frac{Z'}{\theta_M}\right)^2} \tag{114}$$

thus substituting from the above equations

$$\rho(\Delta E, Z') = k\ \frac{e^{-k'Z'^2}}{\sqrt{K_1 \Delta E + K_2 Z'^2}} \tag{115}$$

for which all the constants k, k', K_1, and K_2 are given in terms of A, B, C, etc.
The distribution in ΔE may be found by integrating over Z

$$\rho(\Delta E) = k' \int_{Z'(\Delta E)_{min}}^{Z'(\Delta E)_{max}} \frac{e^{-k'Z'^2}}{\sqrt{K_1 \Delta E + K_2 Z'^2}}\ dZ' \tag{116}$$

The limits in Z' of this integral are not immediately obtained in a simple form, because they are functions of the particular value of ΔE. To get a picture of what these limits are, consider the three dimensional plot of the surface given by Eq. 108 for ΔE as a function of Z and Z'. The main boundaries of this surface are determined by the acceptance zone at the detector. These were shown in Fig. 40. If the surface is projected into the ΔE, Z' plane these limiting surfaces appear as quadratic curves and will in general overlap. Figure 58 shows the result

when calculated for the numerical case under consideration. The lower outline of the curve is obtained by evaluating the appropriate minimum condition. The surface is always concave upwards and the valley which occurs in the middle of the acceptance zone indicates those particles passing through the region at the edge of the pole tip near the median plane.

The limits of integration of Eq. 116 are seen to be the extremities of the projected curve. The integral has been preformed for a series of ΔE increments and the probability distribution is shown in Fig. 59. This function has been folded into the resolution. The final resolution curve is shown in Fig. 60 with the data.

The errors which are introduced by making the single particle approximation are not easily determined and the major effect comes from the cross term of Eq. 108. The constant B is additive in the r.m.s. value. However the effective size of C will be reduced with two particles.

When the exact expressions are used integration becomes tedious since the folding integral and the limits of integration are still more complicated. We have carried out this integration and the result is similar to the result of the simplified calculation.

Cases 11-14, Table 6 are the remaining higher order cross coupling effects studied by the analyzer. These cases are seen to be combinations of the second order cross coupling effects. The values for the latter were subtracted from the appropriate cases 11-14 and the residuals averaged together and applied as changes in the mean value of the energy. The values of all the shifts in the energy scale are tabulated in Table 7.

VI. EXPERIMENTAL RESULTS AND CONCLUSIONS

The data for the precision measurements were taken with a converter thickness chosen to minimize the error due to the statistical uncertainty of the data. The procedure followed was to run various converter thicknesses spending a bare minimum of time on the low yield rates of the hydrogen capture gamma ray for the purpose of checking the resolution for various target thicknesses. The data with 0.050 in. tantalum converter are shown in Fig. 61. Fig. 62 shows the result as obtained with 0.020 in. tantalum converter. Fig. 63 shows the 0.010 in. data from which the mass value was obtained. The values of the mass and the estimated widths are given in Table 7. The solid lines of Figs. 61 and 62 are rough theoretical resolution curves for the thick targets which were obtained by extrapolating the results from the accurate resolution theory. The data resulting from the previous mass determination by Panofsky, et al. are shown to contrast the resolution of the two spectrometer designs.

When the converter became prohibitively thin, the remaining dependence of yield as a function of converter thickness was run using the decay gamma rays from neutral pions produced by protons on wolfram as shown in Fig. 41. This test had the dual purpose of checking the efficiency of various thicknesses of converter and determining the presence of any significant energy dependent losses resulting from scattering of pair fragments so as to miss the detectors. A further attempt was made to determine the effectiveness of the collimation. The 280 Mev neutron beam from an internal target of beryllium was used to check the gross alignment. An x-ray film was exposed to the beam, and a microphotometer trace was made across the major axes of the beam, as shown in Fig. 26. It is apparent that there is probably only a small loss due to the edges of the collimating system. The results obtained with the yield vs. converter area data taken for several converter shapes are shown in Fig. 62. The change of efficiency due to the second order corrections to Z solutions of Eq. 65 is such as to

decrease the yield. The uncertainty of the edge loss is a maximum of ~10 percent of the efficiency of the outer 1/2 in. wide zone of the converter. The effect on the energy scale has been included with the evaluation of the sources of errors.

It should be emphasized that, throughout the experimental runs, the lack of a sufficient flux of monochromatic gamma rays prevented for the most part any detailed investigation into the behavior of the spectrometer. The checks for various converter sizes and thicknesses do provide gross agreement with the theory and, where they have been made, they add to our confidence in the theory of the spectrometer.

There is one additional measurement of the energy dependence of the efficiency of the spectrometer which has been investigated by measurements on the neutral pion spectrum. The 180^{o} spectrum from 340 Mev protons on wolfram was measured with the conventional design spectrometer with the counters located along the edge of the magnetic field. The energy dependent losses in this spectrometer are estimated by varying the magnetic field keeping the mean scattering angle constant by choosing the converter thickness appropriately. The data are shown in Fig. 65. These data were obtained in connection with π^{o} studies of Crandall et al.[24] The same source of γ-rays was measured with the focussing spectrometer with the central field at the same value as used in the meson mass measurement. The data are shown in Fig. 66. Corrections which take into account the number of channels which are available for each energy and the variation of the pair production cross section were applied in the reduction of both data.

The major test of the theory of the spectrometer is in the agreement of the theoretical resolution with the data. The data obtained for the mass measurement are given in detail in Table 8. The data and resolution were shown in Fig. 60. An error based on the amount of apparent disagreement has been included in the probable error of the meson mass obtained.

Concerning the background of gamma rays coming from the empty hydrogen vessel, this is very meager information. A run on the background was made to discover whether any shape could be observed in the region about 130 Mev, and none was found within statistics. The data are shown in Fig. 67. The result as measured with the neutral pion decay gamma rays shows remarkable similarity. One is inclined to attribute most of the background to neutral pions for these reasons. Therefore, a smoothed correction has been subtracted from the hydrogen data. The normalization of this correction is made such as to reduce the counts attributed to hydrogen to zero in the region well outside of the interest region. This procedure seemed to be the most reliable of those considered, and a probable error of as little as 10 percent of the correction is quite doubtful. The error in the spectrum due to treatment of the background is extremely small since only 10 percent of the maximum value of the hydrogen spectrum is affected. The resulting error in the mass evaluation due to this effect has been included. Other possible sources of gamma rays due to reactions with hydrogen are at most only a few percent in intensity due to the narrow region under consideration. This can be shown[64] with a reasonably conservative estimate for the other known processes which may occur. The effect of no-converter was measured in two ways. First, the ratio of signal with the tantalum converter in place to no-converter signal was measured on neutral pion gamma rays and the value of 9 ± 0.5 to 1 was obtained. Second, the hydrogen effect was observed to determine if this background signal was strongly peaked at 130 Mev. Only enough data were accumulated to show that the signal from the beryllium converter holder (4 ± 2 percent) and from air and pole conversion (the remaining 6 percent) do not appear to be distributed in an obviously anomalous way. Electronic cross talk, and noise pickup were also effectively eliminated as sources of error. It is reasonable to assume there are no processes that would cause stray counts to be introduced in such a manner as to satisfy the pair fragment unique channel requirements for a range of only 5 percent of the total efficiency.

The no-converter spectrum of neutral pions has been run with the 90 degree apex angle spectrometer and the results for gamma rays is at most an effective increase in efficiency toward low energy of an order of magnitude of 10 percent from maximum to minimum energy. Here the agreement for the two geometries of the neutral pion spectrum with converters eliminates the possibility of any gross effect. The probability of error due to these effects is apparently remote.

Finally an effect due to changing efficiency during the run will be considered briefly. The angle of passage through the proportional counter depends on the energy of the fragment. Therefore one would expect that the smaller path length particles would be counted with less efficiency as the stability of the equipment varies the threshold of the proportional counter. During the week's run on the spectrum such instability was observed and perhaps the fit of the hydrogen data to the background shows a possible effect in the high energy region, although this is only slightly significant statistically. This effect could therefore introduce an error similar to those considered above, and the error over the region under observation is of the order of a few percent of the maximum hydrogen signal.

The evaluation of the mass and the error of the mass has been done in the following way. The first moment of the data have been computed by weighting each point by the number of counts:

$$\overline{E} = \frac{\Sigma N_i E_i}{\Sigma N_i} \qquad (117)$$

N_i = number of counts corrected for background and energy channel efficiency. This result was then matched to the first moment of the theoretical resolving power. The data was also fitted to the resolution by eye to minimize the statistical errors. The values obtained are in good agreement. This method determines the energy of the gamma ray responsible for the spectrum observed from

which the mass was calculated. The details of the calculation are found in Table 9.

The error of the moment can be computed using a crude theory of the statistical errors. The method used as based on the assumption that the resolving power was gaussian down to approximately 10 percent of the peak value. The degree to which this is a good approximation is seen in Fig. 68. The error was calculated by dividing the R.M.S. width of the equivalent gaussian by the square root of the number of counts contained within this region. Since the statistics is only a small fraction of the total error; further analysis seems to be unwarranted. Table 10 summarizes all the errors associated with the mass value.

As pointed out in the introduction there are several other values of particle masses which are directly connected to the pion mass. The masses of the π^o and both μ's can be found and are given in Table 1. The errors given are combined from the above error and the various errors quoted by the other workers. No attempt has been made to evaluate the accuracy of these assigned errors.

The value of the pion mass and the desirable masses as obtained from this measurement is in fair agreement with the majority of previous measurements. The previous experiment based on the same type of measurement is approximately two probable errors higher than the present result. As yet there is no satisfactory explanation of the discrepancy other than the statistical inaccuracy of the early work as mentioned in Sect. I-B. Only a gross error in the present experiment would allow any appreciable reduction of the disagreement. The most accurate independent work by Smith, et al., is unfortunately not complete at the present time. Their preliminary result is quoted in Table 1. Their results indicate a reduction from the published values for reasons already discussed by Barkas.[65]

VII. ACKNOWLEDGMENTS

The author takes pleasure in acknowledging the assistance so generously offered by members of the Radiation Laboratory staff. Professor W. K. H. Panofsky of Stanford University had guided the entire program. Dr. Robert Phillips has been a patient partner in all phases of the work. Professor A. Sachs of Columbia University pointed out the focussing property of the 90 degree wedge. The magnetic measurements group, under Mr. Duane Sewell, contributed over a thousand field measurements. Mr. Robert Teeters set up the field measurements and made the preliminary field calculations from which the spectrometer design was made. The lengthy reduction of the precise field measurements was made by Mr. Harold B. Knowles and Mr. Glen Lambertson. The calculations of the orbits were made by Mrs. Ardith Kenney and other members of the computing section of the theoretical group under Mr. John Killeen. Dr. Louis Henrich and Dr. David Judd suggested the method of approach that was used. The design and construction of the equipment represents the joint effort of most of the shops in the Laboratory. The cyclotron crew, under Mr. James Vale, provided the bombardments which lasted over a week. The real credit for the success of the experiment, however, belongs to the people who did many hours of tedious work, accurately and skillfully, within the groups named above.

VIII. REFERENCES

1. W. K. H. Panofsky, L. Aamodt, J. Hadley, Phys. Rev., 81, 565 (1951) and Private Communications, Phys. Rev., 80, 94, 282 (1950). W. K. H. Panofsky, L. Aamodt, H. F. York, Phys. Rev. 78, 89 (A), 825 (1950).

2. L. Lederman, J. Tinlot, E. T. Booth, Phys. Rev., 81, 281 (1951). W. M. Powell, Private Communication.

3. W. Birnbaum, F. M. Smith, W. H. Barkas, Phys. Rev. 83, 895 (A) (1951).

4. C. D. Anderson, S. H. Neddermeyer, Phys. Rev., 50, 263, (1936), Phys. Rev. 54, 88, (1938), Phys. Rev., 51, 884 (1937).

5. J. A. Wheeler, R. Ladenburg, Phys. Rev. 60, 754 (1941), R. B. Brode, Rev. Modern Phys. 21, 37 (1949), Phys. Rev. 75, 904 (1949) and W. B. Fretter, Phys. Rev. 70, 625 (1946).

6. J. G. Retallack, R. B. Brode, 75, 1716 (1949). D. R. Corson, R. B. Brode, Phys. Rev. 53, 776 (1938).

7. T. C. Merkle, E. L. Goldwasser, R. B. Brode, 79, 926 (1950).

8. H. A. Bethe, Phys. Rev., 70, 821 (1946).

9. Smith, Barkas, Bradner, Gardner, Phys. Rev. 78, 86 (A) (1950).

10. Bradner, Smith, Barkas, Bishop, Phys. Rev. 77, 462 (1950).

11. W. H. Barkas, F. M. Smith, E. Gardner, Phys. Rev. 82, 102 (1951).

12. F. M. Smith, Private Communication.

13. W. Birnbaum, Private Communication.

14. C. F. Powell, Reports on Progress of Physics, The Physical Society, (London), Vol. XIII, 350 (1950).

15. H. Bradner, Review of Work on Artifically Produced Mesons, UCRL-486 (1949).

16. Camerini, Muirhead, Powell, Ritson, Nature 62, 433 (1948).

17. S. Lattimore, Nature 161, 518 (1948). Goldschmidt-Clermont, King, Muirhead, Ritson, Proc. Roy. Soc. 61, 183 (1948).

18. J. Tiomno, J. A. Wheeler, Rev. Modern Phys. 21, 144 (1949).

19. L. Michel, Proc. Phys. Soc. 63A, 514 (1950), Nature, 163, 959 (1949).

20. R. B. Leighton, C. D. Anderson, A. J. Serif, Phys. Rev. 75, 1432, (1949). R. Sagane, W. L. Gardner, H. W. Hubbard, Phys. Rev., 82, 557 (1951). O. Halpern, H. Hall, Phys. Rev. 78, 320 (A) (1950). H. W. Hubbard, Thesis, University of California, (1952).

21. W. F. Cartwright, Phys. Rev. 82, 460 (L) (1951), Thesis, University of California (1951).

22. V. Z. Peterson, E. Iloff, D. Sherman, Phys. Rev. 84, 372 (1951), Phys. Rev. 81, 647 (A) (1951). V. Z. Peterson, Phys. Rev. 80, 136 (A) Thesis, University of California, (1950).

23. A. G. Carlson, J. E. Hooper, D. T. King, Phil. Mag. 41, 701 (1950).

24. Bjorkland, Crandall, Moyer, York, Phys. Rev. 77, 213 (1950). Crandall, Crowe, Panofsky, Phillips, Walker, Phys. Rev. 83, 893 (A) (1951). W. E. Crandall, Thesis, University of California and Private Communication.

25. A. Sachs, J. Steinberger, Phys. Rev. 82, 973 (L) (1951), and Private Communication with Dr. Steinberger.

26. W. E. Hazen, Phys. Rev. 67, 269, (1945).

27. R. H. Frost, Thesis, University of California, (1947).

28. J. K. Bowker, Phys. Rev. 78, 87 (A) (1950).

29. B. Rossi, K. Greisen, Rev. Modern Phys. 13, 240, (1941). H. Bethe, Nuclear Physics, edited by E. Segrè. To be published by Wiley.

30. W. Heitler, The Quantum Theory of Radiation. Oxford University Press, Oxford (1944).

31. H. Yakawa, Proc. Phys.--Math. Soc., Japan, 17, 48 (1935).

32. E. F. Salpeter, Phys. Rev. 82, 60 (1951).

33. H. E. Hart, R. D. Hatcher, Phys. Rev. 87, 375 (L) (1952).

34. M. Born, Rev. Modern Phy. 21, 463 (1949).

35. A. Pais, G. E. Uhlenbeck, Phys. Rev. 79, 145 (1950).

36. H. J. Bhabha, The Phil. Mag. 336, 33 (1952).

37. H. J. Bhabha, Rev. Modern Phy. 17, 200 (1945).

38. B. T. Darling, Phys. Rev. 80, 460 (1950).

39. P. R. Zilsel, Phys. Rev. 82, 557 (1951).

40. D. Bohm, M. Weinberg, Phys. Rev. 74, 1789 (1948).

41. R. L. Walker, B. D. McDaniel, Phys. Rev. 74, 315 (1947). B. D. McDaniel, G. V. Dardel, R. L. Walker, Phys. Rev. 72, 985 (1947).

42. C. R. Emigh, Phys. Rev. 86, 1028 (1952). J. W. DeWire, A. Ashkin, L. A. Beach, Phys. Rev., 82, 447 (1951), Phys. Rev. 83, 233 476, 505 (1951). J. L. Lawson, Phys. Rev. 75, 433 (1949). C. D. Curtis, Phys. Rev. 81, 308 (1951).

43. F. Bloch, W. W. Hansen, M. Packard, Phys. Rev. 70, 474 (1946).

44. C. A. Harris, Radiation Laboratory Magnet Regulators, Service and Operation, UCRL-520.

45. J. B. Scarborough, Numerical Mathematical Analysis, John Hopkins Press (1930).

46. L. J. Comrie, Interpolation and Allied Tables, His Majesties Stationery Office, London (1936).

47. Tables of Lagrangian Interpolation Coefficients, Columbia University Press (1944).

48. E. G. Sorensen, Construction and Maintenance Report on the UCRL Synchro-Driven Differential Analyzer, UCRL-1717 (1951).

49. J. Killeen, The UCRL Differential Analyzer (in process).

50. G. M. Nonnemaker and J. C. Street, Phys. Rev. 82, 564 (1951).

51. L. Van Rossum, Comptes Rendus, 228, 676 (1949).

52. Brown, Camerini, Fowler, Heitler, King, Powell, Phil. Mag. 40, 862 (1949). Brown, Camerini, Fowler, Muirhead, Powell, Ritson, Nature 163, 42, 82 (1949).

53. I. Barbour, Phys. Rev. 74, 507 (1948), Phys. Rev. 76, 320 (1949), Phys. Rev. 77, 751 (1950), Phys. Rev., 78, 518 (1950).

54. C. Franzinetti, Phil. Mag. 41, 86 (1950), Cosmic Radiation Interscience Publications, 159, (1949).

55. R. L. Mather, E. Segrè, Phys. Rev. 84, 191 (1951). C. J. Bakker, E. Segrè, Phys. Rev. 81, 489 (1951).

56. W. F. G. Swann, J. Franklin Inst. 226, 598 (1938). E. Fermi, Phys. Rev. 56, 1242 (1939), Phys. Rev. 57, 485 (1940). G. C. Wick, Nuovo Cimento, 1, 302 (1943). Ricerca Sci. 11, 273 (1940). O. Halpern, H. Hall, Phys. Rev. 57, 459 (1940), Phys Rev., 73, 477 (1948).

57. L. Landau, J. Phys. 8, 201 (1944). K. R. Symon, Harvard University, Thesis, (unpublished) (1948). A. Bohr, Kgl. Danske Videnstab. Selskab Mat.-fys. Medd. 24, No. 19 (1948).

58. T. Bower, F. X. Roser, Phys. Rev. 83, 689 (1951). F. X. Roser, T. Bower, Phys. Rev. 82, 284 (1951), Phys Rev. 85, 992 (1952). R. Hofstader, A. Hudson, Phys. Rev. 88, 589 (1952). W. L. Wittemore, J. C. Street, Phys. Rev. 76, 1786 (1949). E. L. Goldwasser, F. E. Mills and A. O. Hanson, Phys. Rev. 88, 1137 (1952). D. Clark, R. Eisberg, G. Igo, Letter to be submitted to Phys. Rev.

59. J. W. M. DuMond, E. R. Cohen, American Scientist, 40, 447 (1952).

60. J. Robson, Phys. Rev. 83, 349 (1951). Hornyak, Lauritsen, Morrison, Fowler, Rev. Modern Phys. 22, 291 (1950).

61. H. A. Thomas, R. L. Driscoll, J. A. Hipple, Phys. Rev. 75, 902 (1949), Phys. Rev. 78, 787 (1950).

62. N. F. Ramsey, Phys. Rev. 77, 567 (1950).

63. H. A. Thomas, Phys. Rev. 80, 901 (1950).

64. R. H. Phillips, Thesis, University of California (1952).

65. W. H. Barkas, Am. J. Phys. 20, 5 (1952).

TABLE I
Summary of Meson Mass Measurements

Particle Type	Mass Values	Method	Comments	Reference
$\mu^+\mu^-$	202 ± 5 212 ± 5	($H\rho$) R Same data, different statistical analysis	26 mesons	5
$\mu^+\mu^-$	215 ± 2 215 ± 4	$\Delta\theta$, R	Grand average 37 events	6
$\mu^+\mu^-$	196 ± 3	Cloud Chamber $H\rho$; R	25 - mesons 23 + mesons	7
$\mu^+\mu^-$	220 ± 12	$H\rho$ -R		50
μ^+	217 ± 4	Cloud chamber $\mu^+ \rightarrow \beta^+ + 2\nu$ end point	Cosmic ray	20
μ^+	214 to 206 (± 6)	Spectrometer $\mu^+ \rightarrow \beta^+ + 2\nu$ end point	Artificial Mesons. Value depends upon theory of μ decay	20
$\pi^- - \mu^-$	66 ± 3	Cloud chamber decay in flight $\pi^- \rightarrow \mu^- + \nu$	Artificial Mesons (25 events)	2
$\pi^+ - \mu^+$	63 ± 2	$\pi^+ \rightarrow \mu^+ + \nu$	Artificial Mesons 22 events	2
π^-	264 + 26 - 22	Grain count	18 mesons	15, 28
π^-	280 ± 15	Grain count	13 mesons	51

TABLE I
(continued)

Particle Type	Mass Values	Method	Comments	Reference
π^+,π^-	272 ± 12	Scattering	Nuclear Emulsions	17
$\mu^+\mu^-$	202 ± 8	Scattering	Nuclear Emulsions	17
π^-	290 ± 80	Scattering	30 events	17
$\pi^+\pi^-$	290 ± 20	Range grain count	Nuclear Emulsions	52
π's μ's	270 ± 23 220 ± 26	Momentum range	Cosmic ray particles	53
π^+ μ^+	281 ± 7 217 ± 4	$H\rho$ R in plates	Cosmic ray events	54
$\pi^+\pi^-$	283 ± 7	Grain counting scattering		16
$\pi^+\pi^-$ $\mu^+\mu^-$	276 ± 6 210 ± 4	$H\rho$ R $H\rho$ R	Artificial Mesons	9,10,15
π^+ π^-	277.4 ± 1.1 276.1 ± 1.3	Ratio to protons by range and momentum		11
π^+ π^-	~273.5 ~273.0	Ratio to protons by range and momentum	Latest values from work in progress *	12

TABLE I
(continued)

Particle Type	Mass Values	Method	Comments	Reference
$\pi^+-\mu^+$	66.46 ± 0.16	Decay momentum ratio method and difference		3
π^+	276.1 ± 2.3			
μ^+	209.6 ± 2.4	Decay momentum ratio method and difference		
π^+/μ^+	1.318 ± 0.004	Ratio method		
$\pi^+-\mu^+$	66.50 ± 0.15	Decay momentum ratio method and difference	Research in progress, latest value is reported*	13
π^+	273.7 ± 2.0			
μ^+	207.2 ± 2.0	Decay momentum ratio method and difference		
π^+/μ^+	1.321 ± 0.003	Ratio method		
π^+	275.1 ± 2.5	$P + p \rightarrow \pi^+ + d$		21
π^+	279.0 ± 1.5	$p + p \rightarrow \pi^+ + d$		22
π^-	275.2 ± 2.5	$\pi^- + p \rightarrow n + \gamma$		1
π^-	278.0 ± 2.5	$\pi^- + p \rightarrow n + \gamma$	Ionization loss correction made	1
π^o	280.0 ± 10.0	γ spectrum 340 Mev protons on carbon	Error does not include errors due to contamination	24
π^o	295.0 ± 20.0	γ spectrum cosmic rays		23
$\pi^- - \pi^o$	10.6 ± 2.0	$\pi^- + p \rightarrow \pi^o + n$	Doppler shift	1

TABLE I
(continued)

Particle Type	Mass Values	Method	Comments	Reference
π^-	= 273.5 ± 0.5	Present method		
π^o	= 262.9 ± 2.1	Present method and difference		1
μ^-	= 207.5 ± 3.0	Present method and difference		2
μ^+	= 207.0 ± 0.6	Present method and difference		3

* These values have been supplied by the experimenters as current values and it should be noted that both the central value and probable errors are subject to modification upon the completion of the work.

TABLE 2

Magnetic Field Analysis

A. Proton Moment Data	
1. Frequency readings:	± 0.003 %
2. The accuracy of the location of signal depends strongly on quality of pattern and width of pattern. Average deviation of repeated measurements:	≤ 0.02 %
3. Centering of probe where points were used:	<< 0.01 %
4. Stability of fields:	≤ 0.01 %
5. Reproducability of results indicates changes of uniformity for various central field values. Effect reduced to:	<< 0.01 %
6. Agreement with over lapping slip run measurements:	± 0.012 %
7. Frequency standard:	<< 0.01 %
8. The number of points used ~250 independant measurements:	
9. Total assigned error:	± 0.015 %
B. Flip Coil Data	
1. Reading accuracy ± 0.3 mm on fluxmeter scale:	± 0.016 %
2. Positioning accuracy:	<< 0.01 %
3. Errors in calibration:	± 0.016 %
4. Total error assigned for each point:	± 0.02 %
C. Slip Coil Data	
1. Reading accuracy:	± 0.017 %
2. Positioning checked in high gradient maximum error:	± 0.056 %
3. Errors accumulated in loops at 16 inches. Standard deviation:	± 0.088 %
4. Consistancy for single measurements standard deviation for points overlapped:	± 0.025 %

TABLE 2
(continued)

5. Influence of varying the conversion constant to eliminate accumulated errors and positioning errors. Standard deviation:	± 0.072 %
6. Number of points used (three or more readings averaged for each point.):	900 points
7. Total error assigned to each point:	± 0.03 %
D. Cancellation Data	
1. Sensitivity 1 mm on flux meter scale equivalent:	± 0.011 %
2. Position of electrical center of rotor used in high gradients ~2 mm excursion on rotation. Error:	± 0.011 %
3. Readings of end point settings for limit switches:	± 0.005 %
4. End point reading in measurement:	± 0.008 %
5. Proton moment monotoring of spectrometer magnet:	± 0.005
6. Proton moment monotor of slave magnet	± 0.01 to ± 0.02
7. Error of calibration of fluxmeter reading:	≤ ± 0.003
8. Error of area ratio:	± 0.015
9. Reproducibility including errors of repositioning:	± 0.025
10. Error of correction due to the magnetization effect on uniformity of slave field:	± 0.017
11. Total number of points used:	- 32
12. Total error assigned to each point:	± 0.03

TABLE 2
(continued)

E. Template Accuracy

1. Location of holes: ± 0.002 in.
   (As measured from reference center line.) Contribution to field accuracy: ≤ 0.01 %

2. Fit of pinned holes in plate as measured by actual deflections of fluxmeter readings: < 0.005 %

3. Relative position of pole tip, template etc. No observable effect as seen in reproducability of results in large gradients: ≤ ± 0.01 %

F. Total Error Due To Field

1. The errors are estimated.
   A. Proton moment region: ± 0.015 %
   B. High gradient region: ± 0.060 %
   C. Low field region: ± 0.035 %
   These values are the estimated standard deviation for each value in the region.

2. Weighting factors (W_i) as evaluated from theoretical weighting analysis. (fig. 33)

	49 Mev	81 Mev
A	0.526	0.602
B	0.433	0.597
C	0.328	0.338

3. The weighted errors combined

$$\bar{E} = \sqrt{\Sigma W_i \varepsilon_i^2}$$

49 Mev--- $\bar{\varepsilon} = 0.046$ %

81 Mev--- $\bar{\varepsilon} = 0.057$ %

4. Combined percent probable error averaged over energy

$$0.67 \frac{\bar{\varepsilon}_{49} + \bar{\varepsilon}_{81} + \bar{\varepsilon}_{65}}{3} = 0.035 \%$$

TABLE 3

x → / y ↓	0	1	2	3	4
0	100000 100053	100103 100155	100186 100213	100239 100271	100304 100338
	99980 100059	100114 100139	100174 100191	100210 100242	100280 100324
-1	99930	100014 100059	100098 100106	100129 100165	100212 100273
			99918 99851	99856 99912	100009 100125
-2				99292 99411	99597 99812
				98113 98361	98748 99194
-3				95928	97159 98027
					94554
-4					90855
					86275
-5					
-6					
-7					
-8					61766
-9		53777			
-10	46247	48907			55071
					53039
-11	40082	43033			50704
					48025
-12	33968	36827			45120
					42059
-13	28419	31004		36266	38948 40327
				33316	35905 37233
-14	23728	25909	28187	30549	32969 34220
				29080	30223 31383
-15	19806	21645	23566 24553	25561 26605	27658 28732
		19784	21546 22443	23362 24316	25296 26280
-16	16565	18085	19694 20514	21360 22235	23129
	15156	16532 17249	17984 18734	19503 20302	21115

TABLE 3
(continued)

x → / y ↓	0		1		2		3		4
-17	13873 12703	14494 13265	15115 13826	15758 14401	16418 14992	17099 15607	17830 16244	18532	19264 17579
-18	11633 10643	12142	12651 11573	13164 12030	13692 12506	14249	14828 13611		16042
-19	9742		10589		11425		12394		13356
-20	8220		8879		9533		10304		11121
-21	6937		7441		7951		8569		9232
-22	6277				6681		7177		7703
-23					5624		6008		6422
-24					4774		5086		5397
-25					4062		4311		4579
-26							3662		3896
-27							3072		3314
-28							2540		2759
-29									2251
-30									1814
-31									1463
-32									1076

TABLE 3
(continued)

x → / y ↓	5		6		7		8		9	
0	100366	100380	100387				100407			
	100363	100385	100396							
-1	100330	100355	100382							
	100236	100291	100347	100380	100393					
-2	100018	100160	100256	100329	100371	100418	100444			
	99620	99883	100089	100231	100316	100392	100428			
-3	98859	99409	99796	100059	100190	100318	100385	100410		
	97563	98591	99286	99727	99999	100212	100331	100367	100403	
-4	95506	97212	98395	99186	99686	100024	100218	100313	100360	100396
	92482	94987	96984	98282	99129	99685	100022	100176	100295	100356
-5	88588		94837	96846	98231	99131	99693	99992	100178	100286
	84089		91780	94700	96780	98229	99146	99670	99977	100161
-6	79369		87836	91640	94637	96772	98239	99123	99642	99966
	74919		83343	87707	91574	94593	96780	98210	99091	99627
-7	70975		78678	83194	87655	91518	94566	96748	98173	99066
	67695		74297	78526	83125	87587	91472	94533	96705	98143
-8	64983		70405	74136	78438	83073	87520	91453	94496	96665
	62714		67105	70248	74014	78356	83015	87432	91339	94449
-9	60780		64316	66891	70098	73876	78258	82889	87340	91293
	58984		61946	64030	66664	69864	73709	78092	82742	87266
-10	57192	58375	59783	61539	63701	66353	69592	73477	77893	82621
	55235	56385	57683	59226	61059	63237	65974	69326	73194	77706
-11	53072	54255	55523	56927	58575	60435	62689	65524	68983	72879
	50579	51827	53122	54544	56055	57763	59703	62098	64983	68477
-12	47837	49159	50508	51912	53437	55011	56821	58891	61397	64337
	44841	46212	47606	49066	50579	52159	53831	55762	57951	60525
-13	41722	43116	44536		47523		50749	52541	54566	56837
	38585	39955	41360		44320		47481		51119	
-14	35504	36822	38184		41066		44145		47602	
	32589		35132		37857		40806	42373	44045	
-15	29840		32208		34750	36110	37529	38992	40544	
	27397		29546		31826		34393	35720	37166	
-16	24954		26958		29084		31417		33937	
			24546		26506		28620		30883	

TABLE 3
(continued)

x → / y ↓	5		6		7		8		9	
-17	20.759		22401 20427		24420 21981	22798	26020 23,651		28058	
-18	17276		18,623	19300	19994 18168	20716 18832	21,484		23048	
-19	14334		15424 14037		16532 15010		17704		18898	19521
-20	11906 10837		12774 11616		13,622		14546		15,443	15911
-21	9862 8,978		10560		11,238		11934		12599	12945
-22	8180		8727		9272		9803	10051	10296	10552
-23	6821		7247		7,657		8042	8232	8,418	8601
-24	5,700		6029		6351		6637	6778	6917	7059
-25	4800		5061		5312	5423	5527	5628	5725	
-26	4,078		4281		4483	4574	4655	4,722	4783	
-27	3457		3637		3,798	3879	3954	4012	4063	
-28	2886		3066	3140	3210	3290	3364		3453	
-29	2361		2518	2591	2664	2742	2814		2918	
-30	1883	1969	2044	2105	2163		2304		2413	
-31	1487	1546	1606	1666	1726		1848		1931	
-32	1182	1215	1255	1304	1356		1454		1531	

TABLE 3
(continued)

x⟶ / y↓	6	7	8	9
-33	0992	1124	1136	1198
-34		0891	0881	0928
-35		0717	0688	0722
-36			0531	

TABLE 3
(continued)

x ⟶ / y ↓ / 0	10		11		12		13
-1							
-2							
-3							
-4	100.416		100.424				
	100.402	100.468					
-5	100.352	100.412					
	100.276	100.326					
-6	100.144	100.253	100.319		100.348		
	99.955	100.124	100.230	100.295			
-7	99.612	99.934	100.104	100.195	100.254		100.257
	99.041	99.589	99.905	100.074	100.153	100.218	
-8	98.112	99.015	99.558	99.864	100.034	100.147	100.160
	96.624	98.079	98.979	99.522	99.812		100.056
-9	94.393	96.587	98.035	98.952	99.469		99.915
	91.234	94.333	96.536	97.976	98.856		99.673
-10	87.172	91.139	94.249	96.427	97.894	98.869	99.278
	82.458		91.004	94.059	96.336	97.872	98.654
-11	77.457		86.827	90.746	93.951	96.216	97.615
	72.488		81.854	86.467	90.584	93.703	95.990
-12	67.855		76.598	81.499	86.217	90.148	93.493
	63.566		71.369	76.122	81.015	85.564	89.931
-13	59.503		66.323	70.680	75.417	80.250	85.273
	55.567		61.574	65.427	69.763	74.487	79.631
-14	51.714		57.015	60.369	64.222	68.610	73.520
	47.838		52.566	55.481	58.852	62.777	67.223
-15	44.033	46.027	48.264	50.787	53.692		60.981
	40.344	42.132	44.110	46.305	48.805		55.018
-16	36.804	38.399	40.140	42.044	44.181		49.389
	33.454	34.828	36.380	38.335	40.381		44.031

TABLE 3
(continued)

x ⟶ / y ↓	10		11		12	13
-17	30317	31548 28506	32859 29623	34254	35753	39134 34715
-18	24796 22369	25709 23143	26650 23932	27621	28625	30749 27212
-19	20159 18174	20811 18723	21469		22782	24069 21318
-20	16381 14753	16844 15142	17297		18151	18903
-21	13287	13611	13919		14473	14902
-22	10798	11015	11210			
-23	8775		9074			
-24	7190		7381			
-25	5911		6066			
-26	4910		5045			
-27	4160		4251			
-28	3541		3627			
-29	3003					
-30	2515					
-31	2020					
-32	1622					
-33	1254					

TABLE 3
(continued)

y ↓ / x →	0		1		2		3		4	
0	100.000	100.053	100.103	100.155	100.186	100.213	100.239	100.271	100.304	100.338
	99.952	100.034	100.090	100.114	100.152	100.174	100.196	100.229	100.265	100.303
+1	99.889	99.933	99.976	100.015	100.053	100.063	100.082	100.123	100.174	100.231
					99.805	99.805	99.806	99.865	99.977	100.063
+2					99.304	99.264	99.223	99.338	99.511	99.729
					98.373	98.216	98.058	98.268	98.642	99.109
+3					96.569	96.232	95.894	96.302	97.022	97.964
								93.140	94.614	96.042
								88.846		93.138
+4										
+5										
+6									72.388	
+7										
+8					59.295	59.370	59.960	60.698	61.736	63.119
							58.569	59.246		61.288
+9			54.324		56.173	56.699	57.181	57.890	58.713	59.708
								56.450	57.280	58.198
+10	47.289		49.857		52.389	53.265	54.035	54.855	55.725	56.677
						51.066		52.964		54.962
+11	41.295		44.295		47.322	48.521	49.622	50.763	51.858	52.981
				42.824		45.730		48.192		50.692
+12	35.180		38.186		41.307	42.703	44.044	45.400	46.727	48.108
				36.690		39.644		42.397		45.227
+13	29.520		32.290		35.194	36.479	37.951	39.318	40.757	42.215
				30.911		33.640		36.320		39.149
+14	24.655		27.021		29.557	30.819	32.093	33.389	34.724	36.102
				25.845		28.198		30.603		33.172
+15	20.565		22.563		24.699	25.775	26.871	28.012	29.163	30.388
				21.576		23.558		25.613		27.796
+16	17.181		18.847		20.610	21.514	22.442	23.399	24.398	25.409
				18.004		19.640		21.367		23.214

TABLE 3
(continued)

x → / y ↓	0		1		2		3		4	
+17	14366	13743	15718	15008	17174	16362	18689	19487 17773	20322 18519	21132 19305
+18	12020		13124		14311		15567	16219	16883	17573
+19	10064		10946		11913		12953	13482	14036	14569
+20	8444		9126		9922	10341	10769	11196	11637	12079
+21	7102		7649	7950	8269	8665	8957	9286	9648	9994
+22			6414		6915		7458	7724	8039	8273
+23			5405		5839		6232	6467	6696	6879
+24	4293		4593		4920		5247	5415	5585	5753
+25					4182	4319	4455	4588	4718	4850
+26							3770	3909	3993	4125
+27							3193	3301	3366	3511
+28							2638	2759	2827	2953
+29							2200	2253	2305	2423
+30										1955
+31										1559
+32									1176	1218

TABLE 3
(continued)

y ↓ / x →	5	6	7	8	9
0	100366 100380 100387 100392 100397 100402 100407				
	100337 100361 100371				
+1	100282 100298 100332 100358 100380				
	100158 100212 100262 100314 100340 100362				
+2	99936 100066 100160 100226 100295 100306 100338 100348				
	99479 99786 99974 100108 100223 100269 100288 100310				
+3	98689 99279 99654 99910 100100 100172 100243 100270 100287				
	97335 98419 99115 99578 99883 100032 100137 100213 100250 100262				
+4	95251 97036 98222 99038 99538 99830 100013 100121 100181 100218				
	92253 94900 96783 97763 98977 99475 99790 99991 100073 100167				
+5	88354 91873 94654 96672 97835 98903 99453 99784 99951 100062				
	83834 87989 91623 94538 96615 97980 98875 99401 99726 99916				
+6	79152 83509 87687 91488 94476 96555 97955 98826 99351 99688				
	74706 78864 83222 87571 91411 94378 96501 97901 98777 99338				
+7	70839 74482 78630 83111 87519 91339 94316 96442 97845 98723				
	67626 70626 74238 78510 83054 87438 91251 94249 96383 97791				
+8	64957 67391 70397 74093 78426 82970 87365 91248 94191 96320				
	62794 64739 67184 70265 74040 78349 82880 87290 91127 94153				
+9	60939 62525 64470 67012 70139 73963 78200 82792 87214 91072				
	59301 60621 62186 64125 66826 70069 73740 78088 82691 87146				
+10	57727 58881 60197 61892 63996 66680 69738 73584 77956 82567				
	56004 57085 58345 59784 61577 63774 66272 69498 73395 77784				
+11	54118 55247 56400 57744 59294 61184 63219 65940 69215 73141				
	51955 53127 54368 55640 57134 58670 60606 62788 65555 68874				
+12	49441 50815 52021 53359 54771 56401 57940 59920 62278 65109				
	46730 48062 49485 50814 52178 53738 55417 57130 59189 61635				
+13	43680 45262 46586 48031 49498 50895 52579 54288 56195 58348				
	40675 42067 43611 45028 46481 48066 49589 51317 53094 55093				
+14	37542 39099 40412 41889 43400 44867 46535 48186 49935 51787				
	34559 35903 37372 38724 40183 41706 43239 44921 46625 48423				
+15	31653 33024 34270 35630 37032 38477 39978 41564 43226 44947				
	28955 30157 31444 32671 33996 35382 36796 38268 39828 41463				
+16	26468 27555 28693 29876 31097 32389 33726 35098 36528 38029				
	24162 25143 36171 27247			29557 30792 31967	34723

TABLE 3
(continued)

x → / y ↓	5		6		7		8		9	
+17	22057 20105	22902 20916	23844	24812	25830	26887	28024	29136	30294	31546
+18	18312	19015	19795	20563	21364	22209	23104		24900	
+19	15169	15729	16378	16984	17612	18275	18997		20346	
+20	12518	13018	13493	13995	14505	15017	15551		16581	
+21	10369	10731	11098		11910	12296	12706		13488	
+22	8572	8868	9155		9780	10061	10388		10963	
+23	7100	7350	7545		8039	8261	8493		8939	
+24	5925	6112	6285	6463	6638	6805	6977		7310	
+25	4976	5139	5249		5517	5645	5796		6018	
+26	4200	4354	4429		4620	4756	4844		5043	
+27	3564	3683	3767		3934	4042	4112		4255	
+28	3001	3116	3186		3324	3427	3494		3626	
+29	2481	2566	2651		2800	2878	2938		3071	
+30	2004	2096	2156		2299	2372	2429		2571	
+31	1595	1648	1721	1788	1854	1910	1978		2090	
+32	1256	1301	1355	1408	1464	1516	1557		1651	

TABLE 3
(continued)

x → / y ↓	5		6	7		8	9
+33	0.987	1.017	1.057	1.171	1.181	1.204	1.308
+34	0.755		0825	0.897	0.905	0.936	1.022
+35		0.653	0.668	0.691	0.720	0.732	0.791
+36					0.561	0.565	

TABLE 3
(continued)

x → / y ↓ 0	10	11	12	13
+1				
+2				
+3				
+4	100233	100231		
	100191	100197		
+5	100116	100012	100157	
	100011	100083	100108	
+6	99871	99968	100033	100064
	99648	99816	99921	99984
+7	99283	99592	99759	99877	99929	
	98670	99229	99533	99716	99826	
+8	97736	98621	99170	99480	99668	99768	99792
	96276	97675	98576	99119	99437		99680
+9	94103	96200	97611	98516	99055		99510
	91001	93999	96119	97557	98440	98960	99233
+10	87053	90885	93882	96060	97484	98339	98841
	82414	86900	90752	93799	95979	97365	98217
+11	77572	82225	86717	90638	93691	95835	97210
	72833	77318	81996	86545	90485	93512	95641
+12	68465	72482	77004	81741	86321	90242	93277
	64536	67994	72052	76631	81407	85988	89925
+13	60867	63883	67406	71537	76139	80940	85566
	57354	59979	63050	66667	70861	75463	80357
+14	53848	56204	58921	62065	65724	69934	74625
	50353	52492	54908	57665	60843	64504	68786
+15	46784	48769	50958	53385	56151	59329	63032
	43186	45033	47030	49211	51615		57468
+16	39617	41309	43123	45066	47190		52139
		37685	39306	41021	42853		46976

TABLE 3
(continued)

x / y	10		11		12	13
+17	32861	34220	35641 32178	37135	38706 34779	42105 37542
+18	26883		28962 25996		31143 27821	33349 29539
+19	21821		23312 20872		24780 22071	26123 23095
+20	17657		18685 16708		19661	20436
+21	14235		14951 13378		15573	16008
+22	11533		11987 10741		12387	
+23	9350		9663		9898	
+24	7592		7812		7977	
+25	6222		6386			
+26	5167		5274			
+27	4348		4424			
+28	3707		3764			
+29	3165		3232			
+30	2665					
+31	2187					
+32	1751					
+33	1363					

Field values are shown as percentages relative to the value at the converter position (x = 0, y = 0) taken to be 100.00 %. The position coordinates are indicated on Figures 27, 30, 31, and 32.

TABLE 4

Central Orbit Calculation Example

No. of Step	x	y	g	"G	'G	G	Δ^1	Δ^2	....	$\frac{H(x,y)}{Ho}$
	-1.0	.07047	.14163	-.26988		-.14439				.99899
					.21141		.00313			
	- .5	-.01754	.07030	-.05847		-.14126		-.00217		.99948
					.07015		.00096		.00010	
0	0	0	0	.01168		-.14030		-.00207		1.00000
1/2					-.07015		.00111		.00011	
1	+ .5	+.01756	.07034	-.05847		-.14141		-.00218		1.00054
1 1/2					-.21156		-.00329		-.00024	
2	1.0	.07052	.14177	.27003		-.14470		-.00242		1.00104
2 1/2					-.35626		-.00571		-.00046	
3	1.5	.15971	.21544	.62629		-.15041		-.00288		1.00156
3 1/2					-.50667		-.00859			
4	2.0	.28655	.29266	1.13296		-.15900				

--- Dotted line indicates division between values which are fixed and those which are guessed.

Constants Used In this Orbit.

E = 49.51096 Mev; H_o = 9.12261 kilo gauss; R_o = 7.12777 inches.

Formulas used: $G_3 = \pm \frac{1}{R_o}\left(\frac{H(x_3,y_3)}{H_o}\right)\left[1 + g_2\right]^{3/2}$ $\quad {}^1G_{3\ 1/2} = {}^1G_{2\ 1/2} + G_3, \Delta^1{}_{2\ 1/2} = G_3 - G_2$ etc.

$${}^{"}G_4 = {}^{"}G_3 + {}^{'}G_{3\ 1/2},\ \Delta^2_3 = \Delta'_{3\ 1/2} - \Delta'_{2\ 1/2} \quad \text{etc.} \quad [\text{Eq. 61 in text}]$$

TABLE 4 (continued)

Results For Orbits

	Positive Side				Negative Side			
T	x	y	l	ϕ(rad)	x	y	l	ϕ
49	1.4803	17.9404	5.2545	1.0348	1.5030	-18.0228	5.3399	1.0296
57	2.3521	21.1028	8.5348	.9278				
65	3.2787	24.4640	12.0214	.8243	3.3319	-24.6569	12.2215	.8065
81	5.3637	32.0271	19.8667	.66395	5.4587	-32.3717	20.2241	.64665

T Kinetic energy of the electron.

x,y Coordinates of the intersection of the orbit with the focus line.

l Coordinate as measured along the focus line; The origin was placed at an arbritrary point.

ϕ Acute angle of the intersection of the orbit with the focus line.

The polynomials for the energy scale derived from these orbits are:

Positive side

$$E = 35.783468 + 2.715793\,\bar{z} - 0.019234\bar{z}^2 + 0.000081\bar{z}^3$$

Negative side

$$E = 35.667337 + 2.709313\bar{z} - 0.021882\bar{z}^2$$

TABLE 5

THE TUBE LOCATIONS

(Explanation of symbols will be found at the end of the table)

Positive A (Top Row)

N	x	x	u	ℓ'	ℓ	E	δE	ϕ
5	6.733	31.329	1.505	19.558	21.550	84.5651	0.0651	0.6481
7	6.310	29.852	1.491	18.022	19.936	81.6386	0.1386	0.6632
9	5.901	28.434	1.473	16.545	18.357	78.6541	0.1541	0.6846
11	5.542	27.065	1.491	15.130	16.874	75.7437	0.2437	0.7102
13	5.162	25.755	1.473	13.766	15.389	72.7263	0.2263	0.7406
15	4.849	24.456	1.516	12.431	13.999	69.8102	0.3102	0.7729
17	4.477	23.195	1.493	11.117	12.553	66.6834	0.1834	0.8100
19	4.160	21.997	1.505	9.877	11.226	63.7324	0.2324	0.8468
21	3.839	20.811	1.511	8.649	9.904	60.7153	0.2153	0.8857
23	3.500	19.651	1.492	7.441	8.587	57.6343	0.1343	0.9263
25	3.196	18.528	1.497	6.277	7.341	54.6515	0.1515	0.9660
27	2.889	17.418	1.497	5.125	6.107	51.6330	0.1330	1.0065
29	2.590	16.324	1.500	3.991	4.899	48.6170	0.1170	1.0468
31	2.295	15.266	1.497	2.892	3.730	45.6415	0.1415	1.0862

$\overline{\delta E}$ = + 0.1747

Positive B (Bottom Row)

N	x	y	u	ℓ'	ℓ	E	δE	ϕ
4	6.319	33.727	0.469	21.759	22.385	86.0295	0.0295	0.6432
6	5.903	32.178	0.480	20.155	20.781	83.1869	0.1869	0.6543
8	5.482	30.692	0.469	18.611	19.201	80.2646	0.2646	0.6723
10	5.056	29.215	0.453	17.075	17.616	77.2129	0.2129	0.6967
12	4.661	27.796	0.447	15.601	16.106	74.1958	0.1958	0.7253
14	4.313	26.429	0.475	14.190	14.695	71.2814	0.2814	0.7563
16	3.957	25.093	0.487	12.808	13.291	68.2910	0.2910	0.7907
18	3.592	23.793	0.480	11.458	11.901	65.2432	0.2432	0.8278
20	3.246	22.523	0.484	10.141	10.555	62.2105	0.2105	0.8662
22	2.804	21.306	0.481	8.851	9.231	59.1501	0.1501	0.9061
24	2.553	20.063	0.471	7.586	7.928	56.0648	0.0648	0.9470
26	2.243	18.880	0.486	6.363	6.687	53.0597	0.0597	0.9872
28	1.932	17.715	0.496	5.158	5.461	50.0276	0.0276	1.0278
30	1.601	16.574	0.479	3.969	4.236	46.9362	-0.0638	1.0689
32	1.297	15.410	0.496	2.766	3.018	43.8023	-0.1977	1.1101

$\overline{\delta E}$ = +0.1304

TABLE 5 (continued)

Positive C (Top Row)

N	x	y	u	ℓ'	ℓ	E	δE	ϕ
4	5.755	35.422	-0.525	23.243	22.542	86.3021	0.3605	0.6425
6	5.318	33.783	-0.511	21.547	20.880	83.3663	0.3663	0.6534
8	4.883	32.235	-0.519	19.939	19.287	80.4270	0.4270	0.6712
10	4.479	30.710	-0.503	18.362	17.757	77.4896	0.4896	0.6943
12	4.070	29.224	-0.503	16.821	16.251	74.4906	0.4906	0.7222
14	3.671	27.785	-0.504	15.327	14.792	71.4849	0.4849	0.7539
16	3.274	26.381	-0.514	13.869	13.360	68.4402	0.4402	0.7887
18	2.915	25.008	-0.496	12.449	11.993	65.4478	0.4478	0.8250
20	2.551	23.660	-0.488	11.053	10.638	62.3999	0.3999	0.8636
22	2.178	22.362	-0.503	9.702	9.308	59.3303	0.3303	0.9037
24	1.823	21.069	-0.501	8.362	8.003	56.2445	0.2445	0.9446
26	1.496	19.814	-0.482	7.065	6.748	52.2090	0.2090	0.9852
28	1.142	18.587	-0.498	5.787	5.490	50.1000	0.1000	1.0269
30	0.829	17.394	-0.483	4.555	4.293	57.0815	0.815	1.0670
32	0.495	16.208	-0.490	3.322	3.083	43.9711	-0.289	1.1079

$\overline{\delta E}$ = +0.3229

Positive D (Bottom Row)

N	x	y	u	ℓ'	ℓ	E	δE	ϕ
5	4.911	36.224	-1.559	23.793	21.731	84.8860	0.3860	0.6468
7	4.470	34.572	-1.538	22.082	20.108	81.9575	0.4575	0.6611
9	4.037	33.027	-1.545	20.418	18.521	78.9695	0.4695	0.6819
11	3.577	31.390	-1.554	18.777	16.970	75.9356	0.4356	0.7081
13	3.183	29.849	-1.523	17.187	15.520	72.9967	0.4967	0.7374
15	2.738	28.340	-1.551	15.614	14.031	69.8793	0.3793	0.7717
17	2.348	26.882	-1.540	14.105	12.643	66.8825	0.3825	0.8071
19	1.964	25.463	-1.533	12.635	11.288	63.8730	0.3730	0.8446
21	1.565	23.997	-1.528	11.115	9.884	60.6694	0.1694	0.8858
23	1.202	22.690	-1.531	9.759	8.624	57.7229	0.2229	0.9247
25	0.847	21.351	-1.517	8.374	7.348	54.6692	0.1692	0.9655
27	0.475	20.031	-1.525	7.002	6.067	51.5335	0.0335	1.0075
29	0.121	18.746	-1.515	5.670	4.831	48.4464	-0.0536	1.0488
31	-0.213	17.482	-1.511	4.362	3.613	45.3401	-0.1599	1.0899

$\overline{\delta E}$ = +0.2687

TABLE 5 (continued)

Negative A (Top Row)

N	x	y	u	ℓ'	ℓ	E	δE	ϕ
40	2.288	-15.272	-1.490	2.896	3.709	45.4151	-0.0849	1.0943
42	2.603	-16.342	-1.499	4.011	4.922	48.4727	-0.0273	1.0459
44	2.881	-17.430	-1.486	5.134	6.120	51.4291	-0.0709	1.0005
46	3.193	-18.539	-1.485	6.289	7.366	54.4366	-0.0634	0.9559
48	3.536	-19.686	-1.517	7.483	8.682	57.5406	+0.0406	0.9116
50	3.843	-20.835	-1.507	8.672	9.960	60.4815	-0.0185	0.8713
52	4.210	-22.029	-1.492	9.921	11.348	63.5943	-0.0943	0.8307
54	4.487	-23.218	-1.495	11.141	12.619	66.3719	-0.1281	0.7962
56	4.859	-24.472	-1.519	12.448	14.057	69.4283	-0.0713	0.7606
58	5.201	-25.766	-1.505	13.787	15.485	72.3740	-0.1260	0.7286
60	5.540	-27.018	-1.500	15.174	16.872	75.3392	-0.1608	0.7008
62	5.972	-28.442	-1.487	16.572	18.445	78.1959	-0.3041	0.6731
64	6.330	-29.872	-1.501	18.045	20.027	81.1500	-0.3496	0.6495
66	6.740	-31.362	-1.502	19.591	21.658	84.0811	-0.4189	0.6295

$\overline{\delta E}$ = -0.1206

Negative B (Bottom Row)

N	x	y	u	ℓ'	ℓ	E	δE	ϕ
39	1.315	-15.508	-0.487	2.865	3.106	43.8719	-0.1281	1.1191
41	1.644	-16.628	-0.506	4.032	4.314	46.9469	-0.0531	1.0697
43	1.940	-17.781	-0.485	5.223	5.523	49.9626	-0.0374	1.0227
45	2.287	-18.959	-0.505	6.450	6.796	53.0682	+0.0682	0.9758
47	2.608	-20.134	-0.502	7.668	8.043	56.0435	-0.0435	0.9325
49	2.939	-21.346	-0.501	8.925	9.333	59.0465	-0.0465	0.8905
51	3.270	-22.577	-0.494	10.200	10.632	61.9998	-0.0002	0.8510
53	3.638	-23.846	-0.509	11.521	12.005	65.0385	+0.0385	0.8123
55	3.993	-25.139	-0.508	12.862	13.380	68.0014	+0.0014	0.7767
57	4.350	-26.487	-0.495	14.256	14.796	70.9636	-0.0364	0.7434
59	4.723	-27.862	-0.488	15.681	16.247	73.9095	-0.0905	0.7127
61	5.119	-29.263	-0.498	17.137	17.748	76.8594	-0.1406	0.6847
63	5.534	-30.730	-0.507	18.661	19.316	79.8357	-0.1643	0.6595
65	5.951	-32.235	-0.510	20.223	20.911	82.7540	-0.2460	0.6380
67	6.399	-33.812	-0.522	21.862	22.594	85.7101	-0.2899	0.6200

$\overline{\delta E}$ = -0.0659

TABLE 5 (continued)

Negative C (Top Row)

N	x	y	u	ℓ'	ℓ	E	δE	ϕ
39	0.484	-16.216	0.501	3.327	3.089	43.8279	-0.1721	1.1198
41	0.832	-17.408	0.485	4.568	4.307	46.9299	-0.0701	1.0700
43	1.150	-18.613	0.497	5.815	5.515	49.9432	-0.0568	1.0229
45	1.486	-19.850	0.502	7.097	6.761	52.9852	-0.0148	0.9770
47	1.826	-21.111	0.510	8.403	8.028	56.0062	+0.0062	0.9330
49	2.174	-22.392	0.516	9.730	9.314	59.0035	+0.0035	0.8911
51	2.542	-23.696	0.506	11.085	10.643	62.0238	+0.0238	0.8506
53	2.902	-25.030	0.516	12.472	11.986	64.9975	-0.0025	0.8128
55	3.291	-26.409	0.507	13.899	13.384	68.0094	+0.0094	0.7766
57	3.676	-27.818	0.511	15.360	14.805	70.9826	-0.0174	0.7429
59	4.087	-29.255	0.495	16.855	16.282	73.9795	-0.0205	0.7120
61	4.486	-30.726	0.503	18.379	17.763	76.8893	-0.1107	0.6844
63	4.910	-32.256	0.498	19.967	19.325	79.8527	-0.1473	0.6593
65	5.329	-33.806	0.508	21.572	20.888	82.7120	-0.2880	0.6383
67	5.785	-35.450	0.506	23.278	22.570	85.6701	-0.3299	0.6203

$\overline{\delta E}$ = -0.0791

Negative D (Bottom Row)

N	x	y	u	ℓ'	ℓ	E	δE	ϕ
40	0.171	-17.532	1.484	4.422	3.694	45.3762	-0.1238	1.0945
42	0.175	-18.805	1.490	5.741	4.910	48.4428	-0.0572	1.0460
44	0.520	-20.096	1.499	7.077	6.141	51.4793	-0.0207	0.9993
46	0.881	-21.407	1.499	8.437	7.399	54.5146	+0.0146	0.9543
48	1.261	-22.749	1.491	9.831	8.694	57.5683	+0.0683	0.9107
50	1.613	-24.056	1.497	11.186	9.944	60.4441	-0.0559	0.8713
52	2.020	-25.512	1.491	12.697	11.349	63.5968	+0.0968	0.8302
54	2.436	-26.939	1.471	14.183	12.746	66.6451	+0.1451	0.7925
56	2.845	-28.405	1.466	15.705	14.166	69.6569	+0.1569	0.7576
58	3.230	-29.910	1.497	17.258	15.582	72.5708	+0.0708	0.7262
60	3.639	-31.453	1.511	18.855	17.059	75.5169	+0.0169	0.6970
62	4.085	-33.028	1.500	20.492	18.599	78.4863	+0.0020	0.6684
64	4.531	-34.630	1.495	22.155	20.182	81.4342	-0.0658	0.6472
66	4.991	-36.268	1.486	23.856	21.812	84.3519	-0.1474	0.6278

$\overline{\delta E}$ = +0.0072

TABLE 5 (continued)

EXPLANATION OF SYMBOLS

N — Channel number is chosen so that the equal energy channels correspond to a constant difference between the electron and positron channel numbers.

x,y — Coordinates of the tube relative to the precision template.

u — Coordinate perpendicular to the focus line.

ϕ — Angle of intersection of the orbit and the focus line obtained by expressing ϕ as polynomial in ℓ which is constructed to fit the results of the precise orbit calculations.

ℓ — Coordinate of orbit which passes through the center of the tube as measured along the focus line.

$$\ell = \ell' + u \cot\phi - \frac{u^2}{R_c} \sec^3 \phi$$

R_c is the average curvature of the orbit.

ℓ' — Projected coordinate as measured along the focus line.

E — Channel energy, obtained by expressing E as a polynomial in ℓ which is constructed to fit the result of the precise orbit calculations.

δ E — The difference between the assigned channel energy and the calculated energy which resulted from the errors of the locating procedure.

The Code for the Tubes

There are two sides, positive and negative as indicated throughout the calculations. Each side has four rows, A,B,C,D. Two are on the bottom of the geiger tube holder, two on top. The letters are assigned to match the rows in the order in which a particle passes through the array.

TABLE 6

DIFFERENTIAL ANALYZER RESULTS

A Homogenous solutions of ρ and Z equations
$\rho(0)$, $\rho'(0)$, $Z(0)$, $Z'(0)$ are initial conditions
$\rho(S_f)$, $\rho'(S_f)$, $Z(S_f)$, $Z'(S_f)$ are terminal values
as measured at the focus line.

Negative side — Final displacement and slope for various energies

Initial condition	49 Mev	65 Mev	81 Mev
$\rho = 0 \quad \rho' = \theta_M$	$\rho = 0 \quad \rho' = -0.0615$	$\rho = -0.026 \quad \rho' = -0.0435$	$\rho = +0.0245 \quad \rho' = -0.0327$
$\rho = 1 \quad \rho' = 0$	$\rho = -1.630 \quad \rho' = -0.127$	$\rho = -1.665 \quad \rho' = -0.0992$	$\rho = -1.683 \quad \rho' = -0.0840$
$Z = 0 \quad Z' = \theta_M$	$Z = +3.125 \quad Z' = +0.144$	$Z = +3.212 \quad Z' = +0.125$	$Z = +3.360 \quad Z' = +0.044$
$Z = 1 \quad Z' = 0$	$Z = +1.810 \quad Z' = +0.0522$	$Z = +1.860 \quad Z' = +0.0486$	$Z = +1.913 \quad Z' = +0.0163$

Positive Side (check on symmetry of magnet)

$\rho = 0 \quad \rho' = \theta_M$	$\rho = +0.024 \quad \rho' = -0.0442$
$\rho = 1 \quad \rho' = 0$	$\rho = -1.651 \quad \rho' = -0.0974$
$Z = 0 \quad Z' = \theta_M$	$Z = +3.189 \quad Z' = +0.1250$
$Z = 1 \quad Z' = 0$	$Z = +1.795 \quad Z' = +0.0458$

TABLE 6
(continued)

B Second order results
The cases correspond to the solution of the ρ equation with higher order terms as explained in text.

Case	Initial Conditions ρ	ρ'	Z	Z'	Final Displacement $\rho(S_f)49$	$\rho(S_f)65$	$\rho(S_f)81$
1	1	0	0	0	-0.0011	-0.0039	+0.0013
2	0	θ_M	0	0	-0.0786	-0.0496	-0.0264
3	1	θ_M	0	0	-0.0734	-0.0447	
4	-1	θ_M	0	0	-0.0689	-0.0545	
5	0	0	1	0	-0.1293	-0.1232	
6	0	0	0	θ_M	-0.3355	-0.2369	
7	0	0	1	θ_M	-0.8117	-0.6235	
8	0	0	-1	θ_M	-0.1244	-0.0835	
9	0	0	1	$\theta_M/2$	-0.3939	-0.2515	
10	0	0	-1	$\theta_M/2$	-0.0463	-0.0396	
11	1	θ_M	1	θ_M	-0.7122	-0.6570	
12	-1	θ_M	1	θ_M	-0.7058	-0.6915	
13	1	θ_M	-1	θ_M	-0.1802	-0.1300	
14	-1	θ_M	-1	θ_M	-0.1646	-0.1383	

C The values of θ_M are chosen to be the R.M.S. scattering angle for the pair of particles passing through the converter a thickness of approximately one-half the total thickness. The value is obtained by weighting the various thicknesses by the relative detection efficiency.

Kinetic energy	49 Mev	65 Mev	81 Mev
θ_M =	0.100	0.750	0.600

TABLE 7

SHIFTS IN THE ENERGY SCALE

A. Resolution

1. Ionization energy loss

Converter $\delta E^I = \Sigma w_i' \Delta E_i^I =$ −0.526 Mev

Air $\delta E =$ -0.174 Mev

weighting factors due to scattering out

t	0.10	0.30	0.50	0.70	0.90
w_i	0.2834	0.2250	0.1893	0.1614	0.1410

$$\bar{t} \doteq \frac{\Sigma w_i t_i}{\Sigma w_i} \doteq 0.431 \text{ (for continuous spectra)}$$

2. Radiation energy loss (cut off at + 6 Mev)

$$\delta E^R = \Sigma w_i' \Delta E_i^R = \quad -0.381 \text{ Mev}$$

Areas under straggling curve

t_i	0.10	0.30	0.50	0.70	0.90
A_i	0.967	0.905	0.841	0.787	0.736
w_i'	0.3155	0.2344	0.1843	0.1462	0.1195

$$\bar{t} = \frac{\Sigma w_i A_i t_i}{\Sigma w_i A_i} = \Sigma w_i' t_i = \quad 0.404$$

3. Horizontal scattering ρ'

first order theory (1S)

$$\delta E^{1S} = \quad +0.003 \text{ Mev}$$

second order theory (2S)

$$\delta E^{2S} = \quad -0.153 \text{ Mev}$$

4. Horizontal width

first order theory (1L)

$$\delta E^{1L} = \quad +0.709 \text{ Mev}$$

TABLE 7
(continued)

second order theory (2L)

δE^{2L} = -0.002 Mev

5. Channel location shift (Table 5)

δE^{C} = -0.146 Mev

6. Vertical scattering and height (See note - Table 10)

second order theory

δE^{2V} = -0.603 Mev

7. Net moment of resolution (See note at end of Table 7)

δE = -1.283 Mev

B. Effect of weighting of various energy channels due to statistical factor. (See Table 8)

δE = 0.019 Mev

C. Background subtraction; estimate of change in moment for various normalization of data

1. Change if normalizing factor is varied ± 10 percent

δE = ±0.05 Mev

2. Change if spectrum is not cut off at ± 6 Mev

δE = +0.256 Mev

D. Discrepancy of fit by moment and fit by eye

δE = -0.087 ± 0.045 Mev

TABLE 7
(continued)

The net first moment of the resolution which is obtained from the fold of two or more components can be obtained by simply adding algebraically the first moments of the components.

To prove this let us define

$$R(x) = \int f(x-t)\ g(t)\ dt \tag{1}$$

The first moment of the resolution is defined to be

$$\overline{x} = \frac{\int x\ R(x)\ dx}{\int R(x)\ dx} \tag{2}$$

This can be rewritten as follows

$$\int \left[x - \overline{x}\right]\ R(x)\ dx = 0 \tag{3}$$

Let us define the first moments of the components to be F and G in a similar manner.

$$\int \left[\xi - F\right]\ f(\xi)\ d\xi = 0 \tag{4}$$

$$\int \left[t - G\right]\ g(t)\ dt = 0 \tag{5}$$

We can restate the Theorem

$$\overline{x} = G + F \tag{6}$$

by the equation

$$\int \left[x - G - F\right]\ R(x)\ dx \stackrel{?}{=} 0 \tag{7}$$

or

$$\iint \left[x - G - F\right]\ f(x-t)\ g(t)\ dt\ dx \stackrel{?}{=} 0 \tag{8}$$

TABLE 7
(continued)

If this integral vanishes our Theorem holds.

From Equation 5 we can form the integral

$$\int f(\xi) \int \left[t-G\right] g(t)\, dt\, d\xi = 0 \qquad (9)$$

Since f and g are well behaved we have that

$$\iint \left[t - G\right] f(\xi)\, g(t)\, dt\, d\xi = 0 \qquad (10)$$

Similarly from Equation 4

$$\iint \left[\xi - F\right]\, g(t)\, f(\xi)\, d\xi\, dt = 0 \qquad (11)$$

If we add Equations 10 and 11

$$\iint \left[t + \xi - G - F\right] f(\xi)\, g(t)\, d\xi\, dt = 0 \qquad (12)$$

Transforming to the variables

$$\begin{aligned} t &\longrightarrow t \\ x &\longrightarrow \xi + t \\ x - t &= \xi \end{aligned} \qquad (12)$$

$$d\xi\, dt = dx\, dt$$

Thus Equation 12 becomes

$$\iint \left[x - G - F\right] f(x - t)\, g(t)\, dx\, dt = 0 \qquad (13)$$

This is Equation 8 and our Theorem is proved.

TABLE 8

Channel	Energy	H_2 Counts	Normalized Background	Correction Factor	Corrected Intensity	Probable Error
28	119.50	17	17.9	1.204	- 1.08	4.04
		17	17.8	1.183	- 0.95	3.94
29	121.00	16	17.6	1.167	- 1.87	3.61
		23	17.4	1.147	6.42	4.20
30	122.50	13	17.2	1.133	- 4.76	3.29
		17	16.8	1.118	0.22	3.66
31	124.00	21	16.5	1.104	4.97	3.88
		27	16.1	1.086	11.84	4.14
32	125.50	23	15.7	1.073	7.83	3.94
		33	15.2	1.059	18.85	4.45
33	127.00	63	14.8	1.046	50.42	5.87
		100	14.2	1.033	88.63	7.18
34	128.50	137	13.7	1.021	125.88	8.27
		96	13.1	1.009	83.65	6.88
35	130.00	49	12.5	1.000	36.50	4.99
		24	11.9	1.021	12.35	3.63
36	131.50	21	11.3	1.046	10.15	3.52
		18	10.6	1.069	7.91	3.36
37	132.00	13	10.0	1.096	3.29	2.93
		13	9.2	1.122	4.26	3.05
38	133.50	10	8.6	1.149	1.61	2.81
		11	8.0	1.181	3.54	3.05
39	134.00	10	7.4	1.210	3.15	2.97
		2	6.8	1.240	- 5.95	1.81
40	135.50	9	6.3	1.272	3.43	2.99

TABLE 9

Mass Calculation

Relation between energy of gamma ray and masses:

$$E_\gamma = M_\pi c^2 - \frac{E_\gamma^2}{2M_N c^2} + \frac{1}{8}\left(\frac{E_\gamma^4}{(M_N c^2)^3}\right) - \frac{\alpha^2}{2} - (M_N - M_P)c^2 + \cdots$$

The electronic rest mass, DuMond and Cohen:[59]

$$Mc^2 = 0.510969 \pm 2/10^5 \text{ Mev}$$

The N-P mass difference, Robson:[60]

$$(M_N - M_p)\, c^2 = 1.293(\pm 0.013) \text{ Mev}$$

The magnetic moment of the proton as obtained by Thomas Driscoll and Hipple:[61]

$$g_P = 2.67530\ (\pm 0.0006) \times 10^4 \text{ Sec}^{-1} \text{ gauss}^{-1}$$

The resulting conversion factor from frequency to field:

$$H = 234.865\ (\pm 0.005)\ \gamma \text{ (Megacycles) gauss}$$

The field measured at the converter position (x = 0 y = 0)

$$H_0 = 9.12261 \text{ Kilo gauss}$$

The radius of curvature at the converter

$$R_0 = \frac{E}{Hc}\left[1 + \frac{1}{2}\left(\frac{Mc^2}{E}\right)^2 + \cdots\right]$$

The velocity of light.

$$c = 2.99790 \times 10^{10} \text{ cm/sec}$$

To convert to the energy scale at the detector the results of Table 4 were used

The resolution has a first moment about the assumed zero of

$$-1.283 \quad \text{Mev.}$$

The calculated moment of the data is

$$128.303 \quad \text{Mev.}$$

The moment as observed to be in good agreement with the resolving power is.

$$128.214 \text{ Mev}$$

From these values one can evaluate the energy of the gamma ray.

$$E_\gamma = 129.54 \pm 0.23 \text{ Mev}$$

With this value of E_γ the mass can be obtained to be

$$273.5 \pm 0.5 \text{ m}$$

TABLE 10

SUMMARY OF ERRORS IN MASS MEASUREMENTS

A. Statistical error, based on equivalent gaussian distribution analysis: (RMS)

$$\Delta E = \sqrt{\frac{\Sigma n_i \Delta E_i^2}{(\Sigma n_i)(\Sigma n_i - 1)}} \doteq \frac{\sigma}{\sqrt{N}} = \frac{1.0 \text{ Mev}}{\sqrt{416}} = 0.048 \text{ Mev}$$

$$3.7/10^4$$

B. Uncertainty in central field monitoring based on estimates of deviations observed, which were corrected periodically during the measurements of the Gamma Ray spectrum. Error assigned is 1/2 the maximum deviation:

$$1.0/10^4$$

C. Weighted errors in field measurements obtained in Table 2:

$$3.5/10^4$$

D. Errors in Geometry--counter location templates, etc., based on a series of cross checks and measurements before and after cyclotron runs:

$$3.5/10^4$$

E. Error of energy scale computations apart from uncertainties due to field. Includes error introduced by having only seven orbits:

$$1/10^4$$

F. Errors of computations for the second order skew effects includes uncertainties of higher derivatives obtained from field data and estimated uncertainties in target illumination:

$$6/10^4$$

G. Errors arising from first order resolving power includes estimated errors in ionization loss:

$$2/10^4$$

H. Total error calculated by combining squares of estimated electron masses:

$$\pm 0.28 \text{ electron masses}$$

TABLE 10
(continued)

I. Additional probable errors, which are included by the experimenter to take into account many corrections which have been estimated to be smaller than those considered,* but which until the detailed calculations are completed may combine in a systematic rather than random manner (also included here is as estimate of the error in the fit of the theoretical resolution to the data):

$$\pm 14/10^4 \quad \text{or} \quad \pm 0.40 \text{ electron masses}$$

J. Total obtained by combining squares:

$$\pm 0.50 \text{ electron masses}$$

Finally, since the method of estimating errors is to some extent one which is based on the usual conventions rather than detailed analysis of the error theory, the possibility exists that one or more estimated probable errors may be incorrect as much as a factor of two is possible.

* The major source of this error is that caused by the approximations involved in the calculation of the vertical motion perturbation correction in the energy scale. In particular the calculation of the two particle model which is discussed in Section V-D is not completed at the present time and an estimate of the result has been applied but the error of this estimate is not included elsewhere. On the completion of this calculation, the size of the errors of this Type (I) will be reduced considerably.

X. FIGURE CAPTIONS

Fig. 1 Typical cloud chamber arrangement for cosmic ray meson mass measurements. The top chamber measures momentum and the lower chamber determines ranges. An alternative position of the deflecting field is at D.

Fig. 2 Cosmic ray meson mass data obtained by Retallic and Brode. The short lines represent individual points with their associated uncertainties.

Fig. 3 Target arrangement for negative meson mass measurement.

Fig. 4 Diagram illustrating geometry of experiments to measure meson to proton mass ratios.

Fig. 5 Range histogram of μ^+ mesons from decay of π^+ mesons at rest in nuclear emulsions.

Fig. 6 The π^+ energy spectrum from 340 Mev protons on hydrogen.

Fig. 7 The physical arrangement of apparatus used to study the reaction $P + P \rightarrow \pi^+ + D$.

Fig. 8 The detailed spectrum from the reaction $P + P \rightarrow \pi^+ + D$ measured at 0^o. This peak was used to measure the π^+ mass.

Fig. 9 The π^- capture γ-ray energy spectrum measured with poor resolution. Resolving powers ~22.5 percent width at half maximum.

Fig. 10 The photon spectrum associated with cosmic ray stars. The circles are the values of $Mc^2/2$ obtained for various energy π^o's.

Fig. 11 The neutral meson decay gamma ray spectrum averaged over all laboratory angles obtained with 340 Mev protons on carbon. The dotted curves are drawn for various π^o masses assuming no other sources of γ-rays.

Fig. 12 Composite plot of γ-ray spectrum resulting from the capture of negative pions in hydrogen. Note that the scale is expanded by a factor of five below $I_\gamma = 75$ to show details of π^o peak.

Fig. 13 Experimental arrangement used in early π^- capture experiments.

Fig. 14 Outline diagram of pair spectrometer used in early π^- capture experiments.

Fig. 15 The gamma ray energy spectrum with the theoretical resolving power used in previous π^- mass measurements. The resolution does not include ionization loss, horizontal width corrections, and energy scale corrections due to fringe field. Probable errors are shown.

Fig. 16 Channel width resolution of the early measurements. $\Delta E = E_o - E$ where E_o is the total energy of the gamma ray and E is the observed energy.

Fig. 17 Scattering resolution of the early measurements. Multiple scattering of pair fragments in the converter widens the measured energy distribution.

Fig. 18 Radiation resolution of the early measurements. Radiation of pair fragments which leave the converter lowers the apparent energy.

Fig. 19 The total resolving power which was used in previous γ-ray spectrum analysis. The ionization loss was not included. The changes in the energy scale due to the second order aberations and corrections due to fringe fields were applied as changes in the meson mass.

Fig. 20 Wedge focusing for the small angle scattering in the horizontal plane at the converter. The shaded region indicates a uniform magnetic field.

Fig. 21 The finite converter width aberration simplified for the uniform field case. First order cancellation is obtained since the sum of the electron and positron energy is measured.

Fig. 22 The qualitative effect of the fringe field on the horizontal scattering focus is to distort the focal line for different particle energies.

Fig. 23 The general layout of the experimental apparatus.

Fig. 24 Internal hydrogen target assembly. The vessel walls are stainless steel.

Fig. 25 Collimation system. The scale is chosen to show limiting rays arising from horizontal and vertical widths. The vertical limiting rays are shown from the center and edge of the source. All of the horizontal limiting rays extend beyond the edge of the converter.

Fig. 26 Microphotometer trace of intensified x-ray film which has been exposed to 90 Mev neutrons passing through the collimating system. The vertical profile indicates that the beam probably came from a point on the source below the center line of the collimation. The slope of the horizontal profile is due to non uniform development. The converter is indicated by dotted lines.

Fig. 27 Top view of counter holder in relation to magnet pole tip. The orbits for 49 and 81 Mev electrons are shown. The overlap channels defined by coincidences between adjacent geiger tubes are shown for the central energy of the spectrometer. The duplicate numbered sets of tubes correspond to the top and bottom rows as is shown in Fig. 28

Fig. 28 The side view (cross section) of the tube holder, magnet pole tip and multi wire proportional counter. The geiger counters straddle the focus line.

Fig. 29 The electronic block diagram.

Fig. 30 The field contours on one side of the magnet.

Fig. 31 The grid of field measurements positron side. ϵ's indicate the range of errors in percent of H_o which are estimated to be associated with each of the regions in the field.

Fig. 32 Same as Fig. 31, electron side.

Fig. 33 The weighting function for errors in the magnetic field measurements plotted against the arc length of the orbits for the various energies. Both types of errors are weighted differently depending upon the point where they occur in the orbit.

Fig. 34 The input functions for A(s), the restoring term in the horizontal motion. The curves are plotted for the various energies considered.

Fig. 35 The input functions B(s) for the vertical motion.

Fig. 36 The family of ρ solutions for the horizontal motion. ρ' is approximately the mean square angle of scattering.

Fig. 37 The family of Z solutions which determines the vertical motion in the first order theory.

Fig. 38 The finite detector channel width resolution. The dotted curve is the ideal resolution for a single pair of counters located at positions such that $E^+ + E^- = E_o$. The solid curve is the actual resolution when averaged over slight errors in location and in channel widths.

Fig. 39 The gamma ray energy distribution in the first order resolution theory which results from multiple scattering in the converter in the horizontal plane only. This distribution results from the fact that the counters are not located on the focus line but are placed symmetrically on each side.

Fig. 40 The zone of acceptance for particles produced in strips of the converter at a height $Z = Z_o$ and with an initial angle θ in the vertical plane. From the limiting angles the efficiency can be computed for various thicknesses and heights of the converter.

Fig. 41 The theoretical and experimental yields for various converter thicknesses. The theoretical curve has been used to weight all the effects in the resolution which depend upon converter thickness. The experimental points were measured with neutral mesons γ-rays; probable errors are shown.

Fig. 42 Gamma ray energy distribution resulting from radiation of the pair fragments leaving the converter. The curve shown results from pairs produced at the center of the converter.

Fig. 43 The distribution of γ-ray energies which results from ionization loss of pairs. The curve shown results from pairs produced at the center of the converter.

Fig. 44 The qualitative effect of ionization loss of pair fragments in the converter when averaged over the converter thickness. The low energy tail comes from the fluctuation of the ionization effect (Landau effect).

Fig. 45 Combined resolving power due to ionization, radiation and scattering. These are the first order effects which depend upon converter thickness. Each curve represents a thickness increment of the converter.

Fig. 46 The resolution due to first order converter thickness effects averaged over the converter.

Fig. 47 Mass data with first order resolving power only. Probable errors are shown. The channel width of Fig. 38 has been folded into the converter effects. The semi-logarithmic scale emphasizes the discrepancy at the tails of the distribution.

Fig. 48 Resolving power resulting from the finite lateral width of the converter. This term is the largest second order effect. It depends only however upon the first order solutions to the orbit perturbation problem. (The effect of the second order orbit perturbation theory has not been included in this curve.)

Fig. 49 Differential analyzer input function R(s) which represents the perturbation term in the ρ equation when there is an initial $\rho(o) = 1$ with all other initial conditions set equal to zero. Case 1 three different energies are shown, for one side of the spectrometer.

Fig. 50 Solution of perturbation for initial conditions of Case 1. From this the family of solutions for various initial conditions can be found corresponding to the second order abberation due to the horizontal width of the converter.

Fig. 51 The analyzer input function for the case $\rho'(o) = \theta_M$ where θ_M is the root mean square horizontal angle of scattering in the converter. The other initial conditions are all zero. Case 2.

Fig. 52 The solution of Case 2 for the horizontal scattering in the second order theory.

Fig. 53 The analyzer input function for the initial displacement in the vertical direction $Z(o) = 1$. Case 5.

Fig. 54 The solution in the ρ plane for the vertical height effect of the converter. Case 5.

Fig. 55 The analyzer input functions for the initial vertical scattering where $Z'(o) = \theta_M$. θ_M is the vertical root mean square angle of scattering. Case 6.

Fig. 56 Solution in the ρ equation due to vertical scattering. Case 6.

Fig. 57 Resolution component due to scattering in the horizontal plane due to the second order perturbations in the orbits.

Fig. 58 This curve is the surface of ΔE due to Z and Z' perturbations when projected into the ΔE, Z' plane. Z has been replaced by χ which is Z'/θ_M. This curve is essentially independent of the energy of the particle orbit, and the constants represent an averaging over all the analyzer cases involved.

Fig. 59 The second order energy resolution component due to vertical scattering and vertical height of the converter. This curve is obtained using the simplified model involving a single particle with twice the mean squared angle.

Fig. 60 The resolution curve which includes all the first and second order effects calculated by folding together the resolution components which are statistically independent.

Fig. 61 The pion capture γ-ray spectrum which is obtained by using a 0.050 in. tantalum converter. Probable errors are shown. The solid curve is the estimated resolution. The effects due to scattering out losses are difficult to include.

Fig. 62 The capture spectrum obtained by using a 0.020 in. tantalum converter probable errors are shown. The solid curve is the calculated resolution.

Fig. 63 The capture spectrum measured with the thin target, 0.010 in. tantalum, compared to the spectrum obtained by Panofsky, et al. The solid curves are theoretical resolution curves. Probable errors are shown.

Fig. 64 Experimental and theoretical yields for various converter shapes. Experimental points were obtained from π^o gamma rays from the primary target. Probable errors are shown.

Fig. 65 π^o gamma ray spectrum from protons on wolfram measured at 180 degrees, using three overlapping field settings where energy dependent loss corrections are negligible.

Fig. 66 π^o gamma ray spectrum from 340 Mev protons on wolfram target using the focussing spectrometer. The solid line is from the data taken using conventional 90 degree spectrometer. Probable errors are shown. The results show that the losses are unimportant over the range of energies considered.

Fig. 67 Gamma ray background from the empty hydrogen vessel. The solid line is obtained from the π^o decay gamma's which are produced at the primary target with 340 Mev protons. Since the energy of the primary protons is reduced to $\sim$330 Mev when the primary target is in the position at which the meson capture spectrum is measured, one would expect the higher energy gamma ray yield to be reduced. Probable errors are shown.

Fig. 68 The meson capture spectrum is shown with a gaussian of RMS width of 1 Mev. The agreement extends to approximately 10 percent of the maximum intensity.

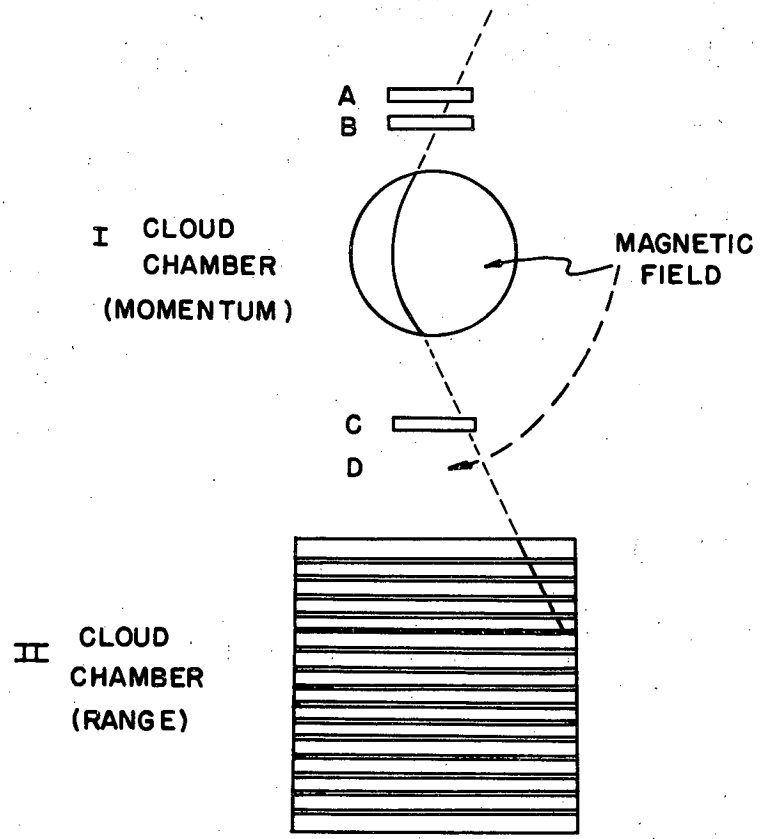
A
B
I CLOUD CHAMBER (MOMENTUM)
MAGNETIC FIELD
C
D
II CLOUD CHAMBER (RANGE)

MU-4572

Fig. 1

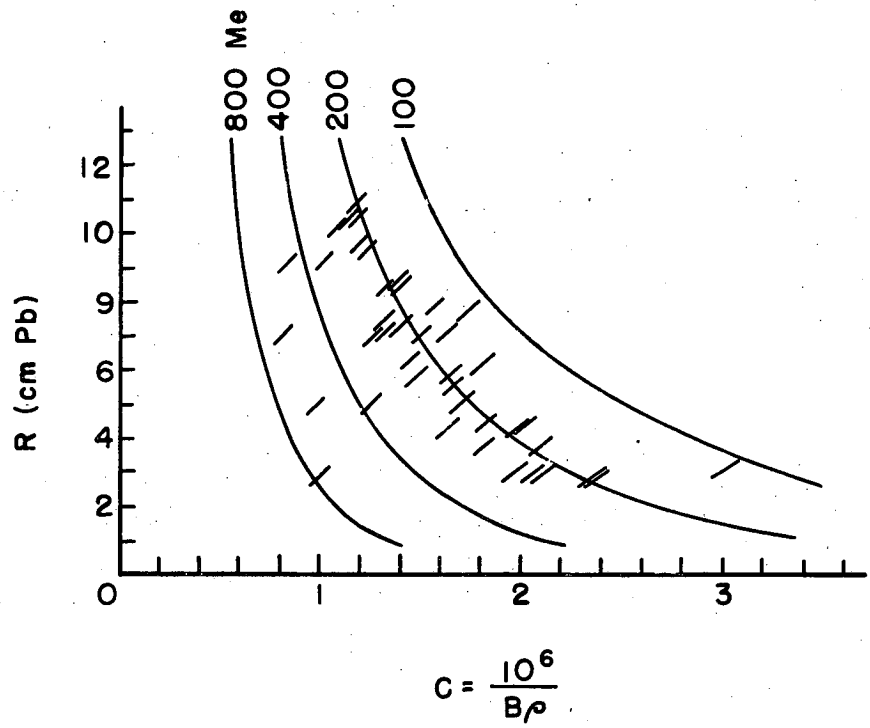

MU-4540

Fig. 2

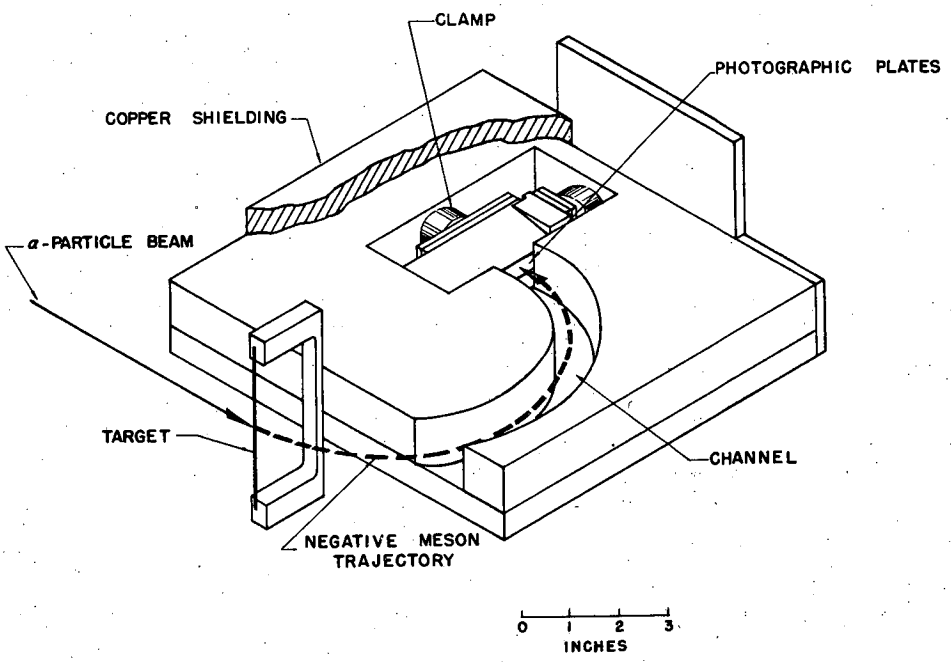

HOLDER FOR MASS MEASUREMENT STUDIES

MU 349

Fig. 3

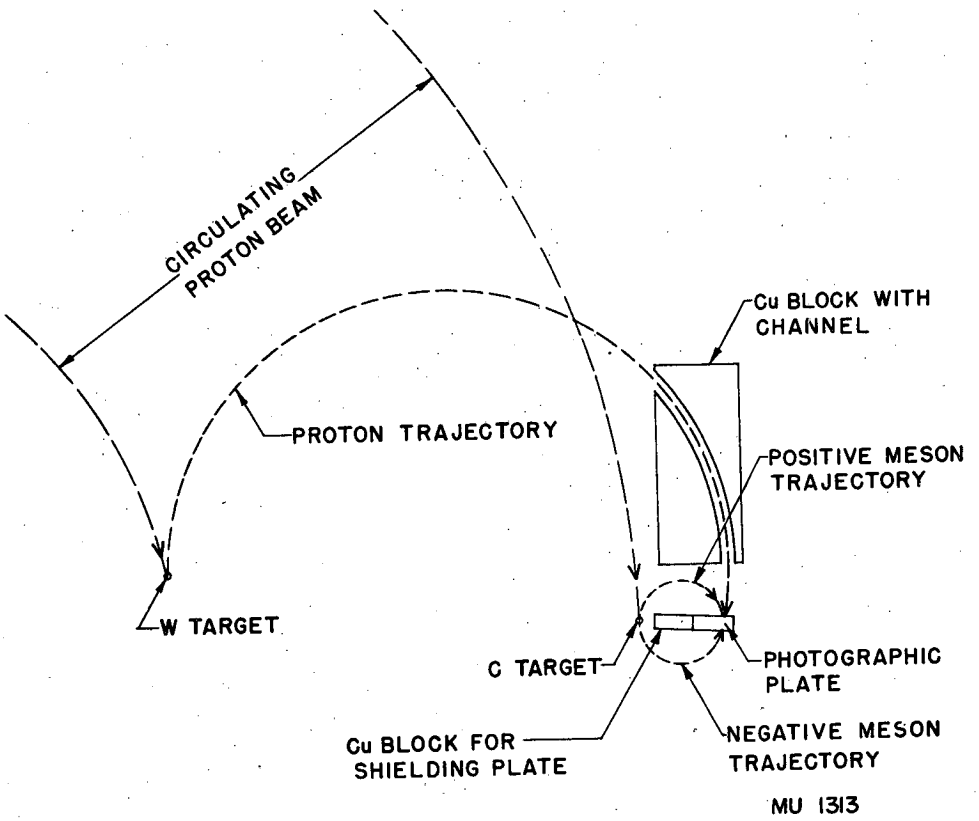
CIRCULATING
PROTON BEAM
Cu BLOCK WITH
CHANNEL
PROTON TRAJECTORY
POSITIVE MESON
TRAJECTORY
W TARGET
C TARGET
PHOTOGRAPHIC
PLATE
Cu BLOCK FOR
SHIELDING PLATE
NEGATIVE MESON
TRAJECTORY
MU 1313

Fig. 4

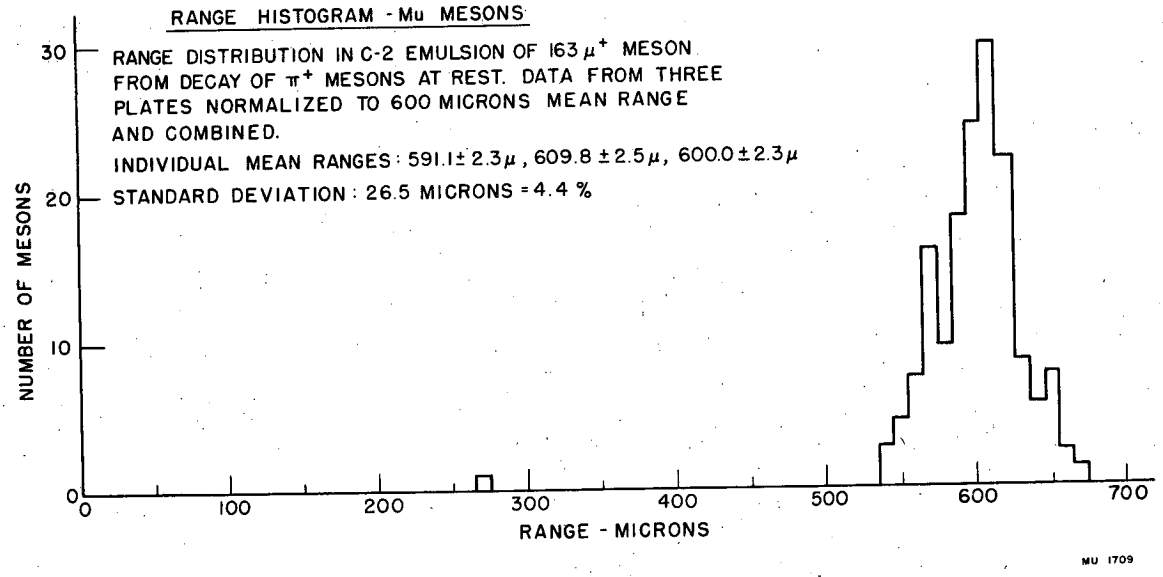
RANGE HISTOGRAM - Mu MESONS
RANGE DISTRIBUTION IN C-2 EMULSION OF 163 μ+ MESON FROM DECAY OF π+ MESONS AT REST. DATA FROM THREE PLATES NORMALIZED TO 600 MICRONS MEAN RANGE AND COMBINED.
INDIVIDUAL MEAN RANGES: 591.1± 2.3μ, 609.8 ±2.5μ, 600.0±2.3μ
STANDARD DEVIATION: 26.5 MICRONS = 4.4 %
NUMBER OF MESONS
30
20
10
0
0
100
200
300
400
500
600
700
RANGE - MICRONS
MU 1709

Fig. 5

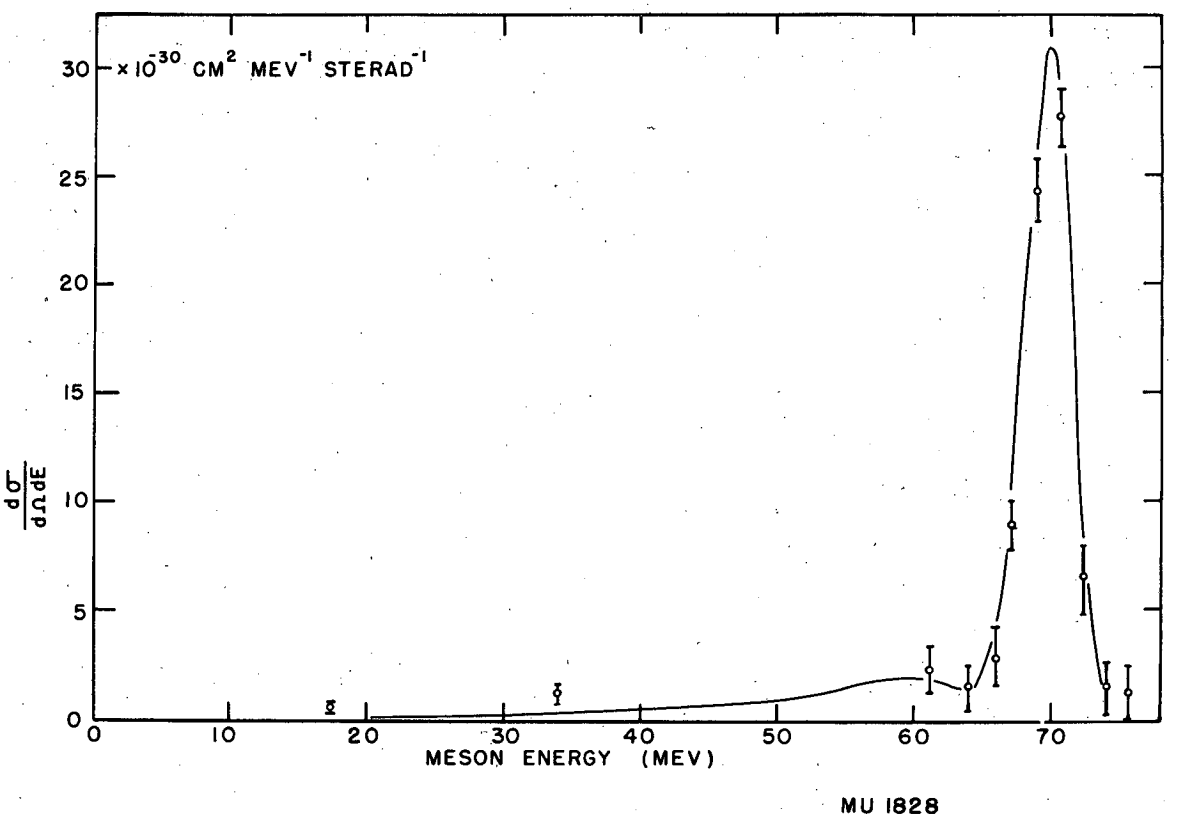
× 10^-30 CM^2 MEV^-1 STERAD^-1
30
25
20
15
10
5
0
dσ/dΩdE
0
10
20
30
40
50
60
70
MESON ENERGY (MEV)
MU 1828

Fig. 6

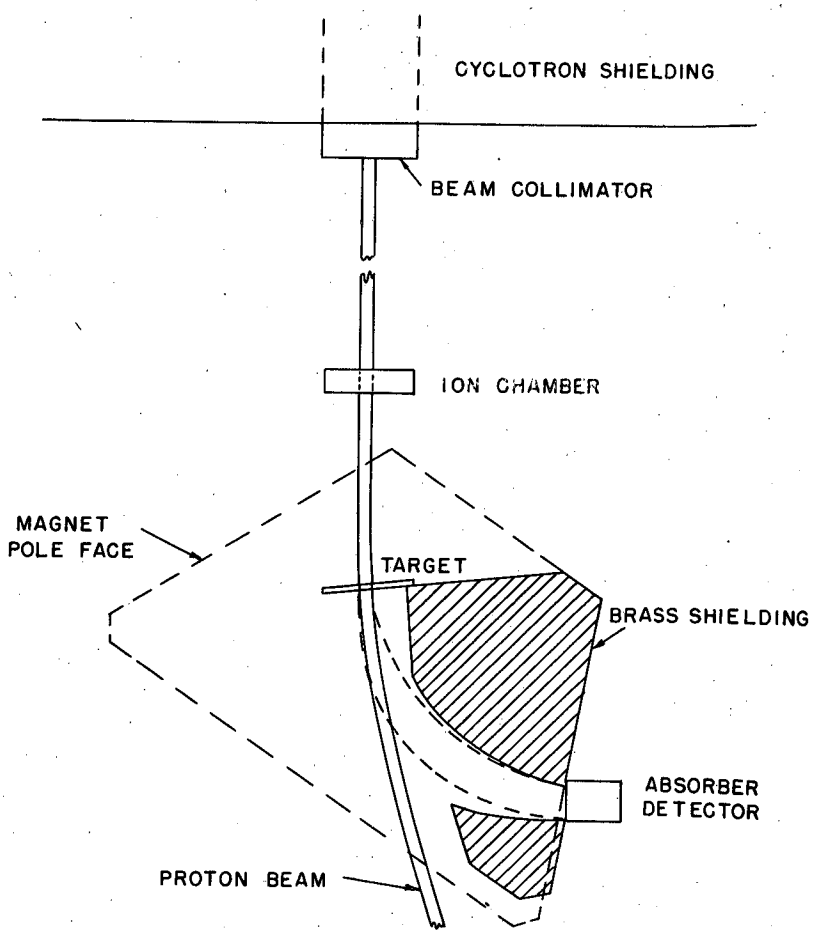
CYCLOTRON SHIELDING
BEAM COLLIMATOR
ION CHAMBER
MAGNET
POLE FACE
TARGET
BRASS SHIELDING
ABSORBER
DETECTOR
PROTON BEAM
MU 1824

Fig. 7

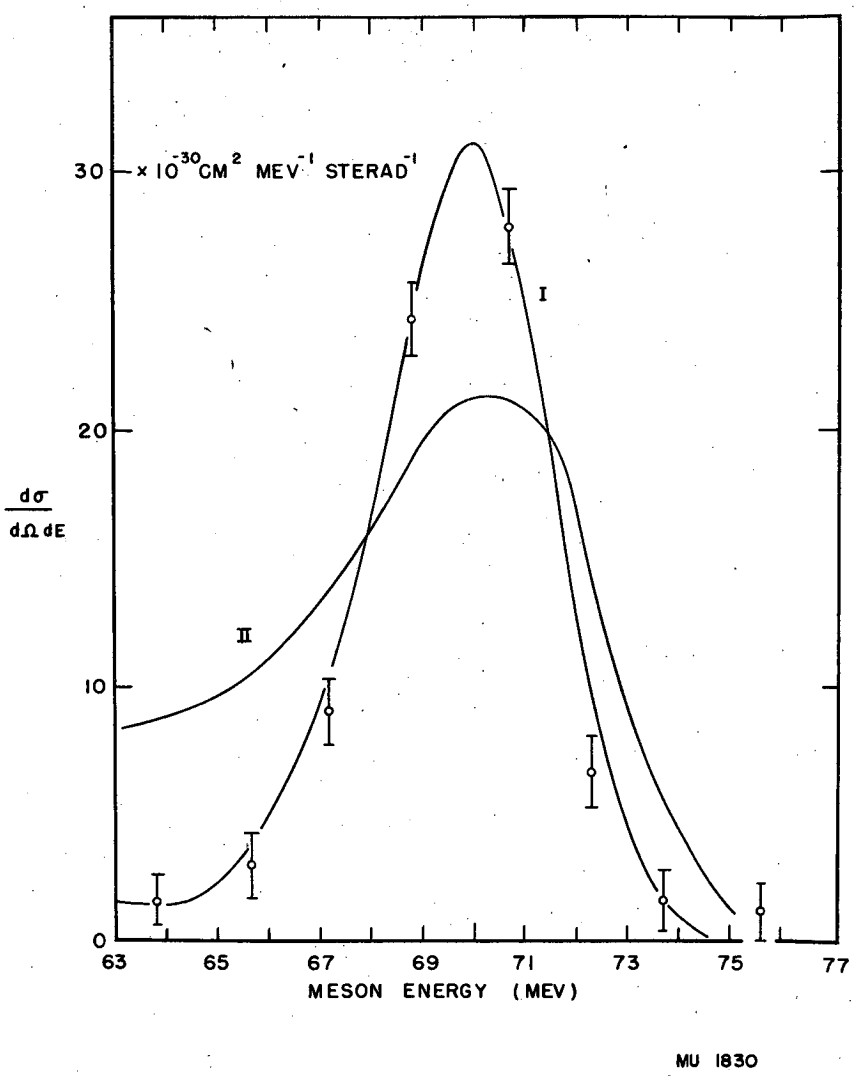
30
20
10
0
× 10⁻³⁰ CM² MEV⁻¹ STERAD⁻¹
dσ / dΩ dE
I
II
63
65
67
69
71
73
75
77
MESON ENERGY (MEV)
MU 1830

Fig. 8

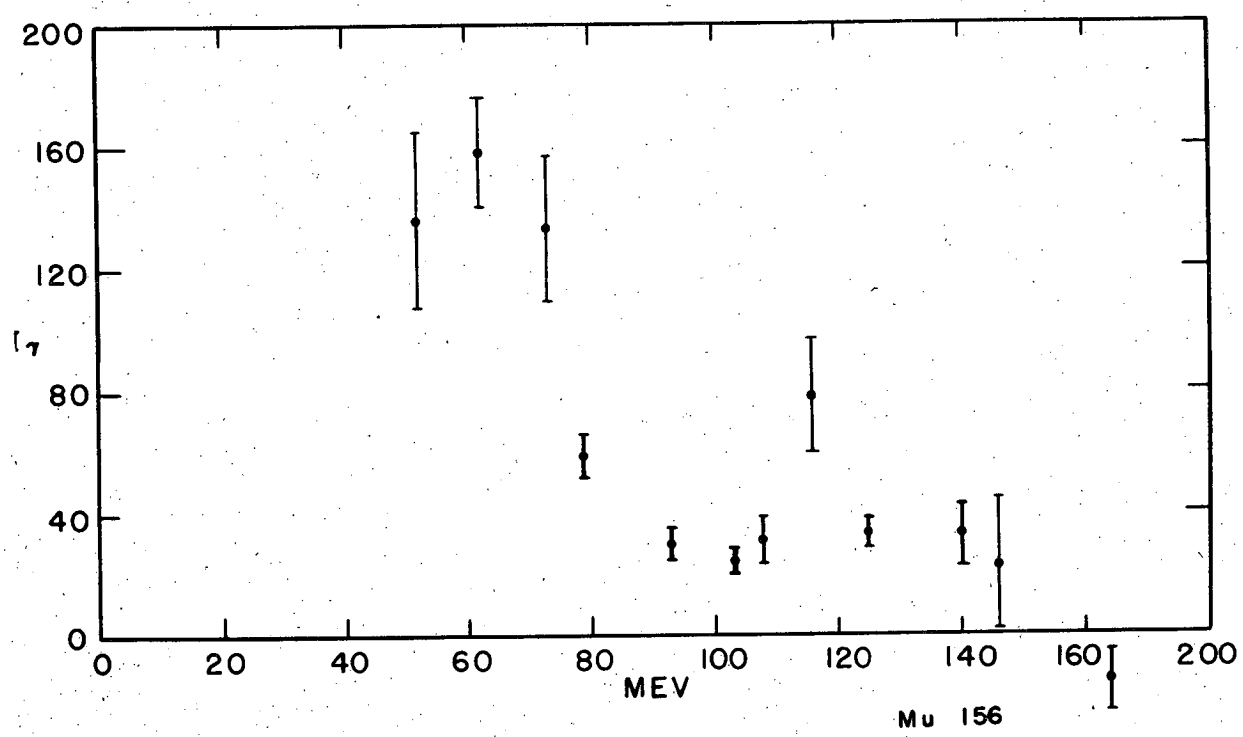
200
160
120
80
40
0
Γ_γ
0
20
40
60
80
100
120
140
160
200
MEV
Mu 156

Fig. 9

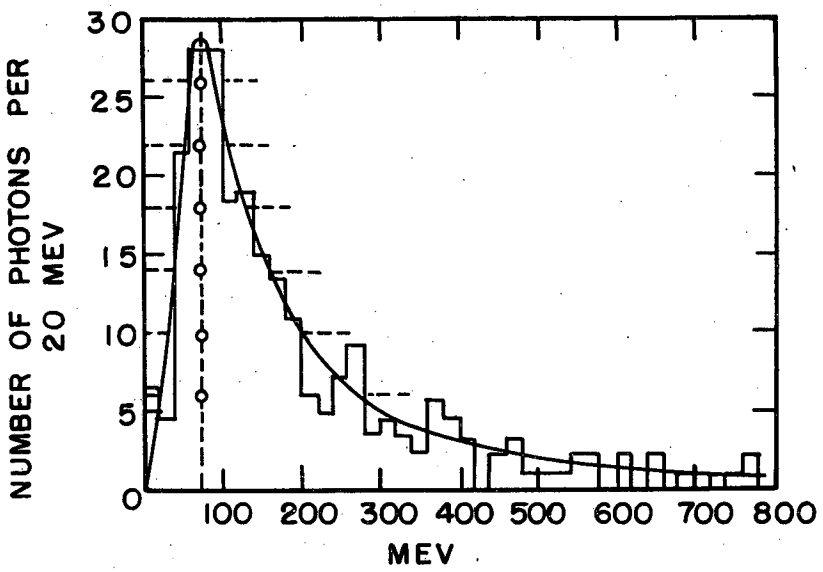

MU-4537

Fig. 10

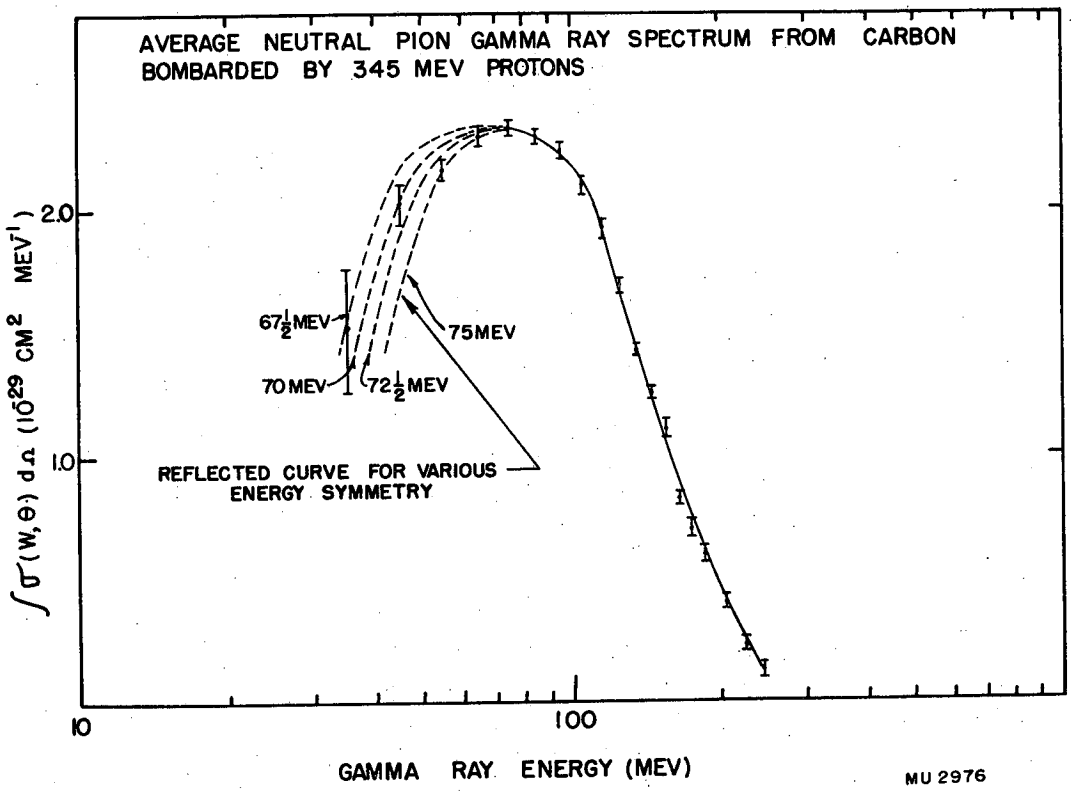
AVERAGE NEUTRAL PION GAMMA RAY SPECTRUM FROM CARBON BOMBARDED BY 345 MEV PROTONS
67½ MEV
70 MEV
72½ MEV
75 MEV
REFLECTED CURVE FOR VARIOUS ENERGY SYMMETRY
2.0
1.0
10
100
GAMMA RAY ENERGY (MEV)
MU 2976

Fig. 11

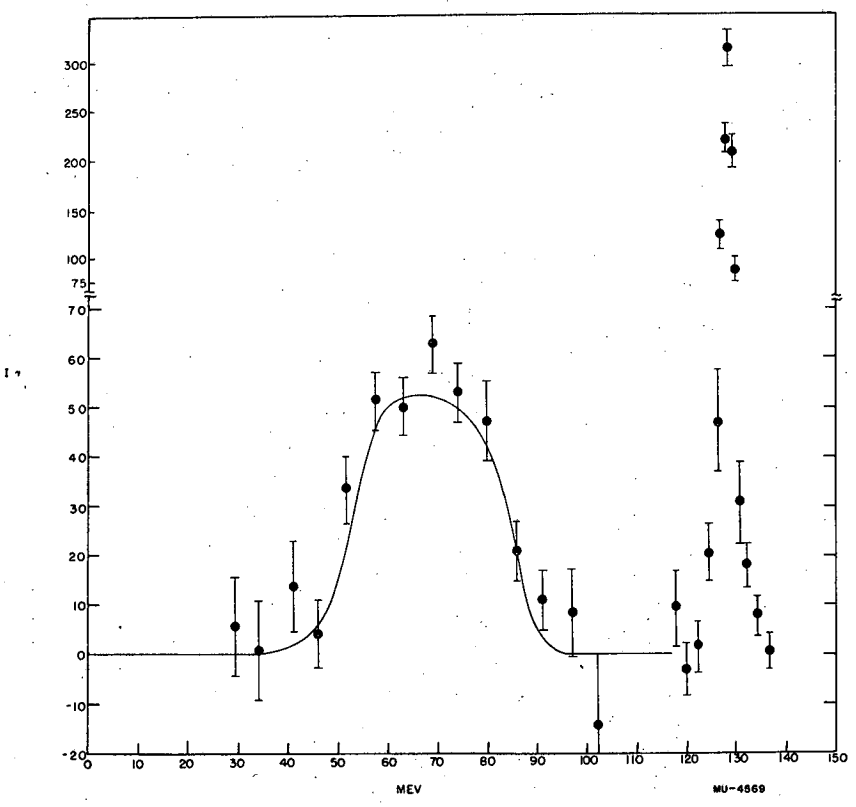
300
250
200
150
100
75
70
60
50
40
30
20
10
0
-10
-20
0
10
20
30
40
50
60
70
80
90
100
110
120
130
140
150
MEV
MU-4569

Fig. 12

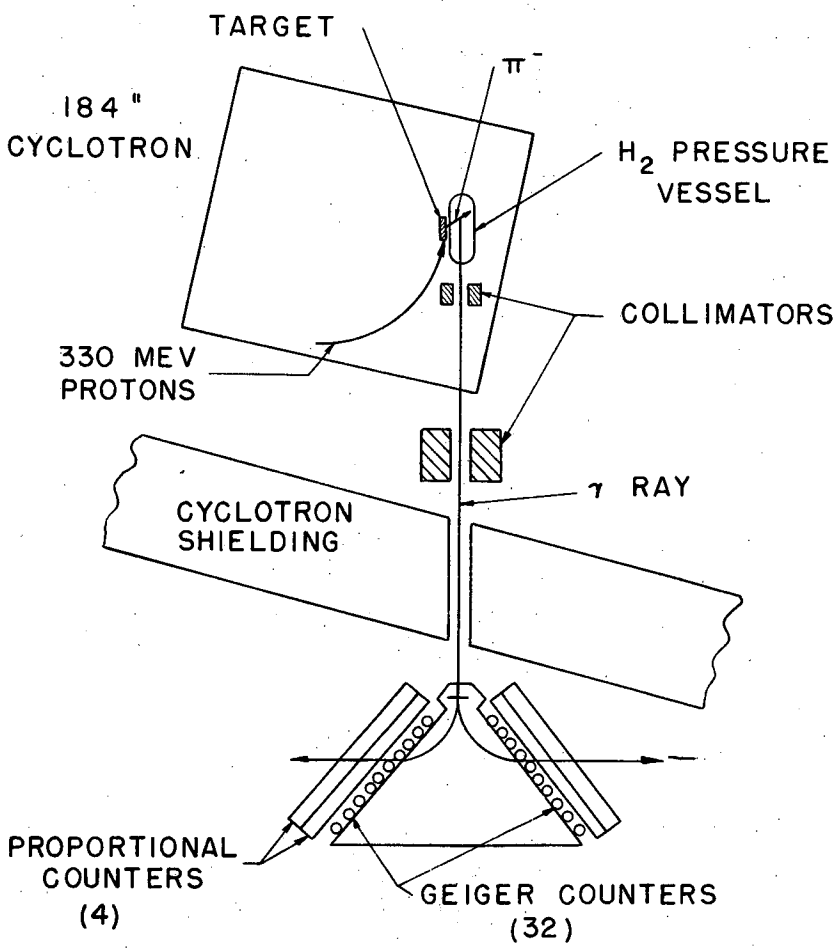
TARGET
π⁻
184"
CYCLOTRON
H2 PRESSURE
VESSEL
COLLIMATORS
330 MEV
PROTONS
γ RAY
CYCLOTRON
SHIELDING
PROPORTIONAL
COUNTERS
(4)
GEIGER COUNTERS
(32)
MU 791

Fig. 13

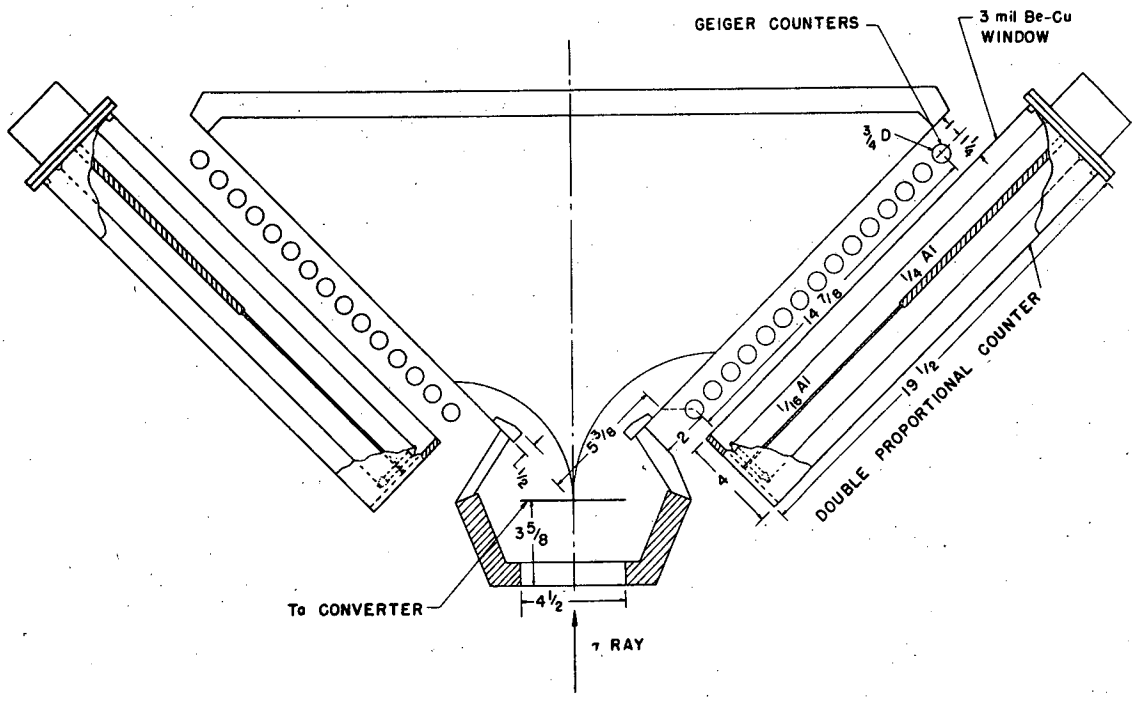
GEIGER COUNTERS
3 mil Be-Cu WINDOW
3/4 D
1/4
14 7/8
1/4 Al
1/16 Al
19 1/2
DOUBLE PROPORTIONAL COUNTER
5 3/8
1/2
2
4
3 5/8
4 1/2
To CONVERTER
γ RAY
MU 794

Fig. 14

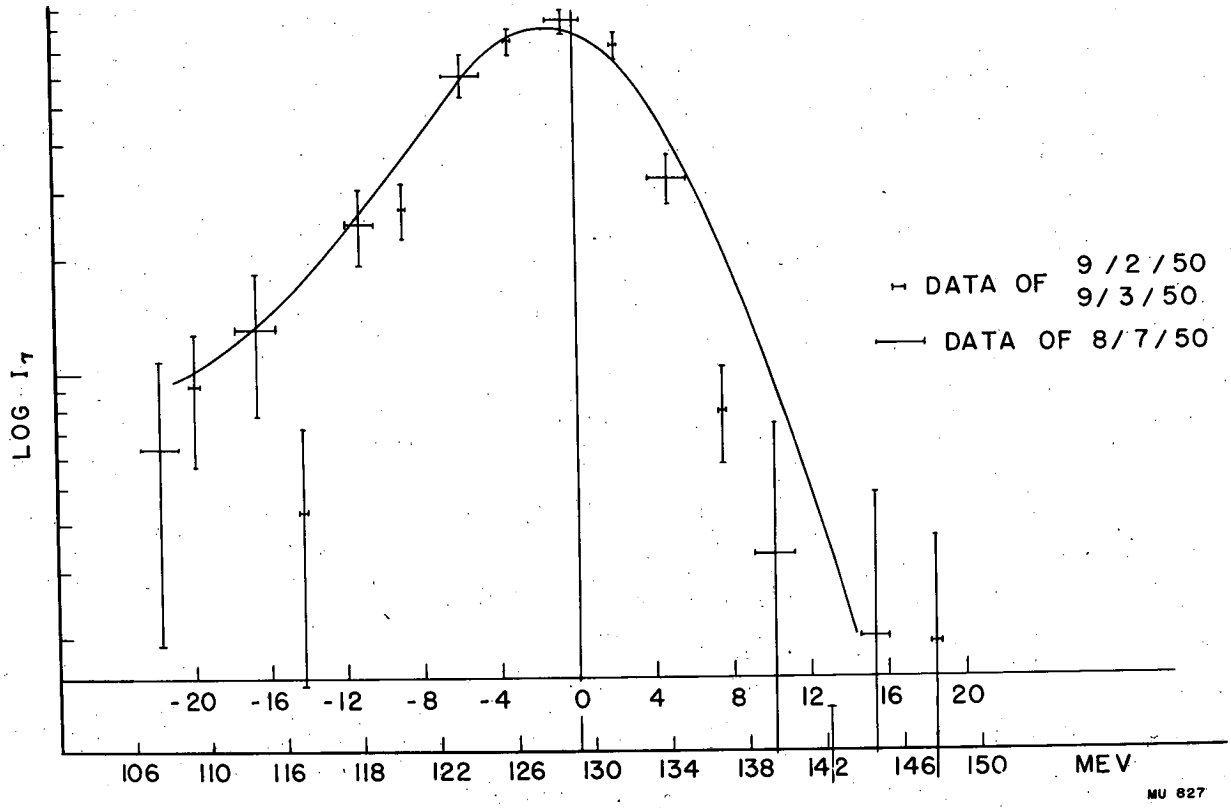
LOG I_γ
DATA OF 9/2/50
9/3/50
DATA OF 8/7/50
-20
-16
-12
-8
-4
0
4
8
12
16
20
106
110
116
118
122
126
130
134
138
142
146
150
MEV
MU 827

Fig. 15

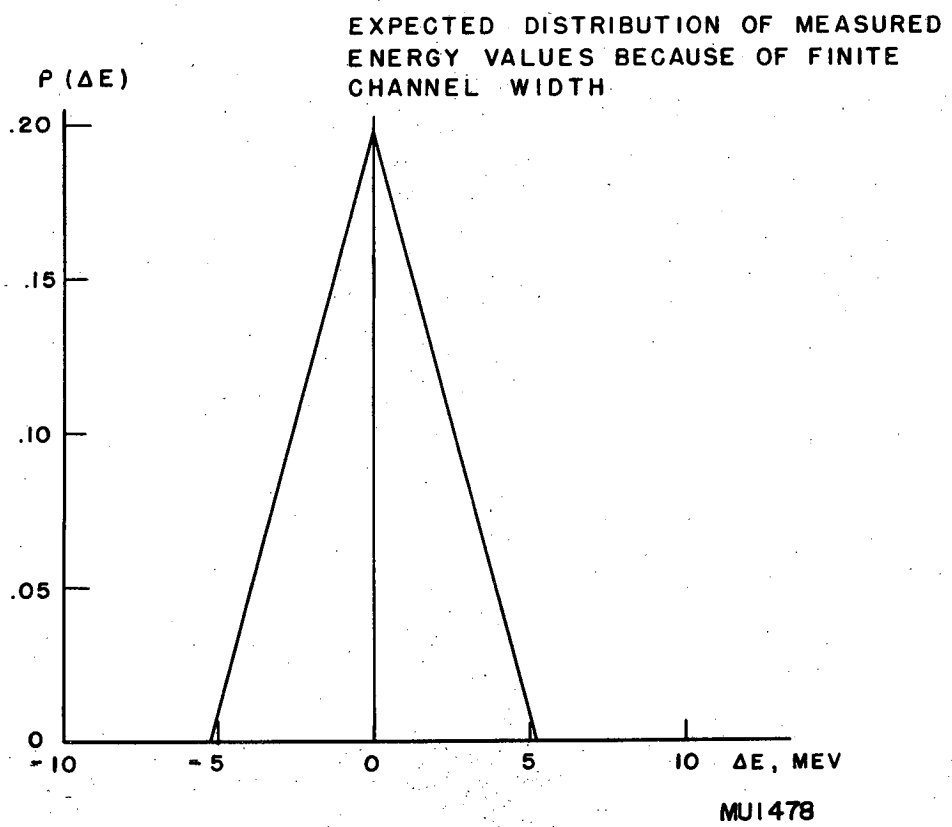
EXPECTED DISTRIBUTION OF MEASURED ENERGY VALUES BECAUSE OF FINITE CHANNEL WIDTH
P (ΔE)
.20
.15
.10
.05
0
-10
-5
0
5
10
ΔE, MEV
MU1478

Fig. 16

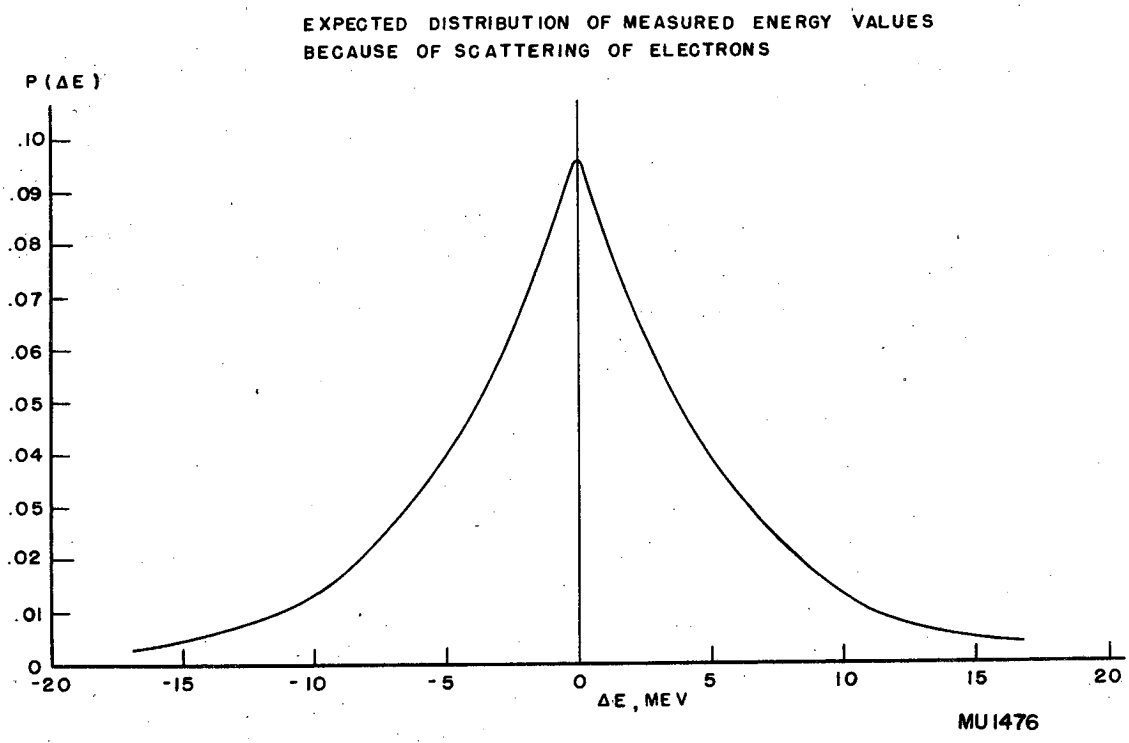
EXPECTED DISTRIBUTION OF MEASURED ENERGY VALUES
BECAUSE OF SCATTERING OF ELECTRONS
P(ΔE)
.10
.09
.08
.07
.06
.05
.04
.05
.02
.01
0
-20
-15
-10
-5
0
5
10
15
20
ΔE, MEV
MU1476

Fig. 17

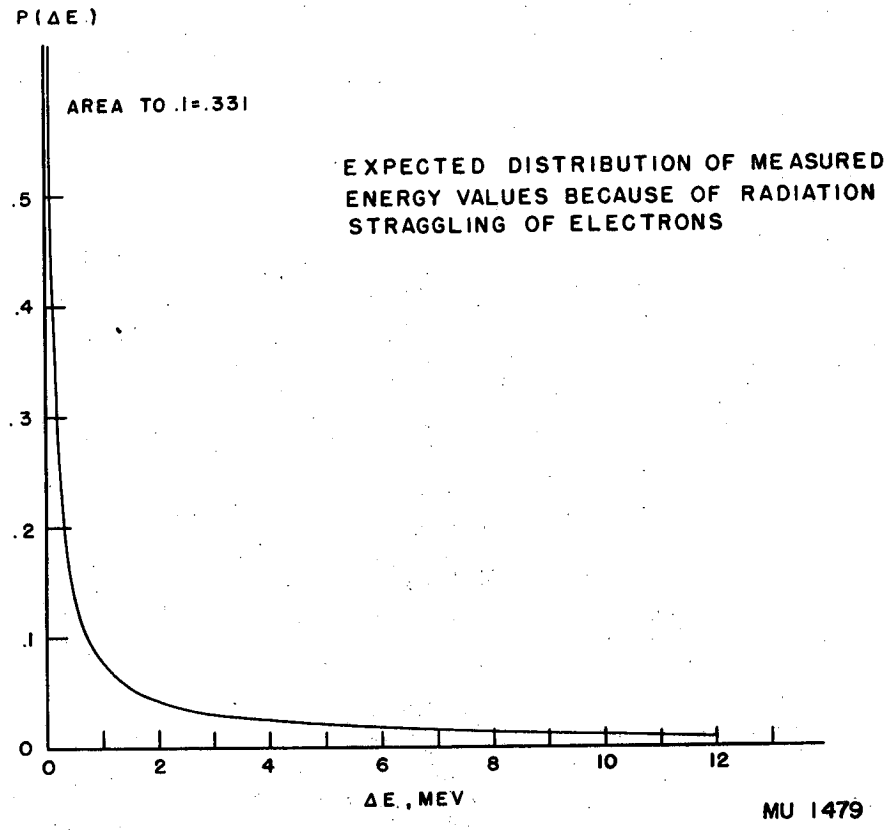
P(ΔE)
AREA TO .1=.331
EXPECTED DISTRIBUTION OF MEASURED ENERGY VALUES BECAUSE OF RADIATION STRAGGLING OF ELECTRONS
.5
.4
.3
.2
.1
0
0
2
4
6
8
10
12
ΔE, MEV
MU 1479

Fig. 18

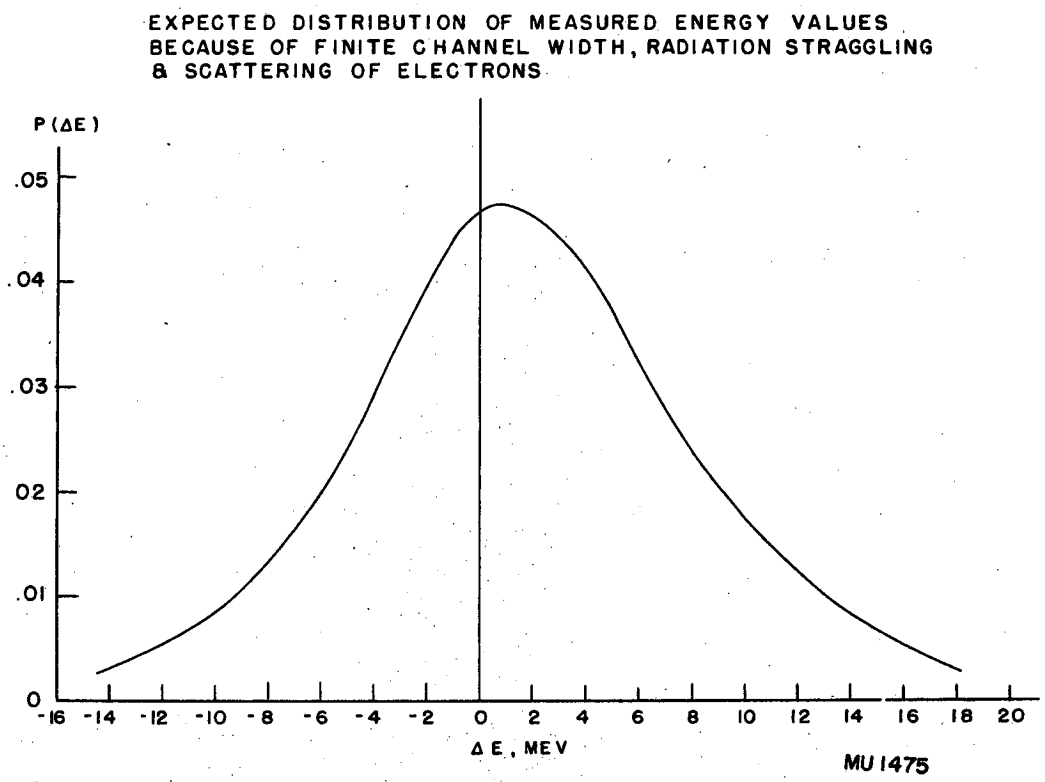
EXPECTED DISTRIBUTION OF MEASURED ENERGY VALUES
BECAUSE OF FINITE CHANNEL WIDTH, RADIATION STRAGGLING
& SCATTERING OF ELECTRONS
P(ΔE)
.05
.04
.03
02
.01
0
-16 -14 -12 -10 -8 -6 -4 -2 0 2 4 6 8 10 12 14 16 18 20
Δ E, MEV
MU 1475

Fig. 19

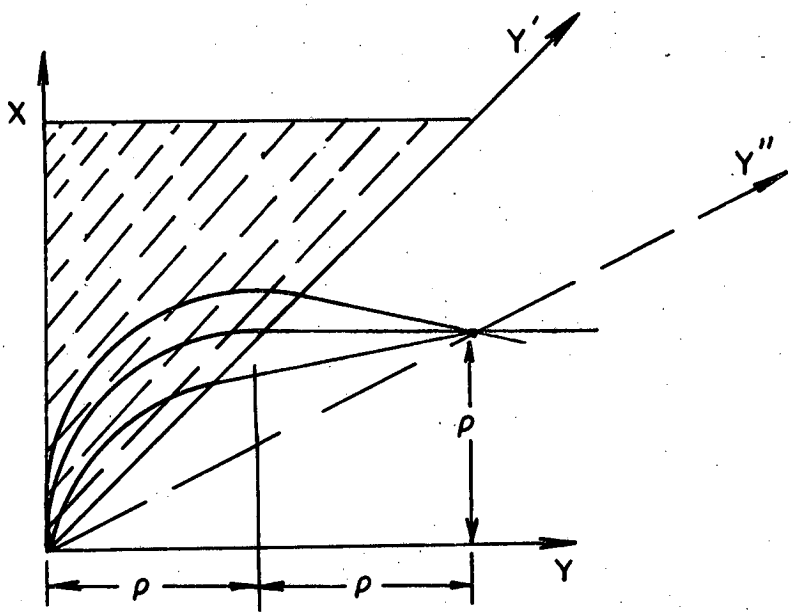

MU-4532

Fig. 20

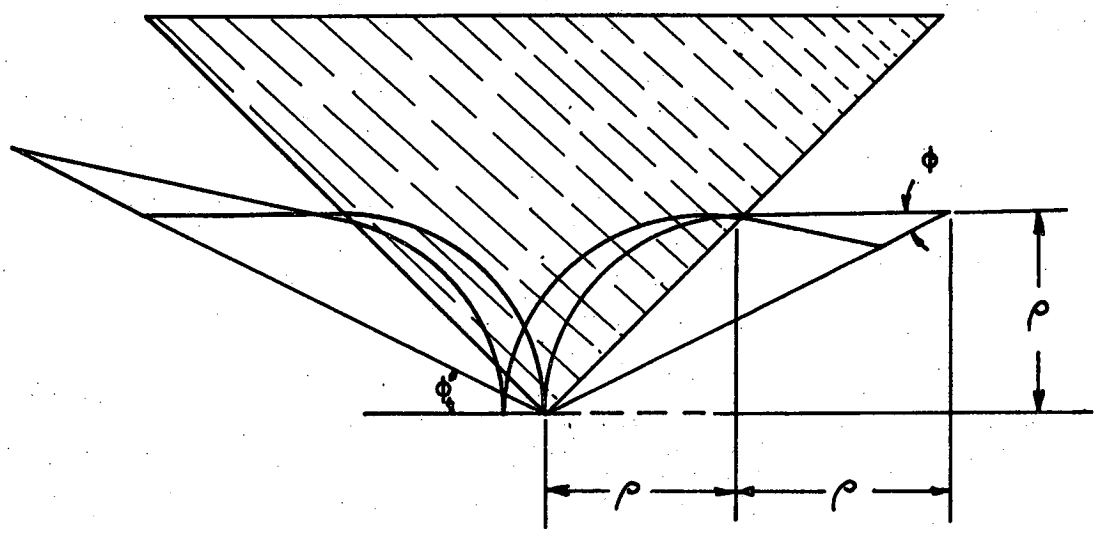

MU-4582

Fig. 21

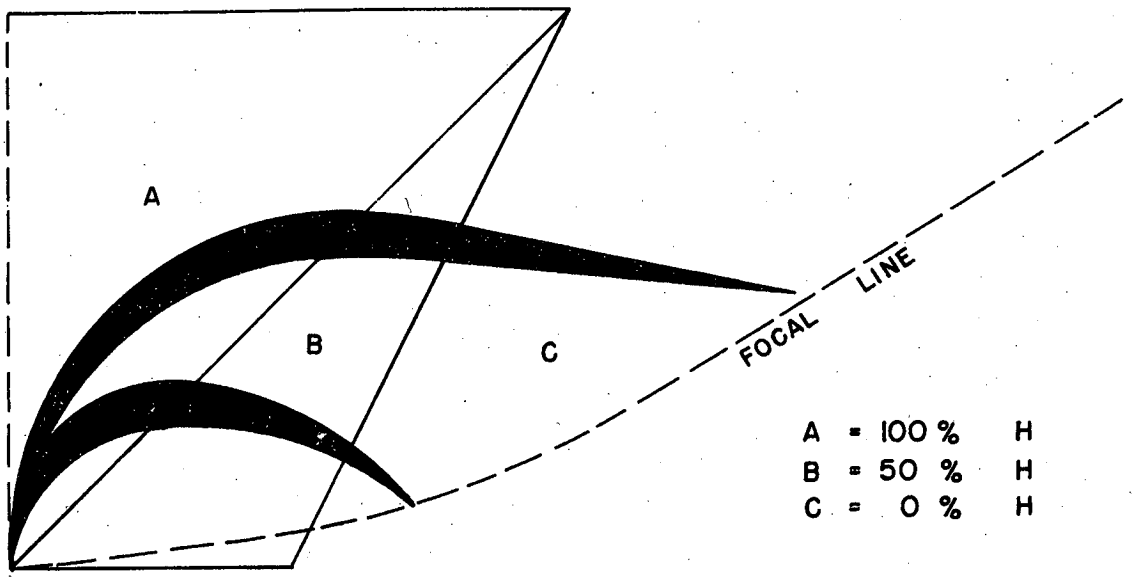

MU-4530

Fig. 22

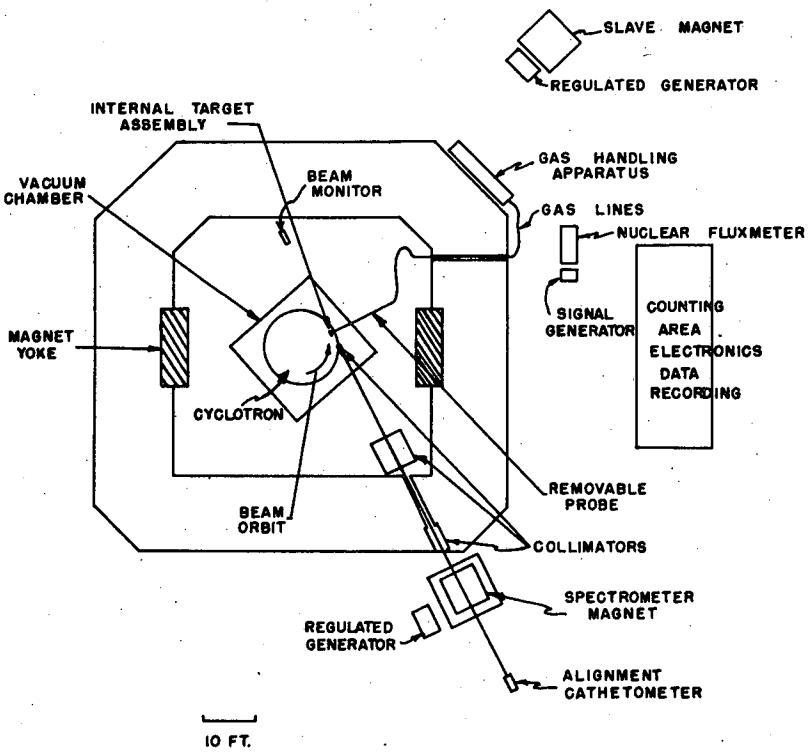
SLAVE MAGNET
REGULATED GENERATOR
INTERNAL TARGET ASSEMBLY
VACUUM CHAMBER
BEAM MONITOR
GAS HANDLING APPARATUS
GAS LINES
NUCLEAR FLUXMETER
SIGNAL GENERATOR
COUNTING AREA ELECTRONICS DATA RECORDING
MAGNET YOKE
CYCLOTRON
REMOVABLE PROBE
BEAM ORBIT
COLLIMATORS
SPECTROMETER MAGNET
REGULATED GENERATOR
ALIGNMENT CATHETOMETER
10 FT.
MU-4527

Fig. 23

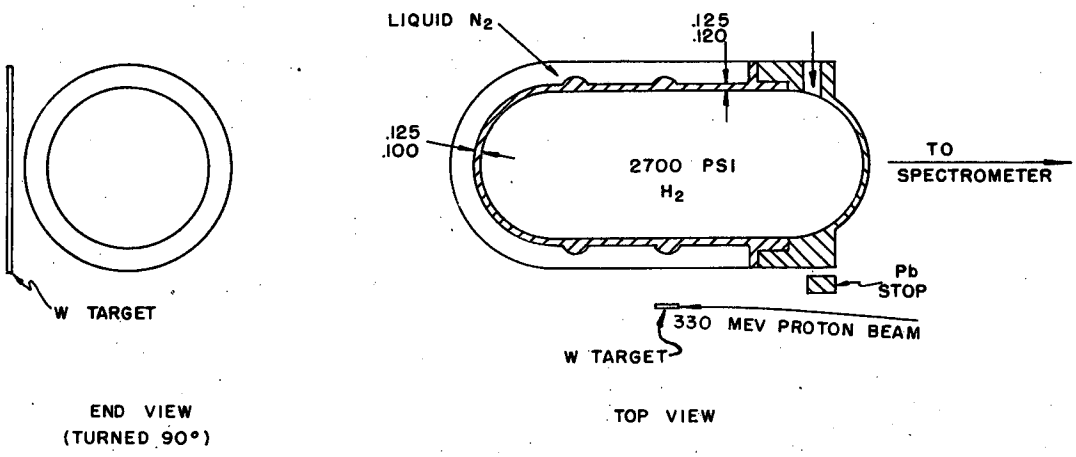
LIQUID N_2
.125
.120
.125
.100
2700 PSI
H_2
TO
SPECTROMETER
Pb
STOP
330 MEV PROTON BEAM
W TARGET
W TARGET
END VIEW
(TURNED 90°)
TOP VIEW
MU-4522

Fig. 24

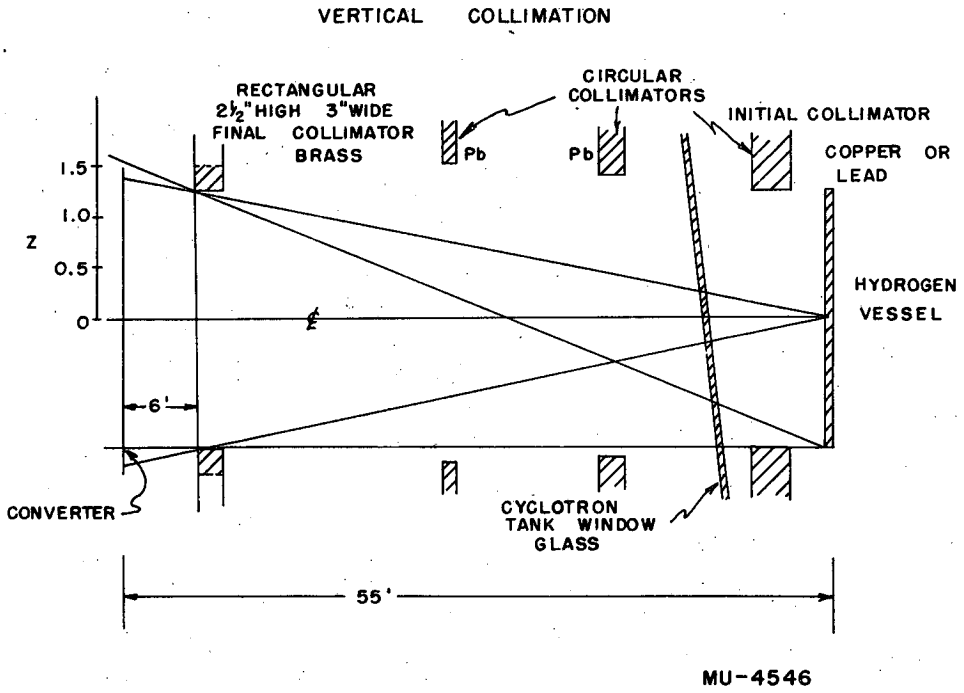
VERTICAL COLLIMATION
RECTANGULAR
2½"HIGH 3"WIDE
FINAL COLLIMATOR
BRASS
CIRCULAR
COLLIMATORS
Pb
Pb
INITIAL COLLIMATOR
COPPER OR
LEAD
HYDROGEN
VESSEL
1.5
1.0
Z
0.5
0
6'
CONVERTER
CYCLOTRON
TANK WINDOW
GLASS
55'
MU-4546

Fig. 25

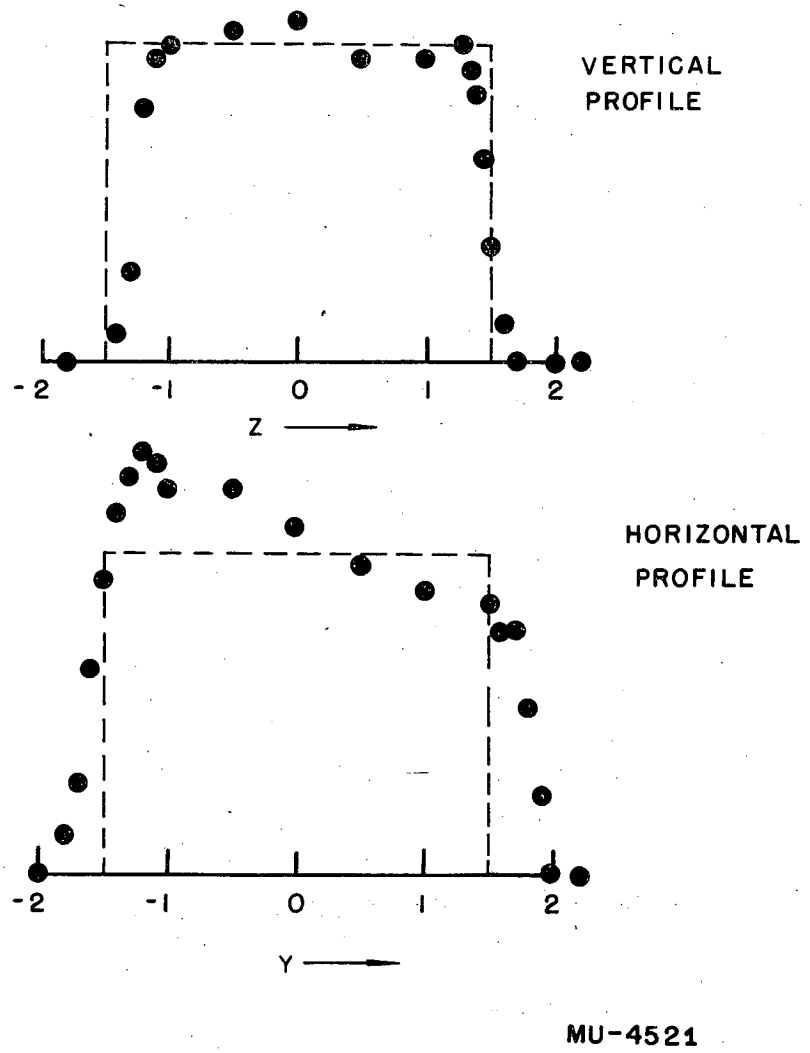
VERTICAL
PROFILE
-2
-1
0
1
2
Z
HORIZONTAL
PROFILE
-2
-1
0
1
2
Y
MU-4521

Fig. 26

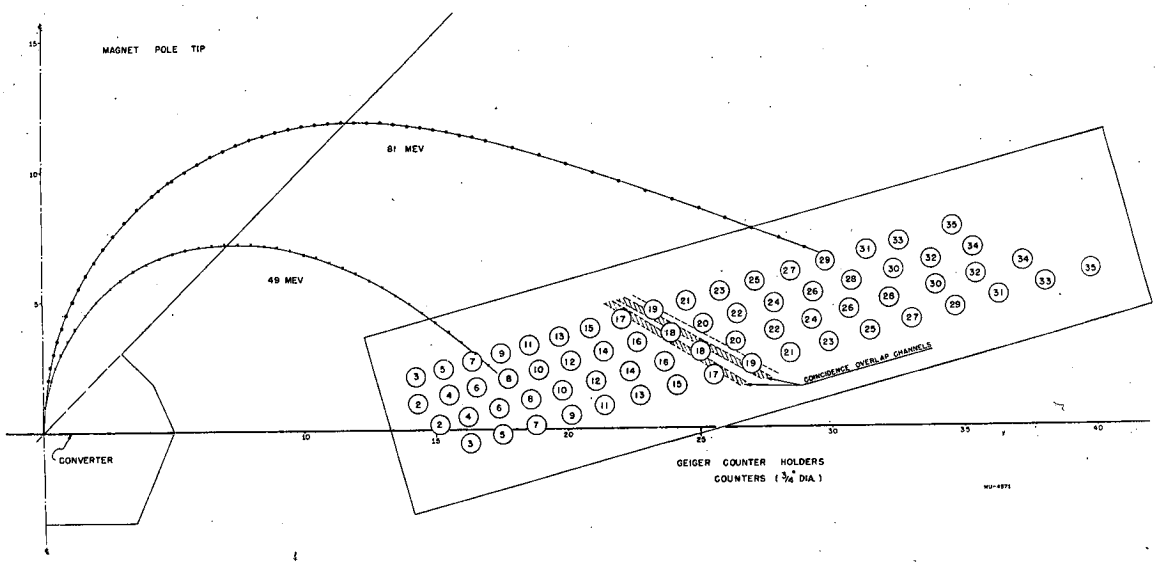
MAGNET POLE TIP
81 MEV
49 MEV
CONVERTER
COINCIDENCE OVERLAP CHANNELS
GEIGER COUNTER HOLDERS
COUNTERS (3/4" DIA.)

Fig. 27

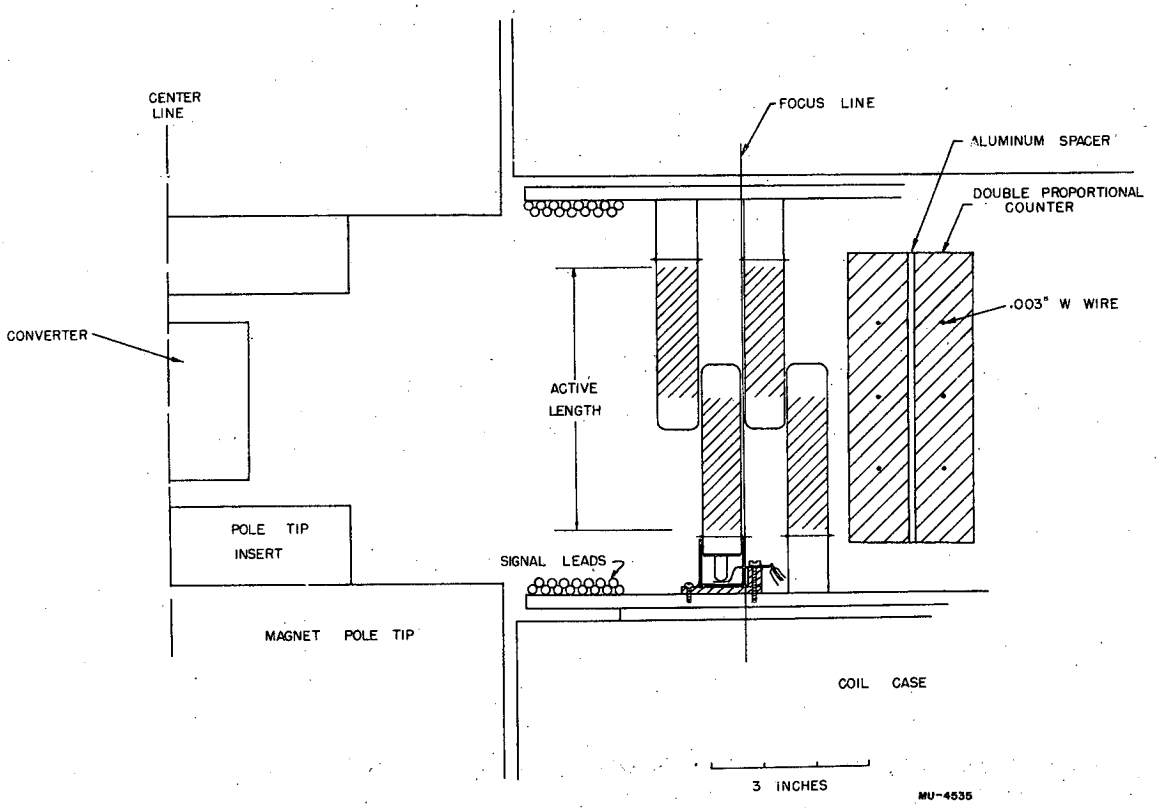
CENTER LINE
FOCUS LINE
ALUMINUM SPACER
DOUBLE PROPORTIONAL COUNTER
.003" W WIRE
CONVERTER
ACTIVE LENGTH
POLE TIP INSERT
SIGNAL LEADS
MAGNET POLE TIP
COIL CASE
3 INCHES
MU-4535

Fig. 28

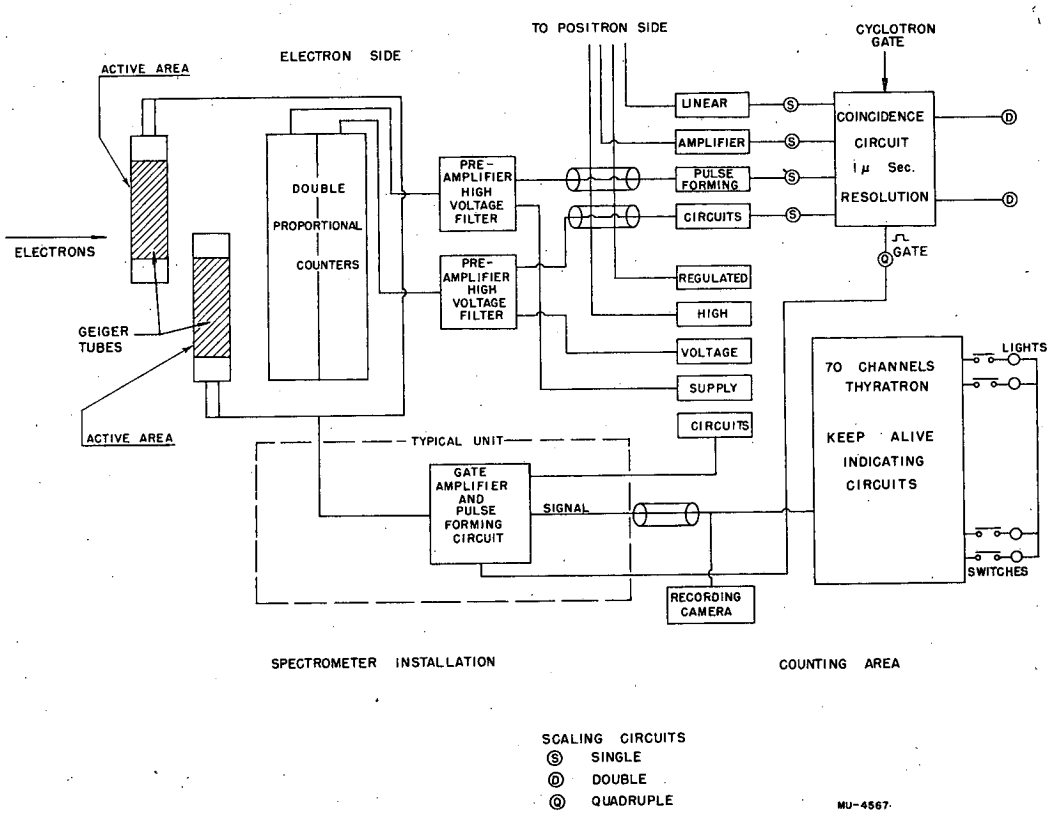
TO POSITRON SIDE
CYCLOTRON GATE
ELECTRON SIDE
ACTIVE AREA
ELECTRONS
GEIGER TUBES
ACTIVE AREA
DOUBLE PROPORTIONAL COUNTERS
PRE-AMPLIFIER HIGH VOLTAGE FILTER
PRE-AMPLIFIER HIGH VOLTAGE FILTER
LINEAR AMPLIFIER
PULSE FORMING CIRCUITS
REGULATED HIGH VOLTAGE SUPPLY CIRCUITS
COINCIDENCE CIRCUIT 1 μ Sec. RESOLUTION
GATE
70 CHANNELS THYRATRON KEEP ALIVE INDICATING CIRCUITS
LIGHTS
SWITCHES
TYPICAL UNIT
GATE AMPLIFIER AND PULSE FORMING CIRCUIT
SIGNAL
RECORDING CAMERA
SPECTROMETER INSTALLATION
COUNTING AREA
SCALING CIRCUITS
(S) SINGLE
(D) DOUBLE
(Q) QUADRUPLE
MU-4567

Fig. 29

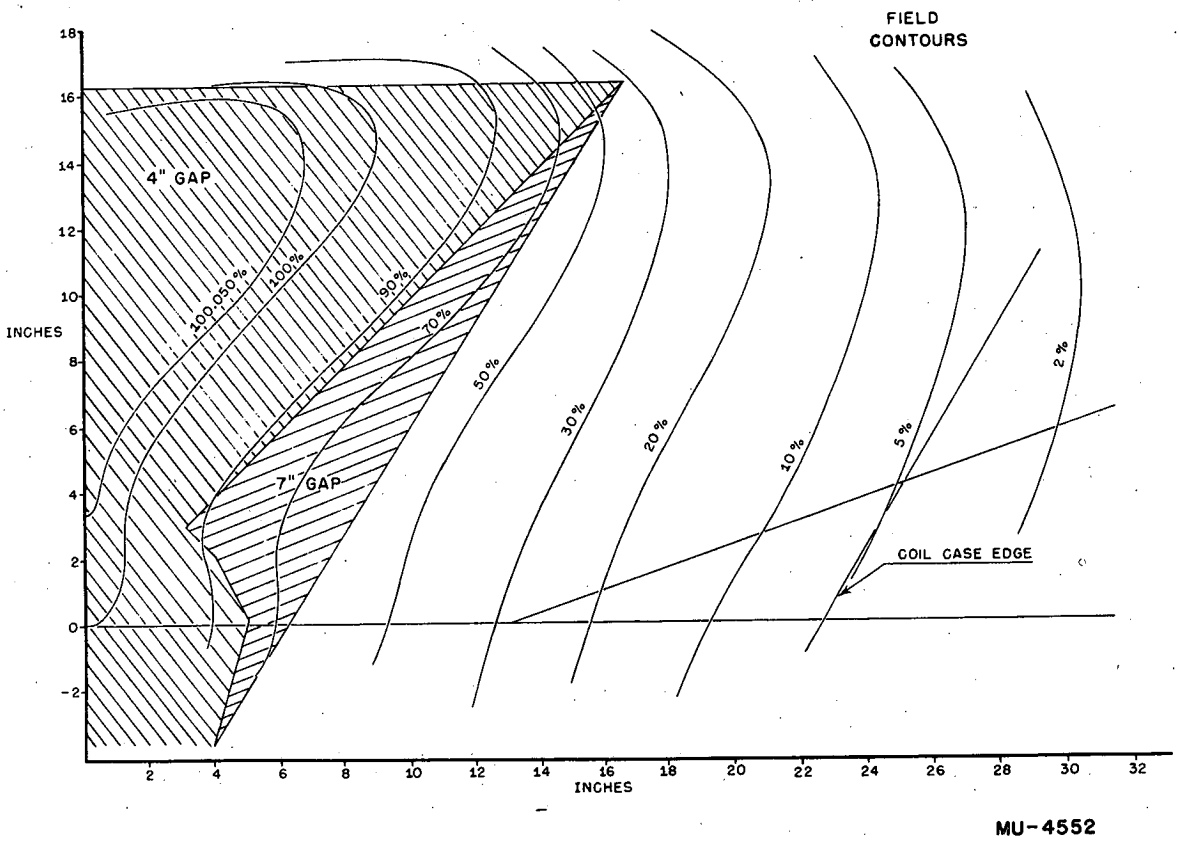
FIELD
CONTOURS
4" GAP
7" GAP
100.050%
100%
90%
70%
50%
30%
20%
10%
5%
2%
COIL CASE EDGE
INCHES
INCHES
18
16
14
12
10
8
6
4
2
0
-2
2
4
6
8
10
12
14
16
18
20
22
24
26
28
30
32
MU-4552

Fig. 30

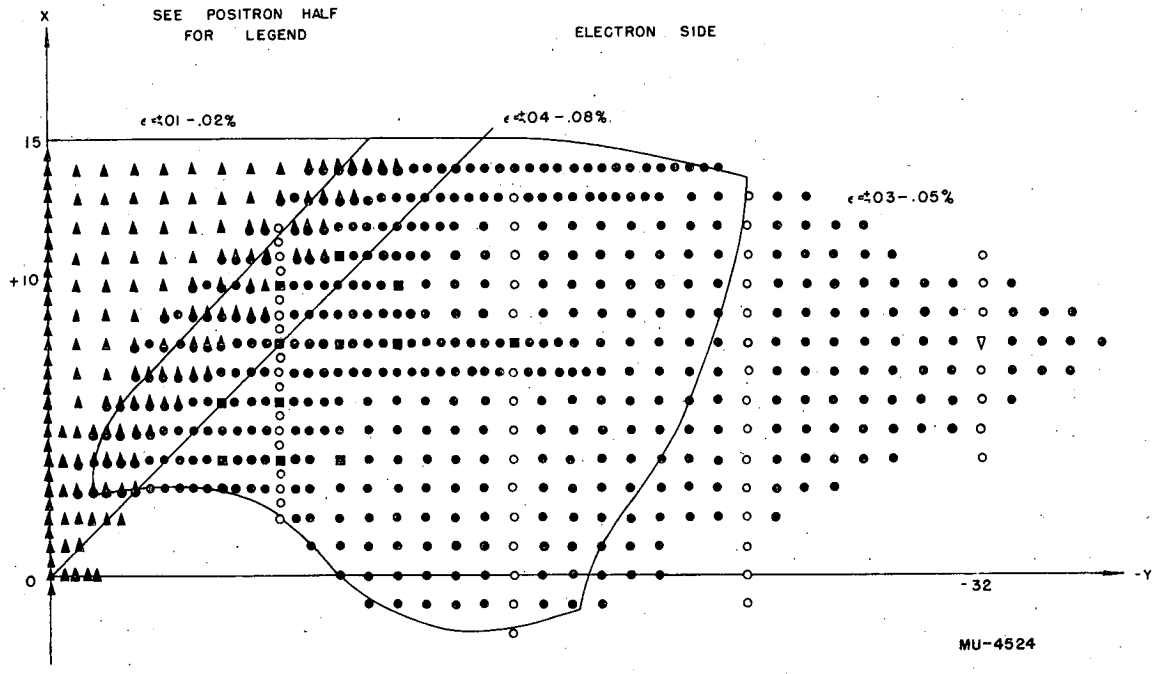
X
SEE POSITRON HALF
FOR LEGEND
ELECTRON SIDE
ε=.01 -.02%
ε=.04 -.08%
ε=.03-.05%
15
+10
0
-32
-Y
MU-4524

Fig. 31

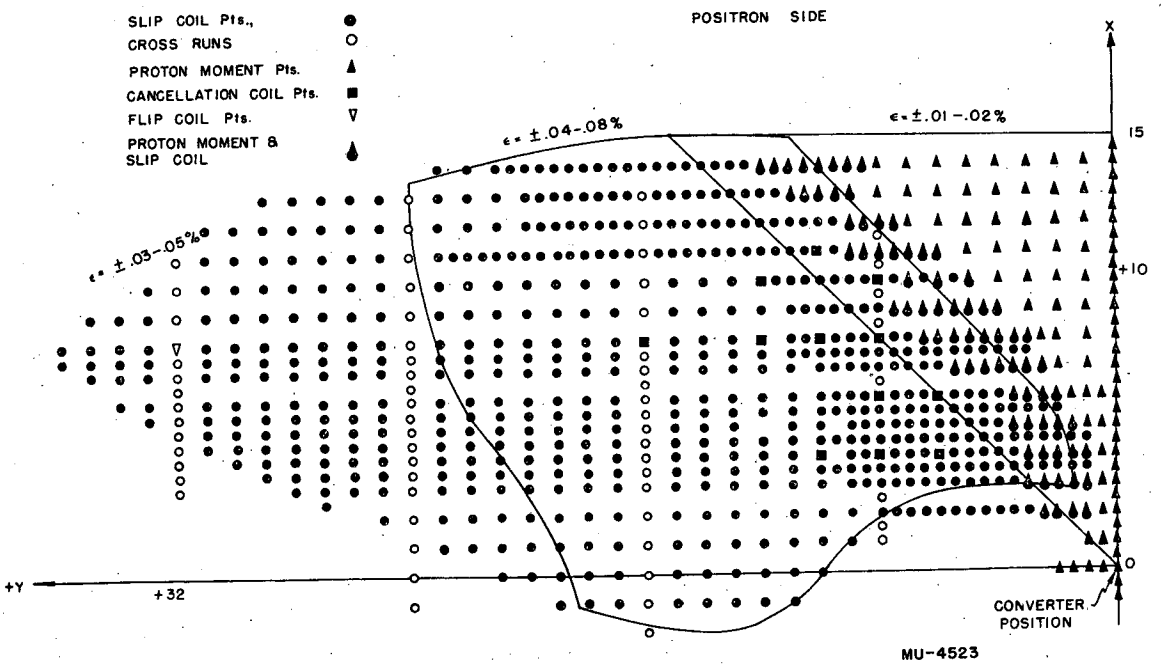
SLIP COIL Pts.,
CROSS RUNS
PROTON MOMENT Pts.
CANCELLATION COIL Pts.
FLIP COIL Pts.
PROTON MOMENT & SLIP COIL
POSITRON SIDE
X
ε = ± .04-.08%
ε = ± .01 - .02%
ε = ± .03-.05%
15
+10
0
+Y
+32
CONVERTER POSITION
MU-4523

Fig. 32

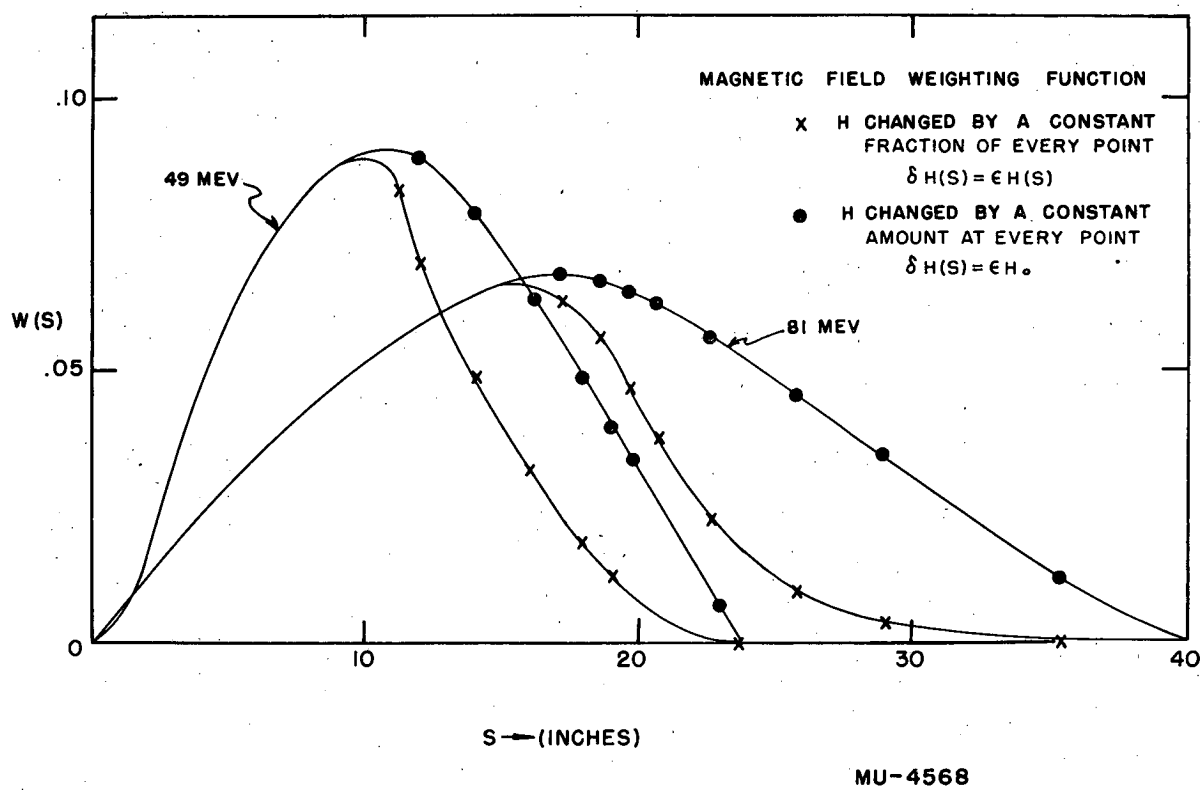
MAGNETIC FIELD WEIGHTING FUNCTION
X H CHANGED BY A CONSTANT FRACTION OF EVERY POINT
δ H(S) = ε H(S)
● H CHANGED BY A CONSTANT AMOUNT AT EVERY POINT
δ H(S) = ε H₀
49 MEV
81 MEV
W(S)
.10
.05
0
10
20
30
40
S → (INCHES)
MU-4568

Fig. 33

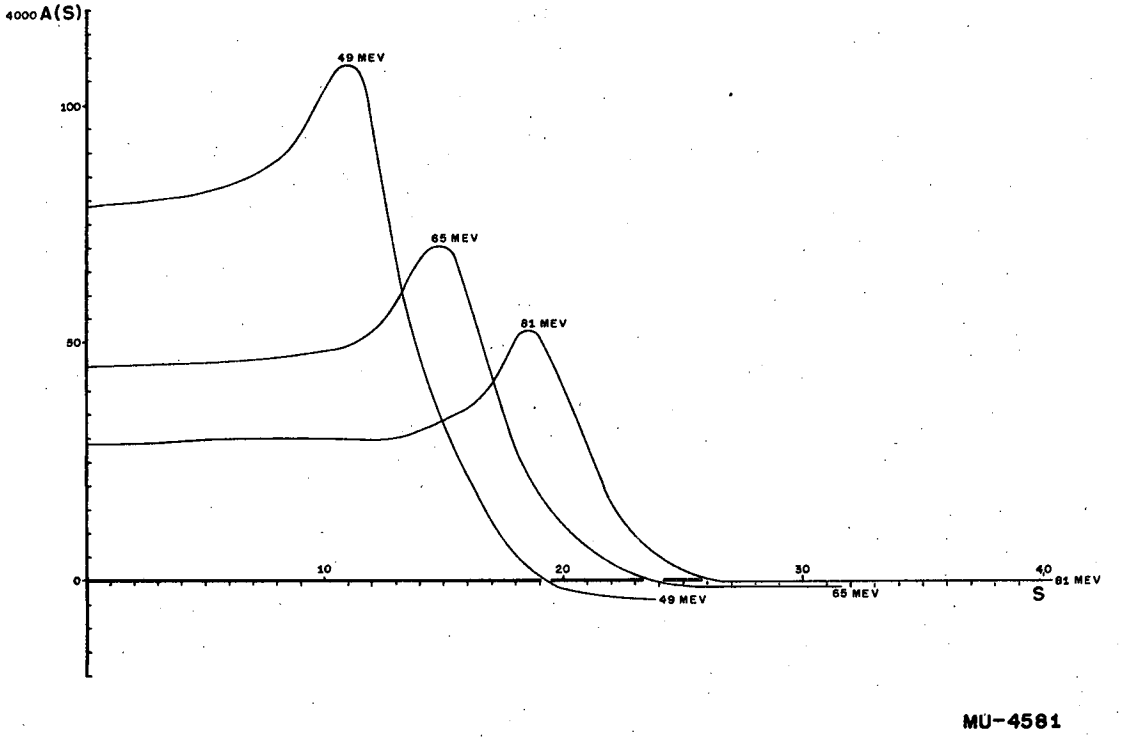
4000 A(S)
100
50
0
49 MEV
65 MEV
81 MEV
10
20
30
40
49 MEV
65 MEV
81 MEV
S
MU-4581

Fig. 34

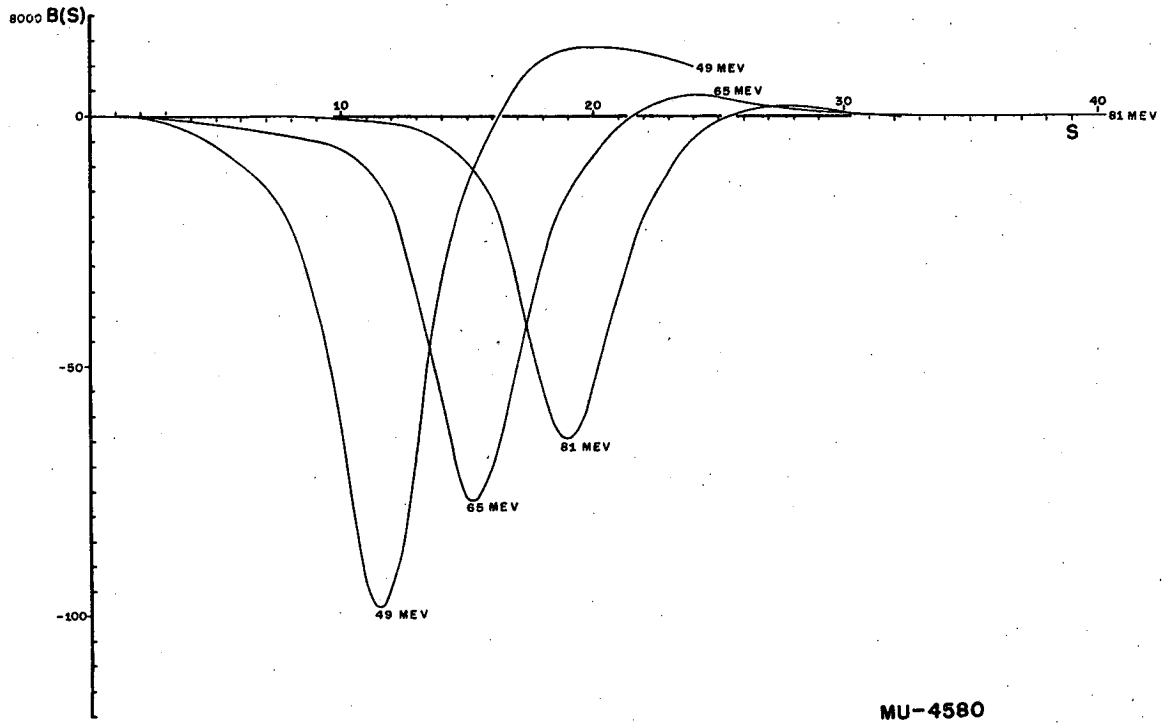
8000 B(S)
0
-50
-100
10
20
30
40
S
49 MEV
65 MEV
81 MEV
49 MEV
65 MEV
81 MEV
MU-4580

Fig. 35

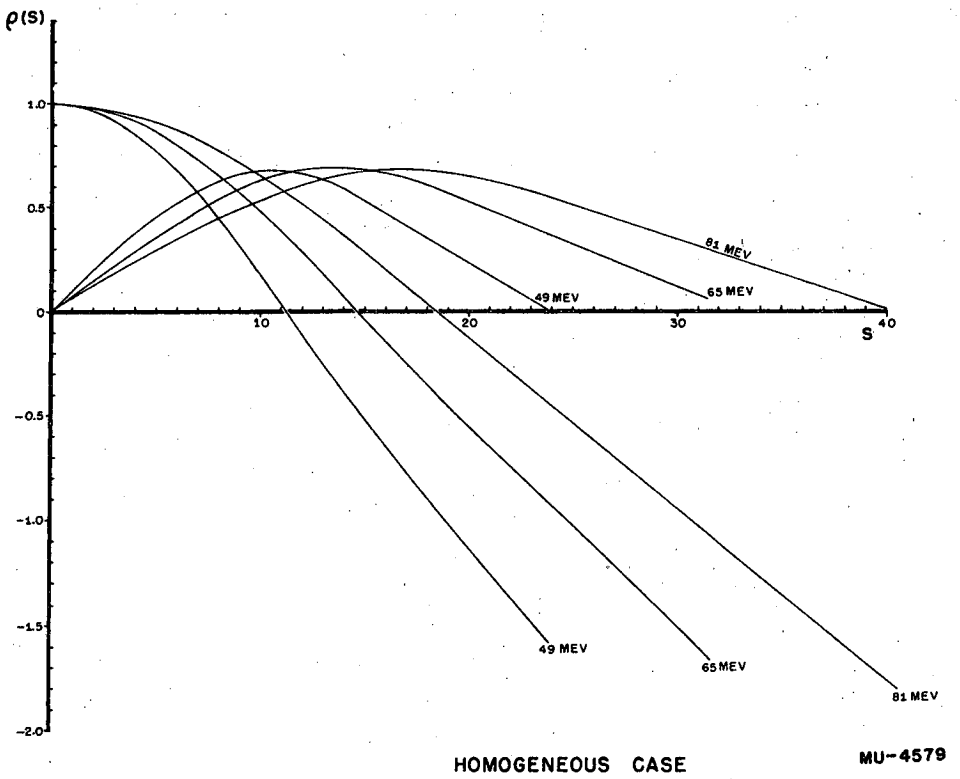
ρ(S)
1.0
0.5
0
-0.5
-1.0
-1.5
-2.0
10
20
30
40
S
81 MEV
65 MEV
49 MEV
49 MEV
65 MEV
81 MEV
HOMOGENEOUS CASE
MU-4579

Fig. 36

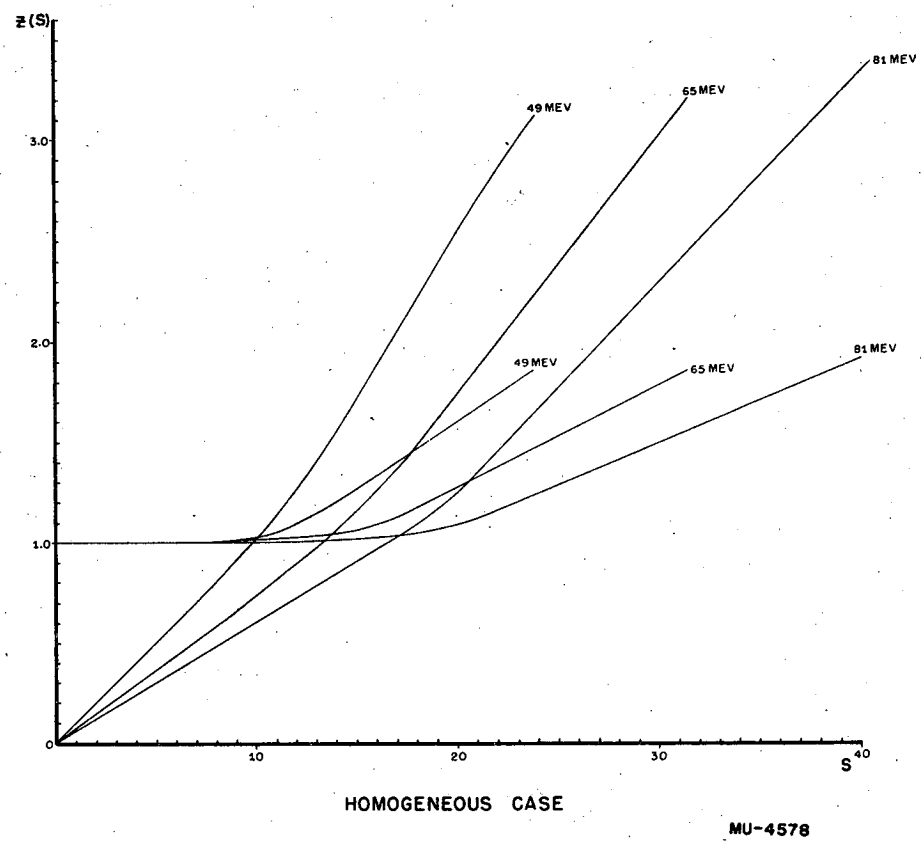
z(S)
3.0
2.0
1.0
0
10
20
30
40
S
49 MEV
65 MEV
81 MEV
49 MEV
65 MEV
81 MEV
HOMOGENEOUS CASE
MU-4578

Fig. 37

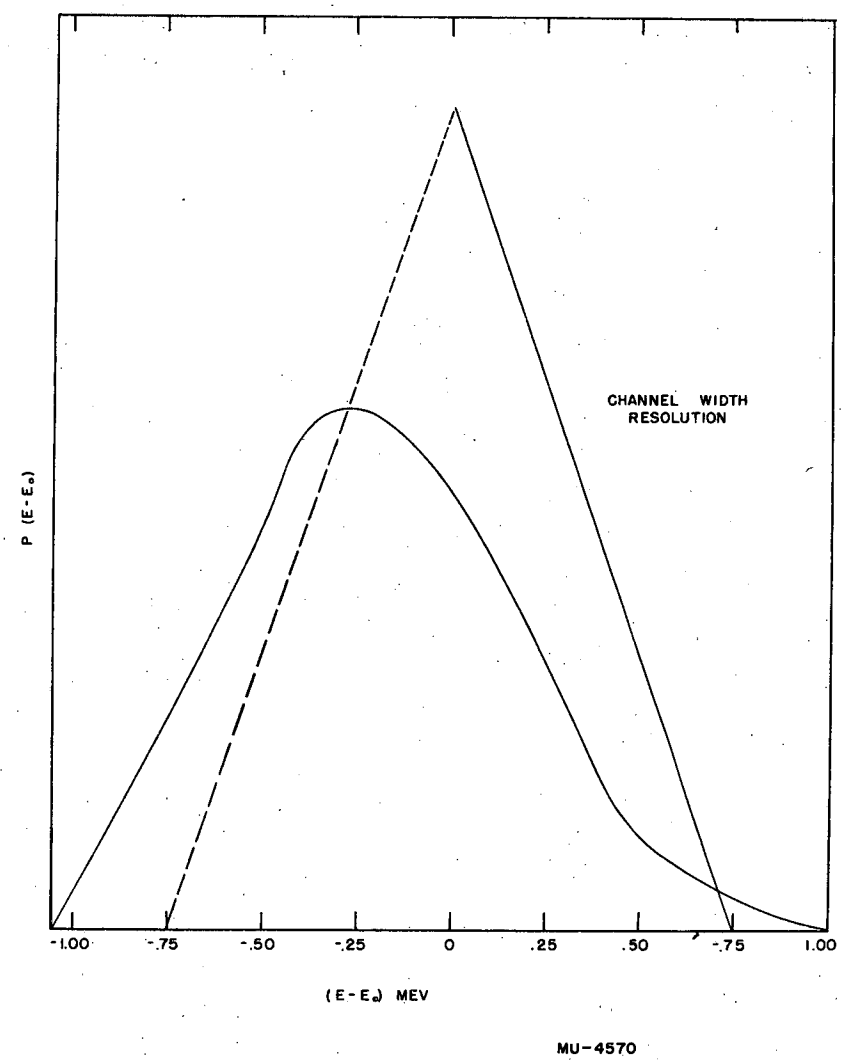
CHANNEL WIDTH
RESOLUTION
P (E-E₀)
-1.00
-.75
-.50
-.25
0
.25
.50
.75
1.00
(E-E₀) MEV
MU-4570

Fig. 38

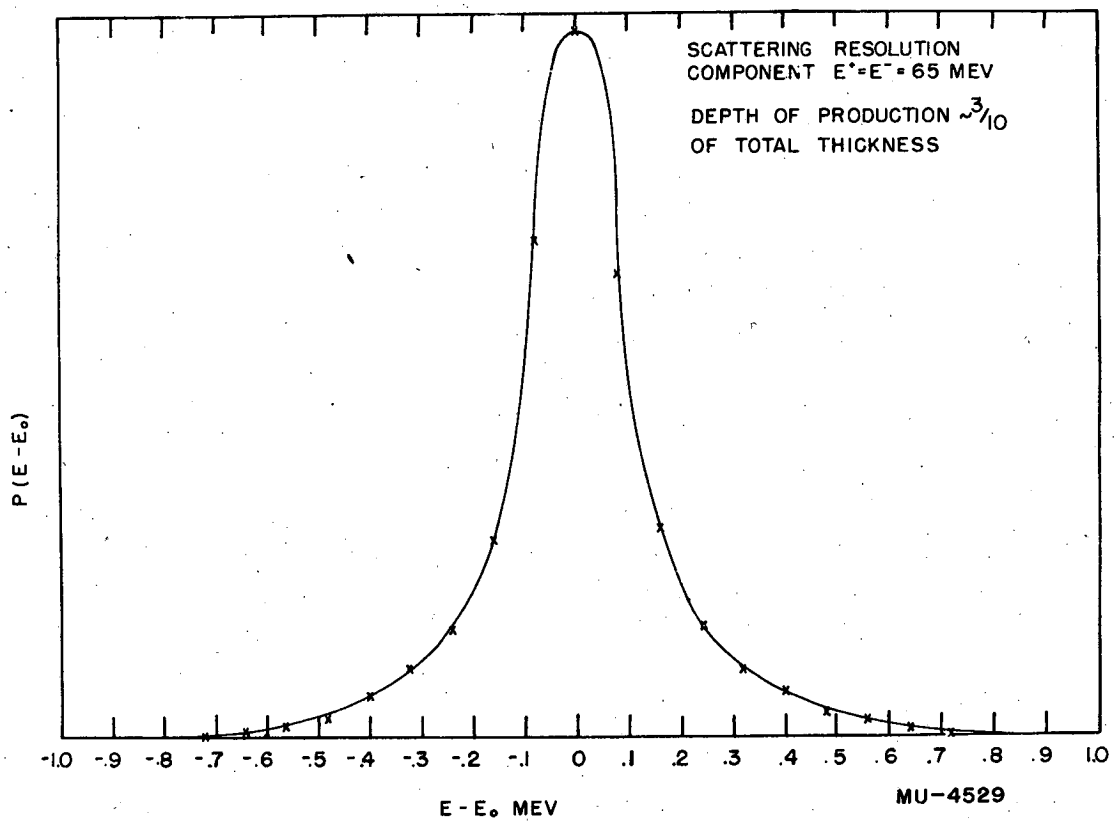
SCATTERING RESOLUTION
COMPONENT E⁺=E⁻=65 MEV
DEPTH OF PRODUCTION ~3/10
OF TOTAL THICKNESS
P(E-E₀)
-1.0 -.9 -.8 -.7 -.6 -.5 -.4 -.3 -.2 -.1 0 .1 .2 .3 .4 .5 .6 .7 .8 .9 1.0
E-E₀ MEV
MU-4529

Fig. 39

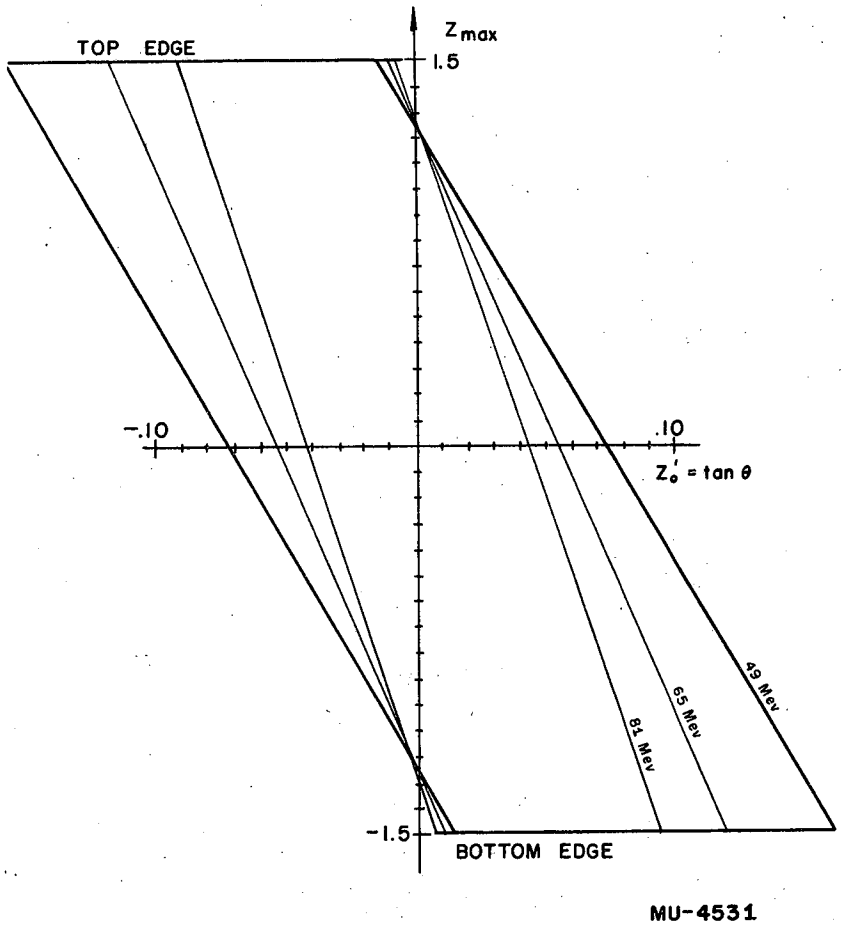
TOP EDGE
Z_{max}
1.5
-.10
.10
$Z_o' = \tan\theta$
49 Mev
65 Mev
81 Mev
-1.5
BOTTOM EDGE
MU-4531

Fig. 40

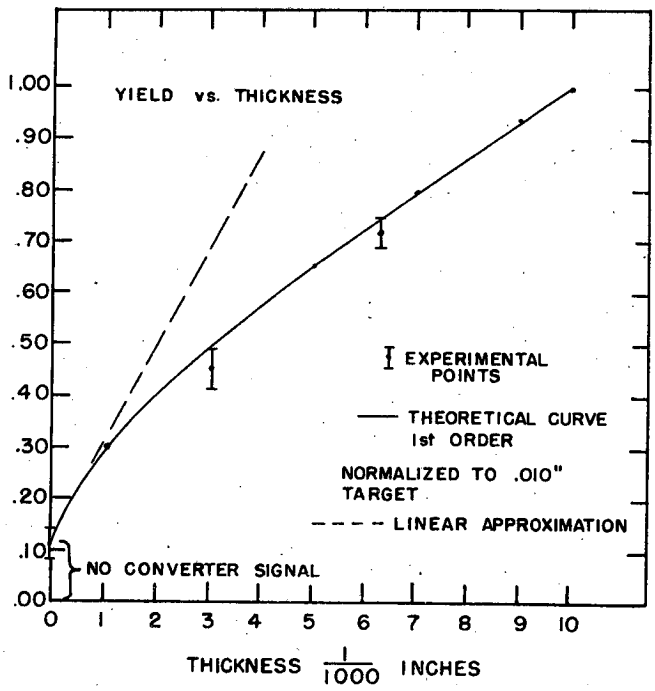
YIELD vs. THICKNESS
1.00
.90
.80
.70
.60
.50
.40
.30
.20
.10
.00
0 1 2 3 4 5 6 7 8 9 10
EXPERIMENTAL POINTS
THEORETICAL CURVE 1st ORDER
NORMALIZED TO .010" TARGET
LINEAR APPROXIMATION
NO CONVERTER SIGNAL
THICKNESS 1/1000 INCHES
MU-4544

Fig. 41

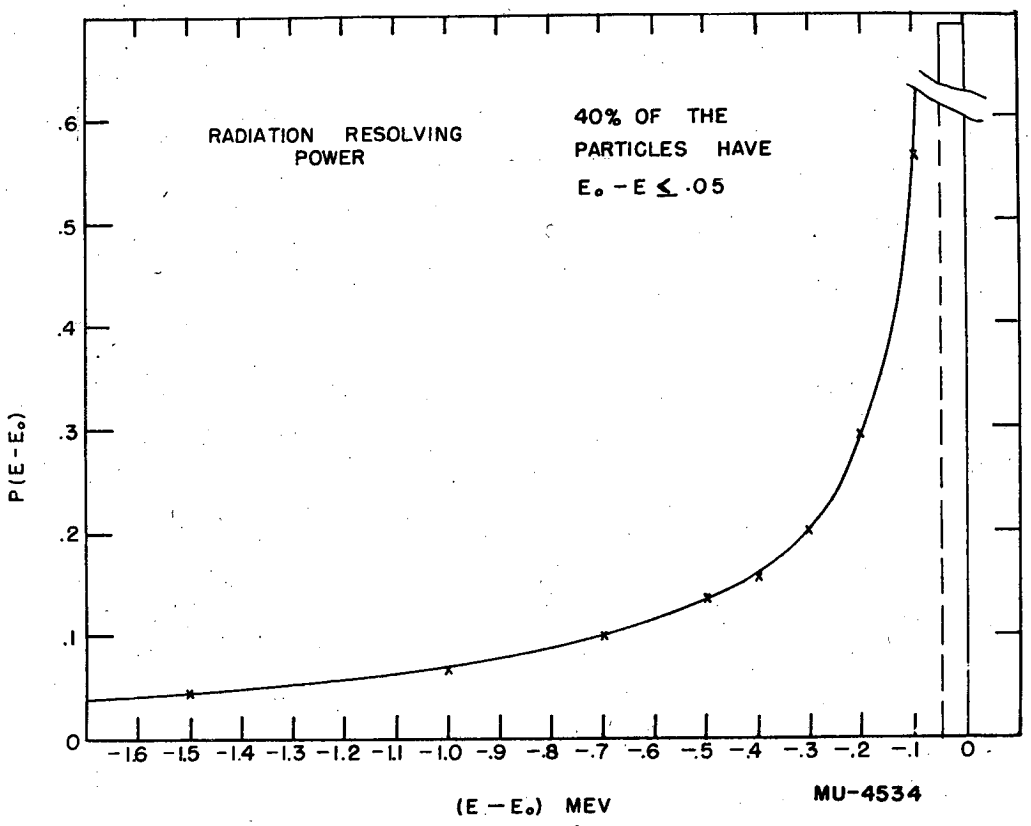
RADIATION RESOLVING POWER
40% OF THE PARTICLES HAVE
E₀ - E ≤ .05
P(E - E₀)
.6
.5
.4
.3
.2
.1
0
-1.6 -1.5 -1.4 -1.3 -1.2 -1.1 -1.0 -.9 -.8 -.7 -.6 -.5 -.4 -.3 -.2 -.1 0
(E - E₀) MEV
MU-4534

Fig. 42

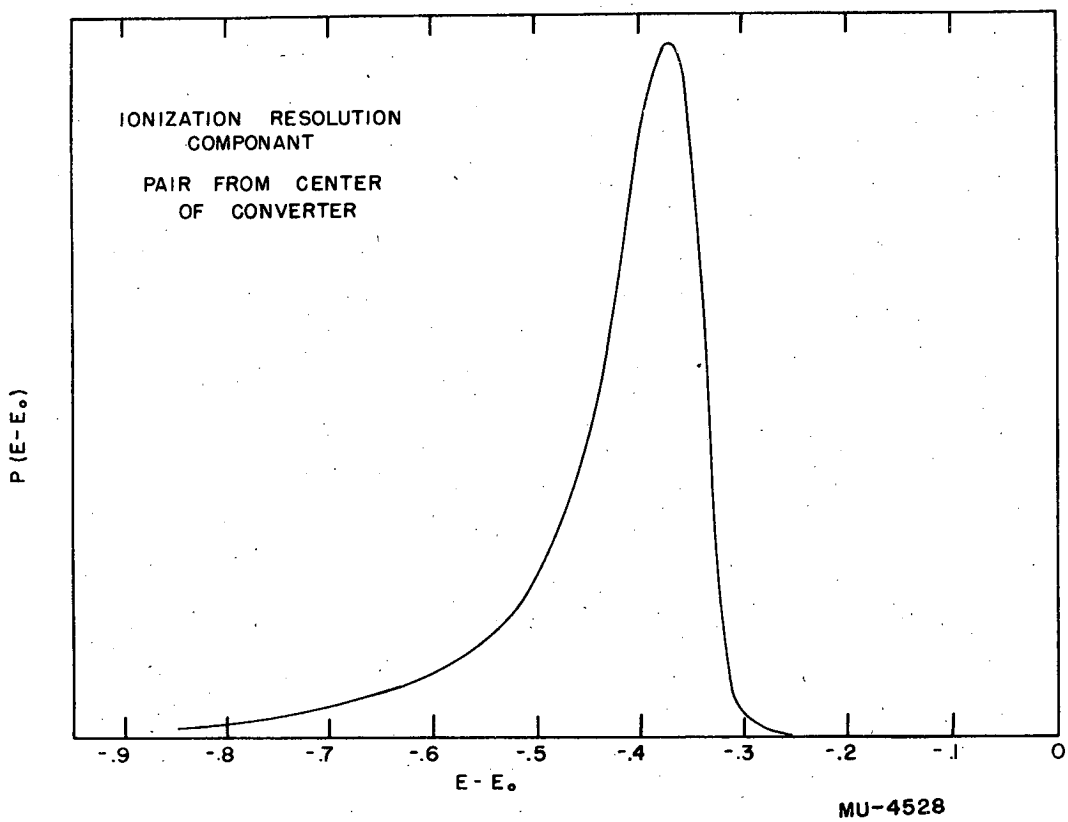
IONIZATION RESOLUTION
COMPONANT
PAIR FROM CENTER
OF CONVERTER
P (E - E₀)
-.9
-.8
-.7
-.6
-.5
-.4
-.3
-.2
-.1
0
E - E₀
MU-4528

Fig. 43

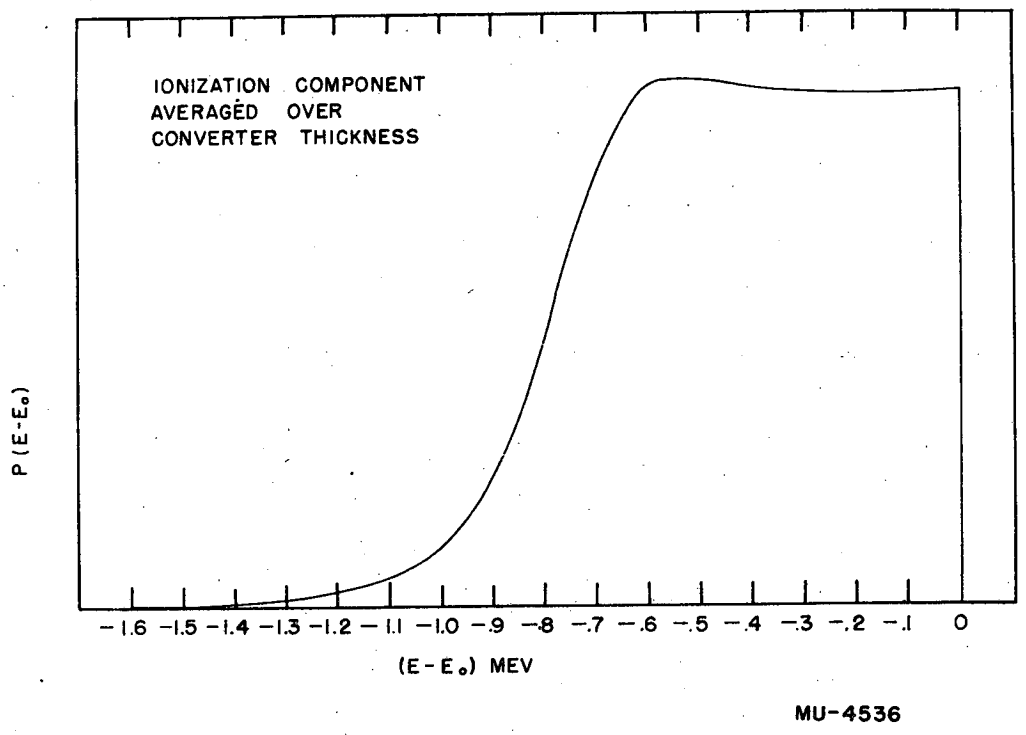
IONIZATION COMPONENT
AVERAGED OVER
CONVERTER THICKNESS
P (E-E₀)
-1.6 -1.5 -1.4 -1.3 -1.2 -1.1 -1.0 -.9 -.8 -.7 -.6 -.5 -.4 -.3 -.2 -.1 0
(E-E₀) MEV
MU-4536

Fig. 44

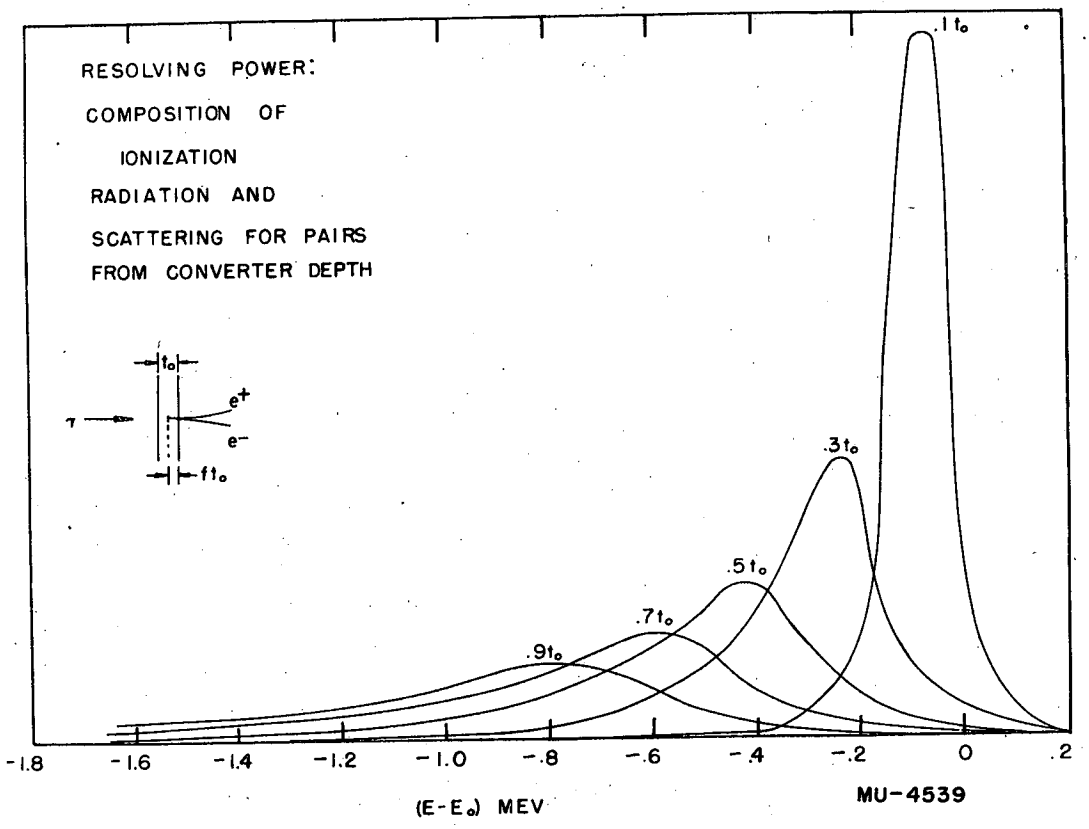
RESOLVING POWER:
COMPOSITION OF
IONIZATION
RADIATION AND
SCATTERING FOR PAIRS
FROM CONVERTER DEPTH
t_o
e^+
γ
e^-
ft_o
$.1t_o$
$.3t_o$
$.5t_o$
$.7t_o$
$.9t_o$
-1.8
-1.6
-1.4
-1.2
-1.0
-.8
-.6
-.4
-.2
0
.2
$(E-E_o)$ MEV
MU-4539

Fig. 45

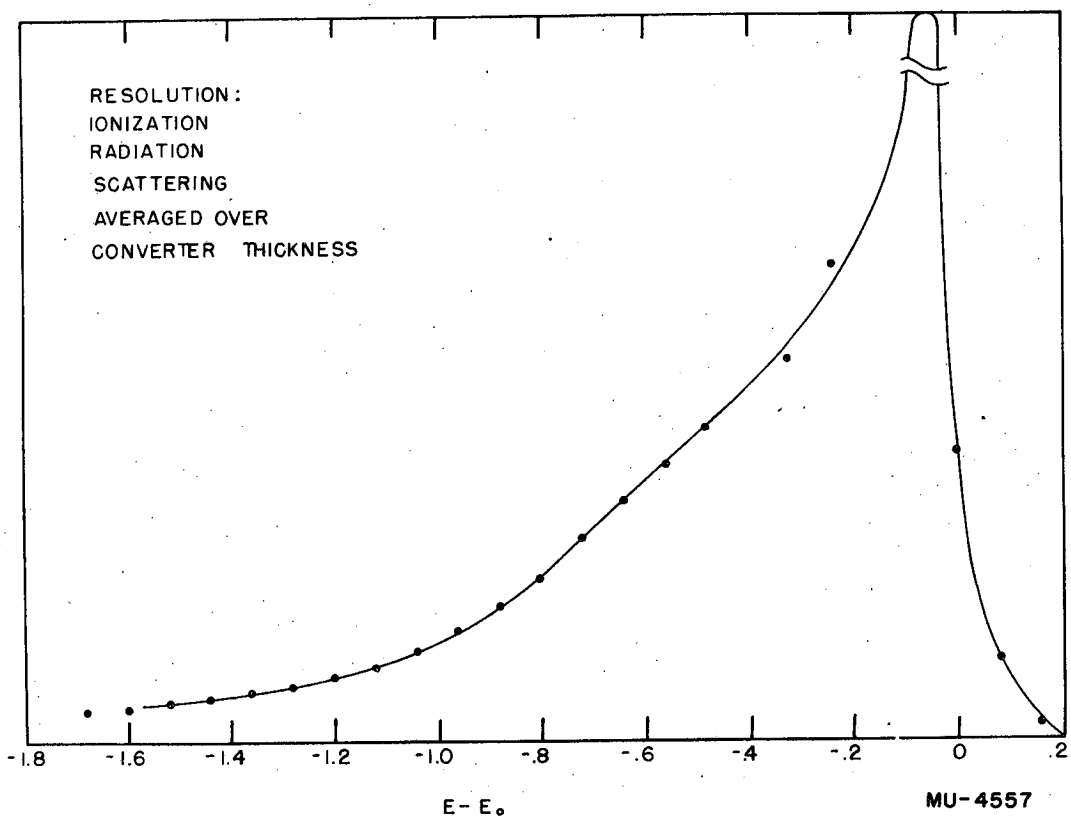
RESOLUTION:
IONIZATION
RADIATION
SCATTERING
AVERAGED OVER
CONVERTER THICKNESS
-1.8
-1.6
-1.4
-1.2
-1.0
-.8
-.6
-.4
-.2
0
.2
E - E₀
MU-4557

Fig. 46

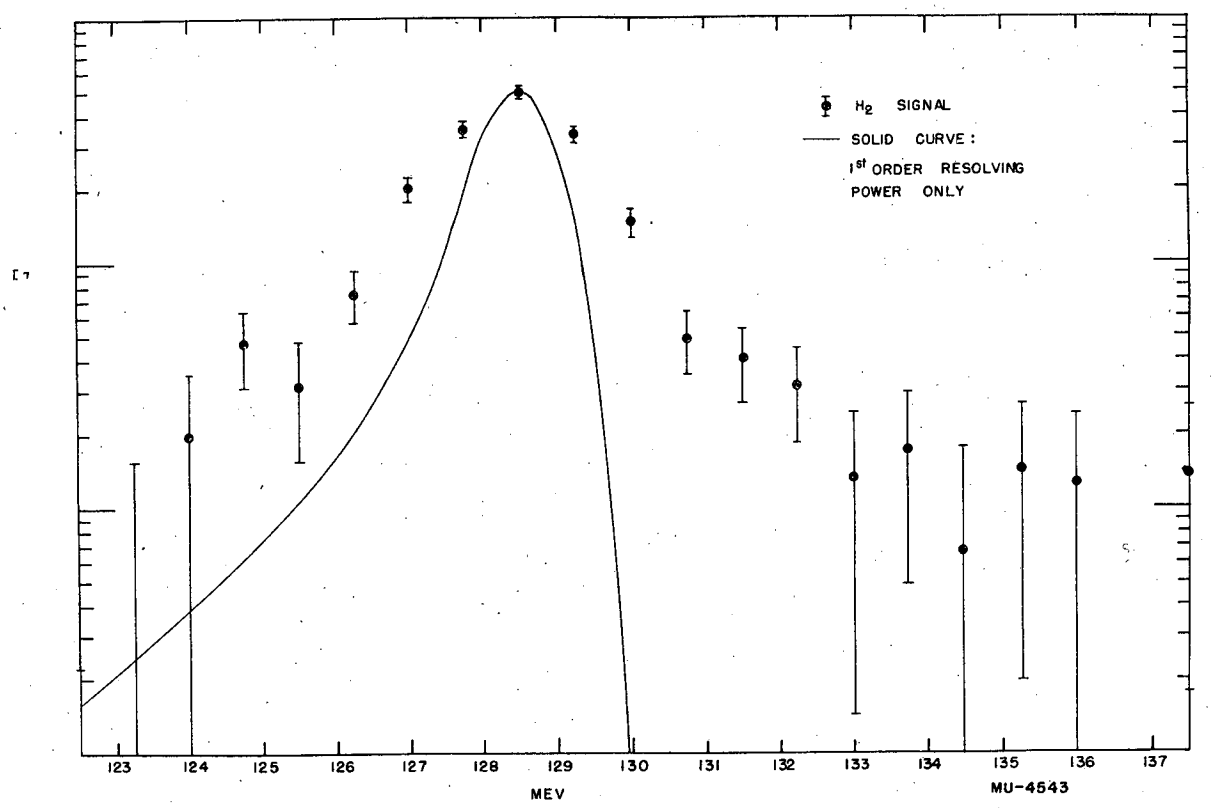
H_2 SIGNAL
SOLID CURVE :
1st ORDER RESOLVING POWER ONLY
123
124
125
126
127
128
129
130
131
132
133
134
135
136
137
MEV
MU-4543

Fig. 47

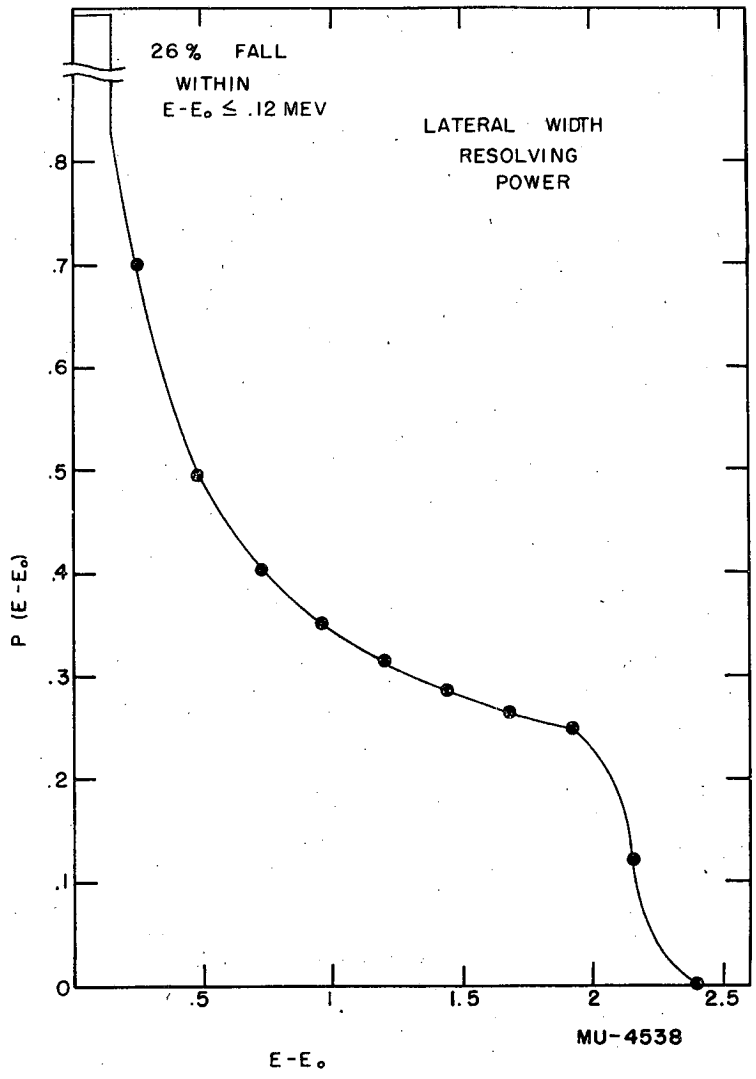
26 % FALL
WITHIN
E-E₀ ≤ .12 MEV
LATERAL WIDTH
RESOLVING
POWER
P (E-E₀)
0
.1
.2
.3
.4
.5
.6
.7
.8
.5
1
1.5
2
2.5
E-E₀
MU-4538

Fig. 48

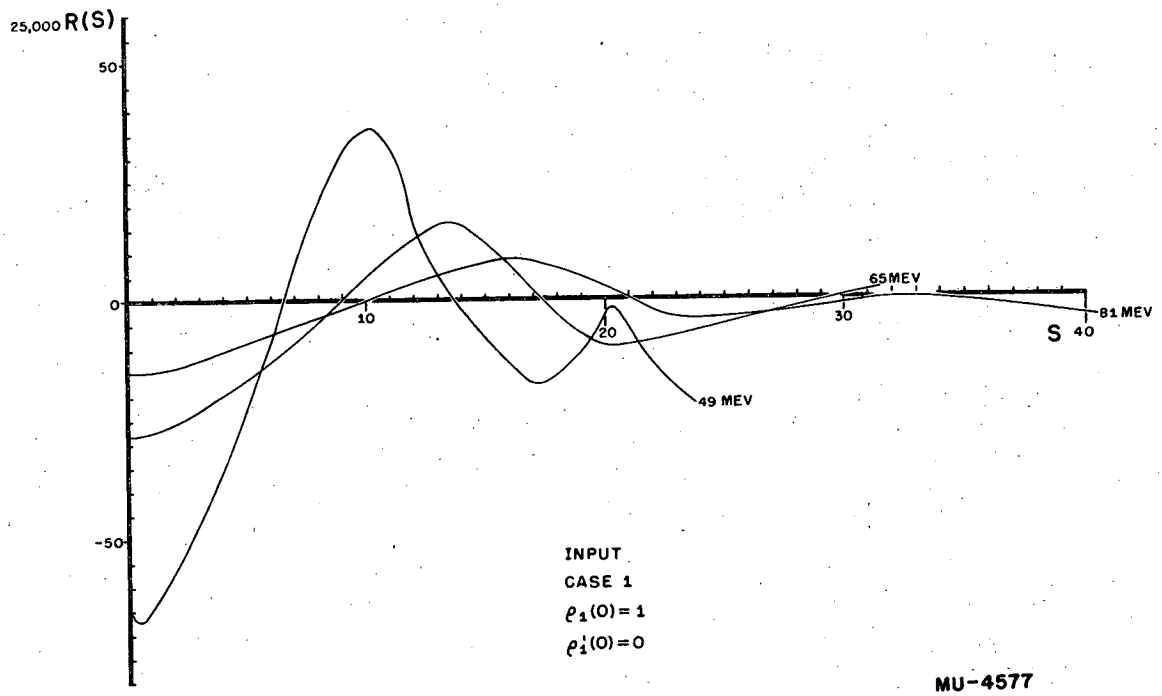
25,000 R(S)
50
0
-50
10
20
30
40
S
65 MEV
81 MEV
49 MEV
INPUT
CASE 1
$\rho_1(0) = 1$
$\rho_1'(0) = 0$
MU-4577

Fig. 49

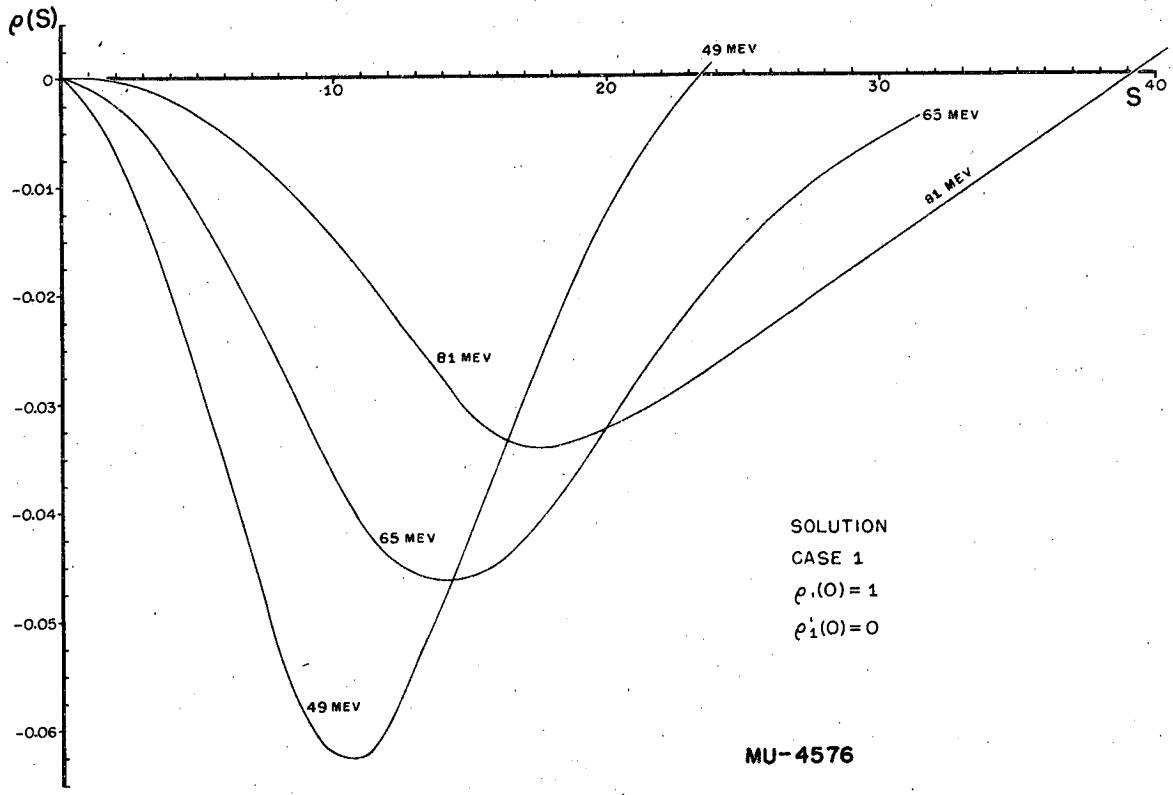
ρ(S)
0
-0.01
-0.02
-0.03
-0.04
-0.05
-0.06
10
20
30
40
S
49 MEV
65 MEV
81 MEV
81 MEV
65 MEV
49 MEV
SOLUTION
CASE 1
ρ1(0) = 1
ρ'1(0) = 0
MU-4576

Fig. 50

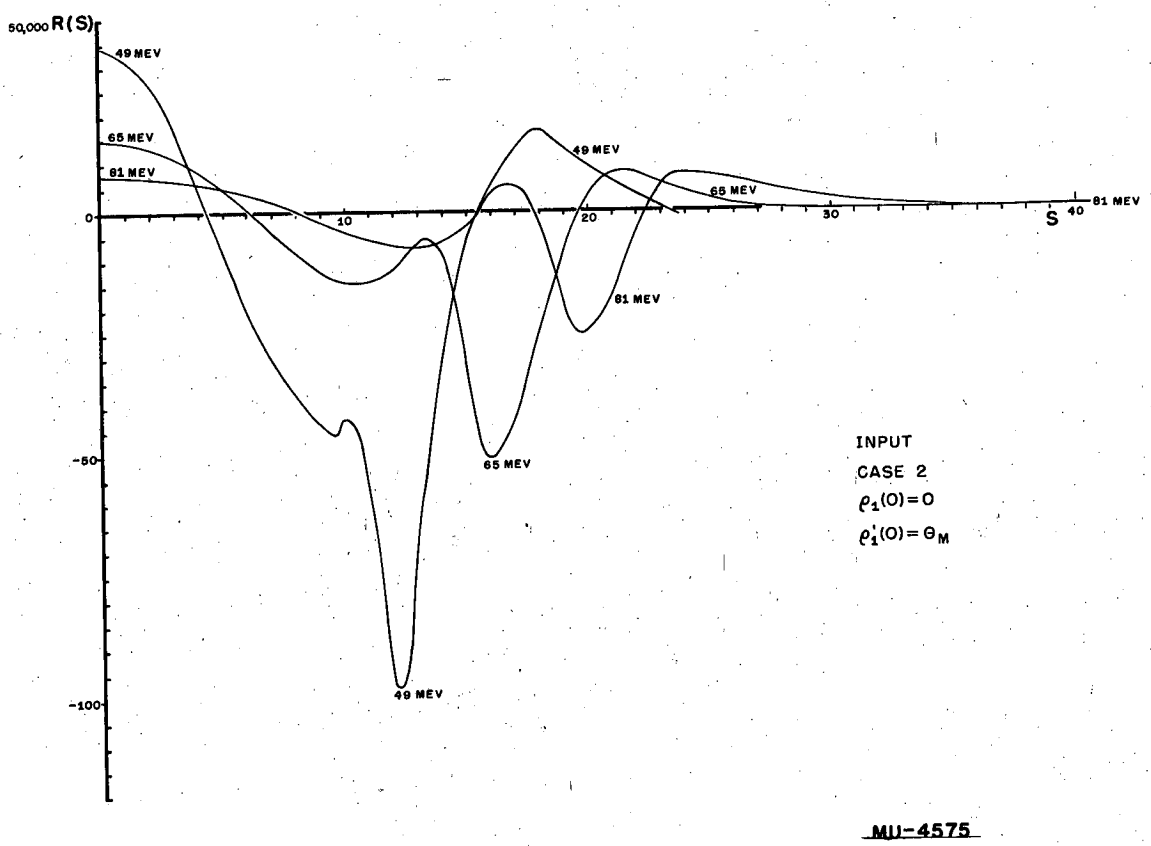
50,000 R(S)
49 MEV
65 MEV
81 MEV
0
10
20
30
40
S
81 MEV
49 MEV
65 MEV
81 MEV
65 MEV
-50
-100
49 MEV
INPUT
CASE 2
$\rho_1(0)=0$
$\rho_1'(0)=\Theta_M$
MU-4575

Fig. 51

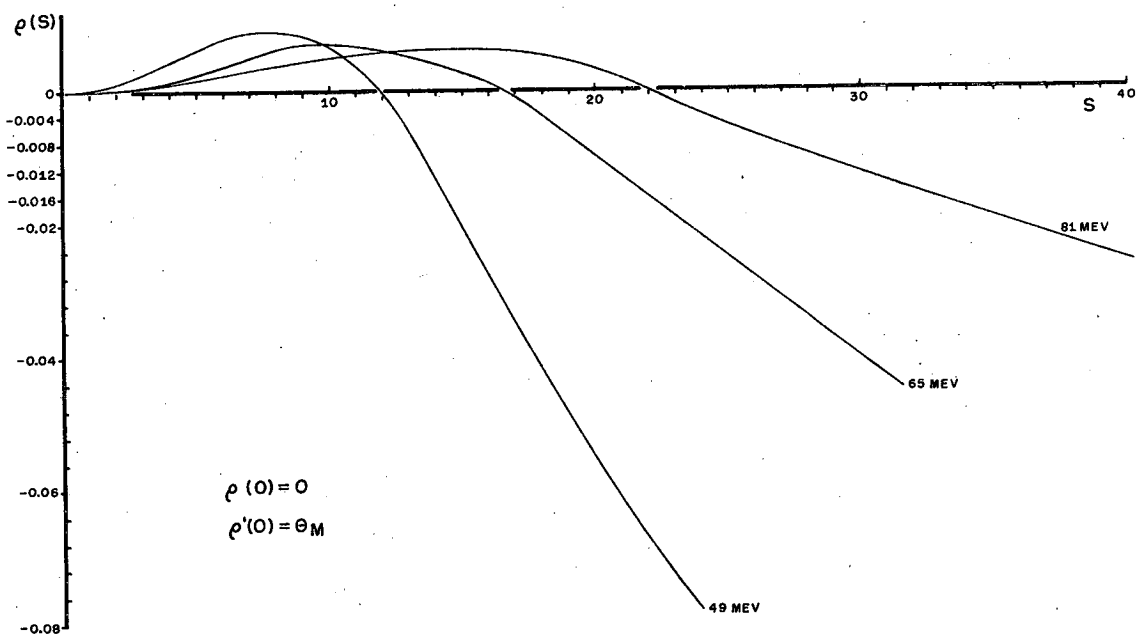

CASE II

MU-4594

Fig. 52

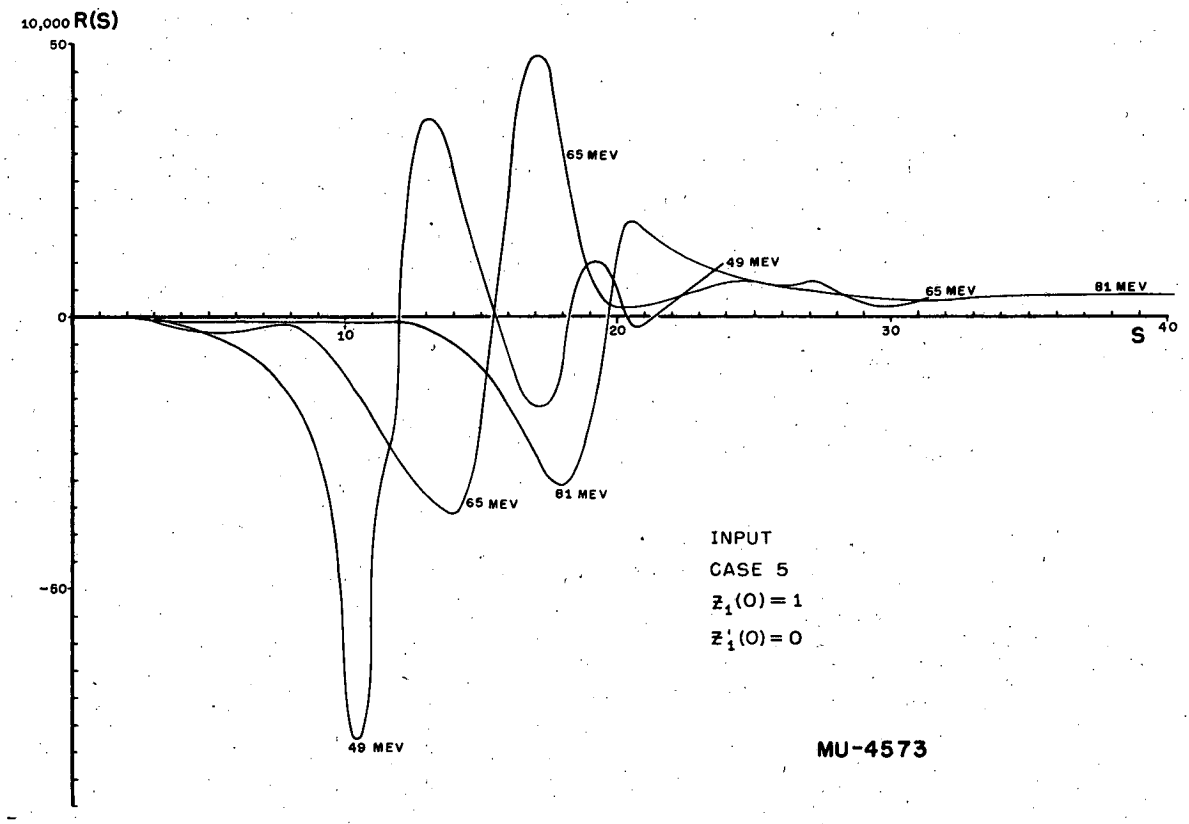
10,000 R(S)
50
0
-50
10
20
30
40
S
65 MEV
49 MEV
65 MEV
81 MEV
65 MEV
81 MEV
49 MEV
INPUT
CASE 5
$\bar{z}_1(0) = 1$
$\bar{z}_1'(0) = 0$
MU-4573

Fig. 53

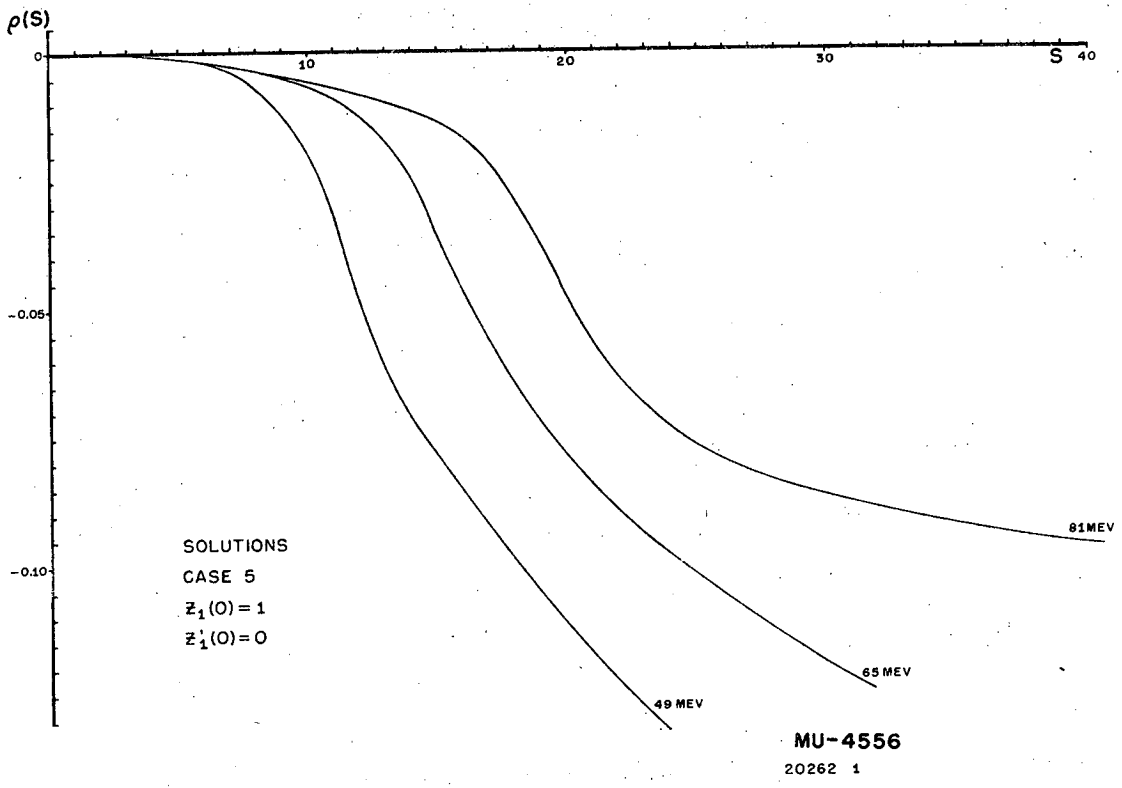
ρ(S)
0
10
20
30
S
40
-0.05
-0.10
SOLUTIONS
CASE 5
$z_1(0) = 1$
$z_1'(0) = 0$
81MEV
65 MEV
49 MEV
MU-4556
20262 1

Fig. 54

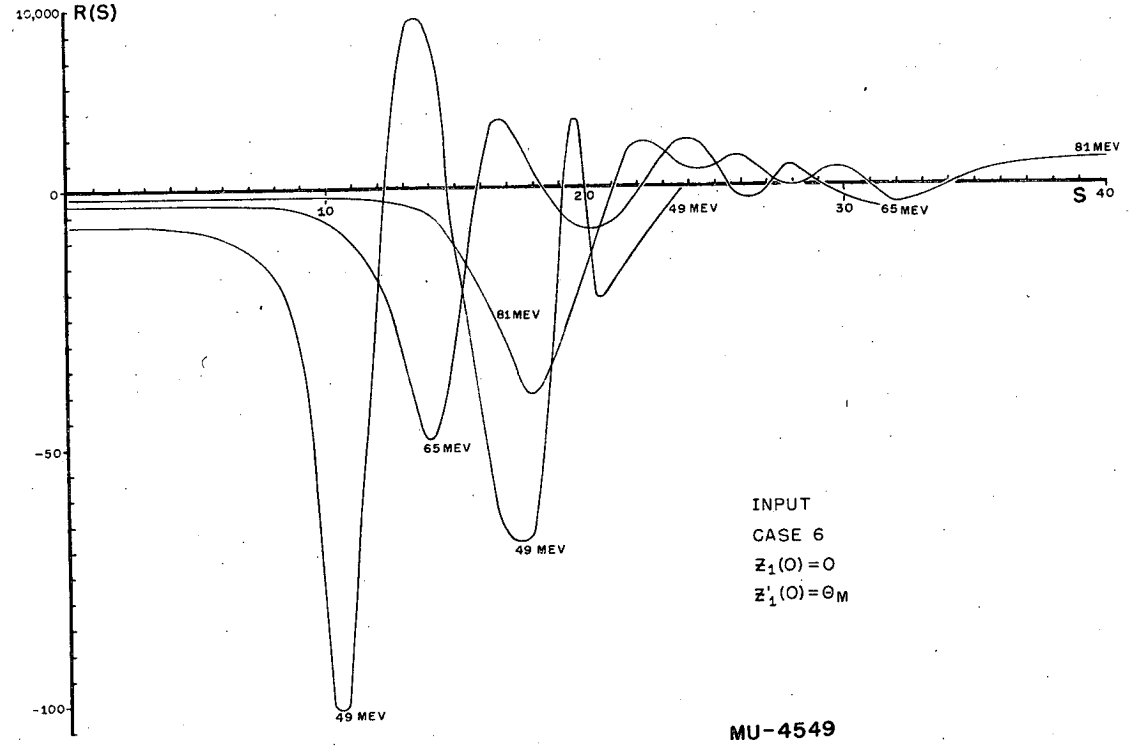
10,000
R(S)
0
-50
-100
10
20
30
S 40
81 MEV
65 MEV
49 MEV
81 MEV
65 MEV
49 MEV
INPUT
CASE 6
$z_1(0) = 0$
$z'_1(0) = \Theta_M$
MU-4549

Fig. 55

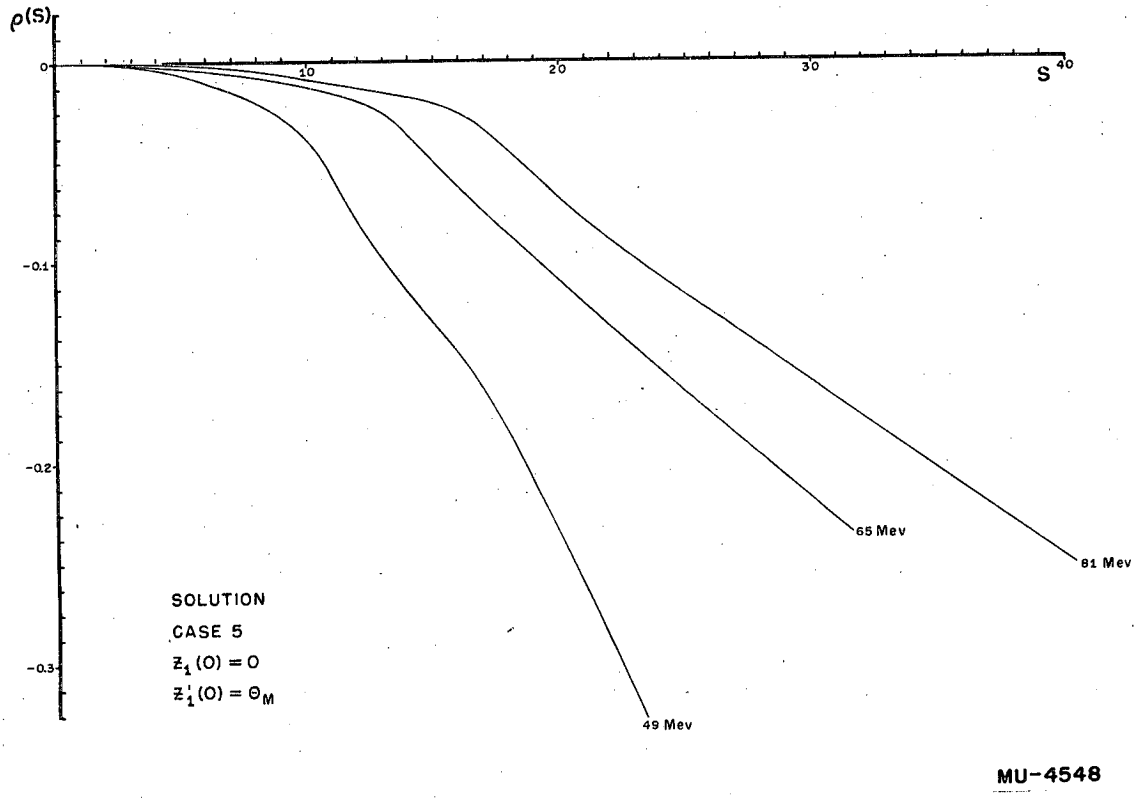
ρ(S)
0
-0.1
-0.2
-0.3
10
20
30
40
S
65 Mev
81 Mev
49 Mev
SOLUTION
CASE 5
$z_1(0) = 0$
$z_1'(0) = \Theta_M$
MU-4548

Fig. 56

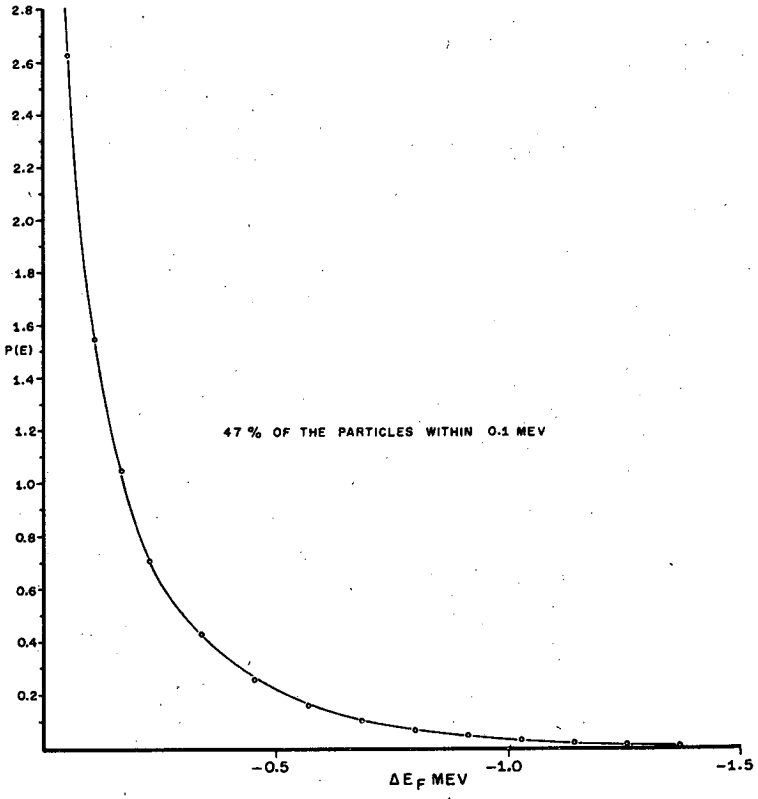

CASE 2

2nd ORDER RESOLUTION ρ' MOTION

MU-4551

Fig. 57

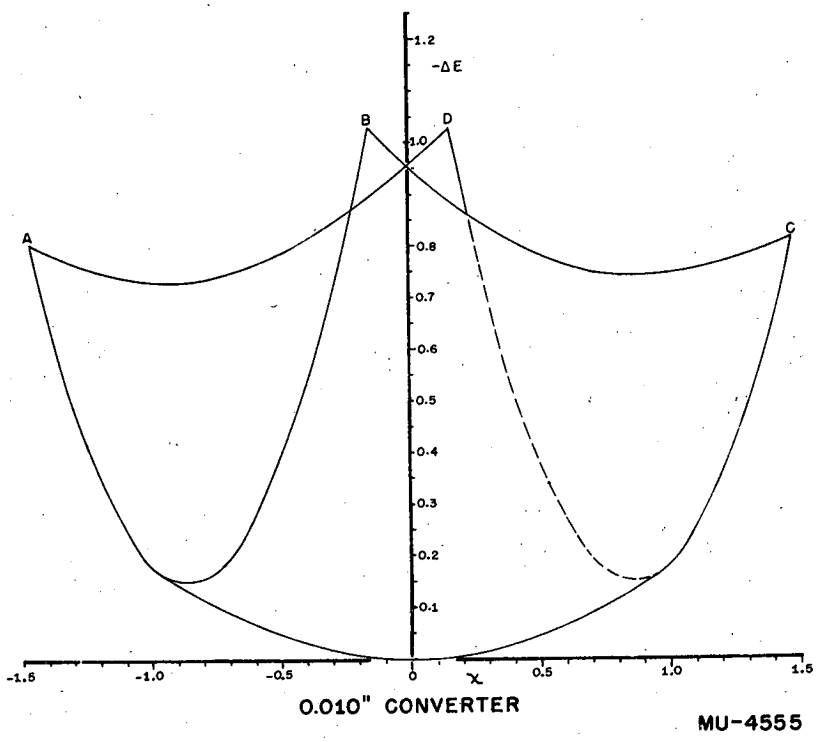
1.2
-ΔE
B
D
1.0
A
C
0.8
0.7
0.6
0.5
0.4
0.3
0.2
0.1
-1.5
-1.0
-0.5
0
X
0.5
1.0
1.5
0.010" CONVERTER
MU-4555

Fig. 58

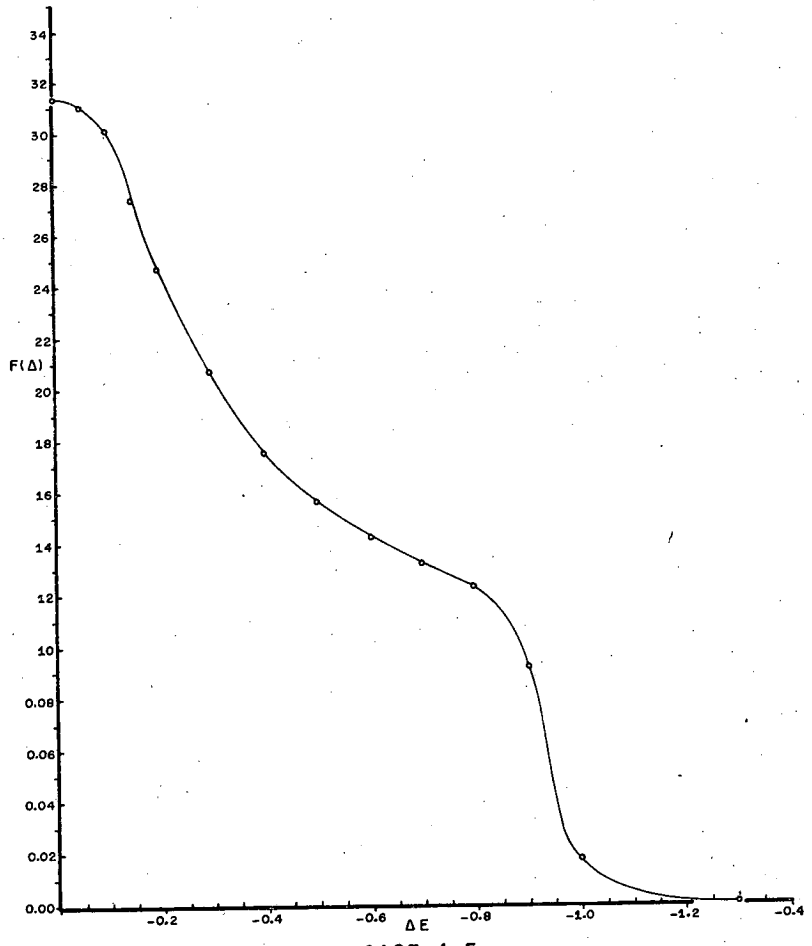
34
32
30
28
26
24
22
F(Δ)
20
18
16
14
12
10
0.08
0.06
0.04
0.02
0.00
-0.2
-0.4
-0.6
ΔE
-0.8
-1.0
-1.2
-0.4
CASE 4,5
2nd ORDER RESOLUTION Z MOTION
MU-4553

Fig. 59

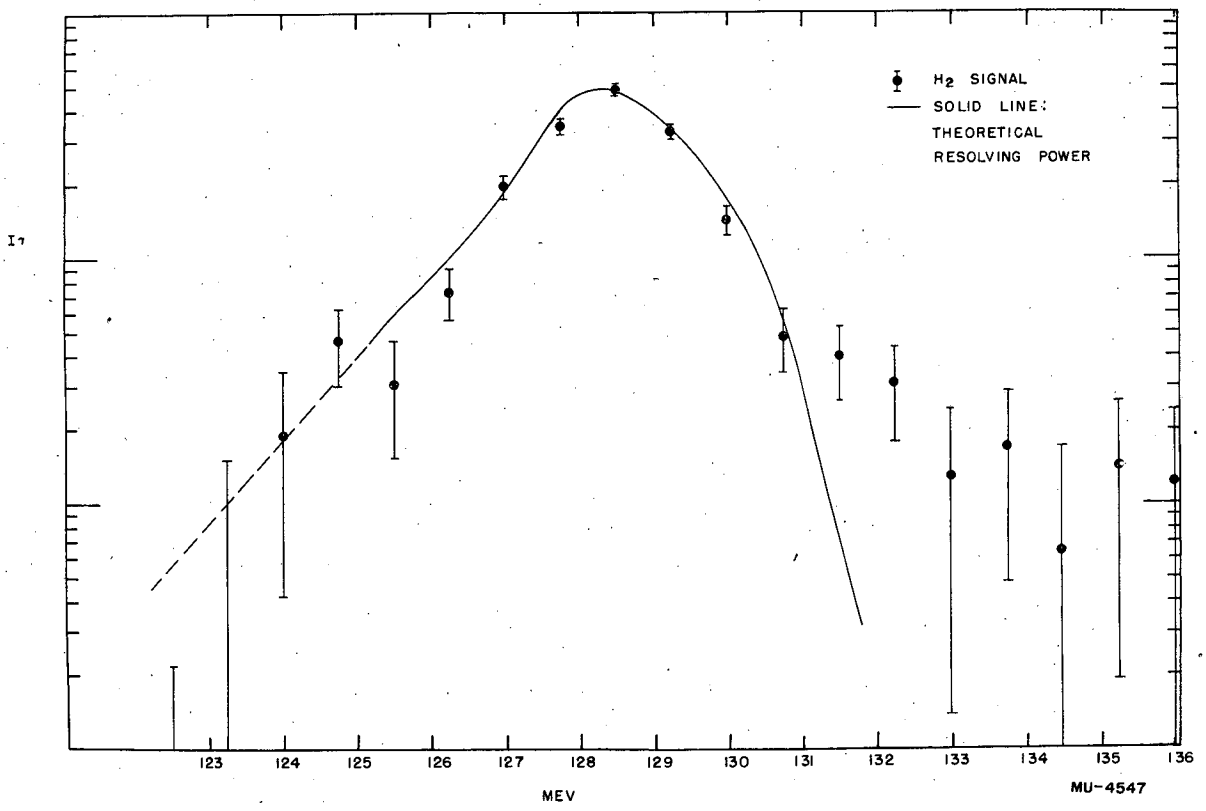
H_2 SIGNAL
SOLID LINE:
THEORETICAL
RESOLVING POWER
123
124
125
126
127
128
129
130
131
132
133
134
135
136
MEV
MU-4547

Fig. 60

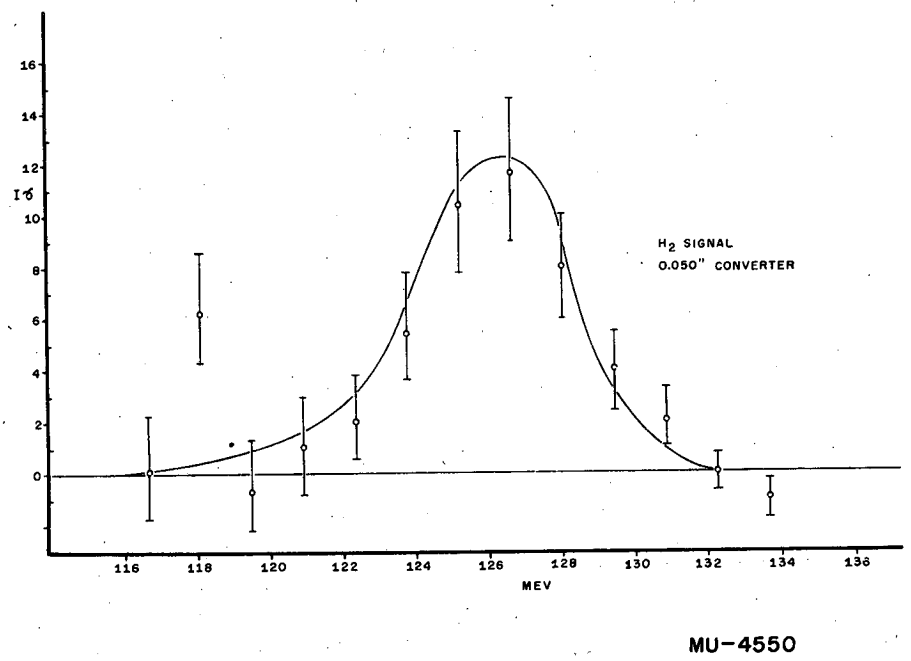
16
14
12
Iσ
10
8
6
4
2
0
116
118
120
122
124
126
128
130
132
134
136
MEV
H2 SIGNAL
0.050" CONVERTER
MU-4550

Fig. 61

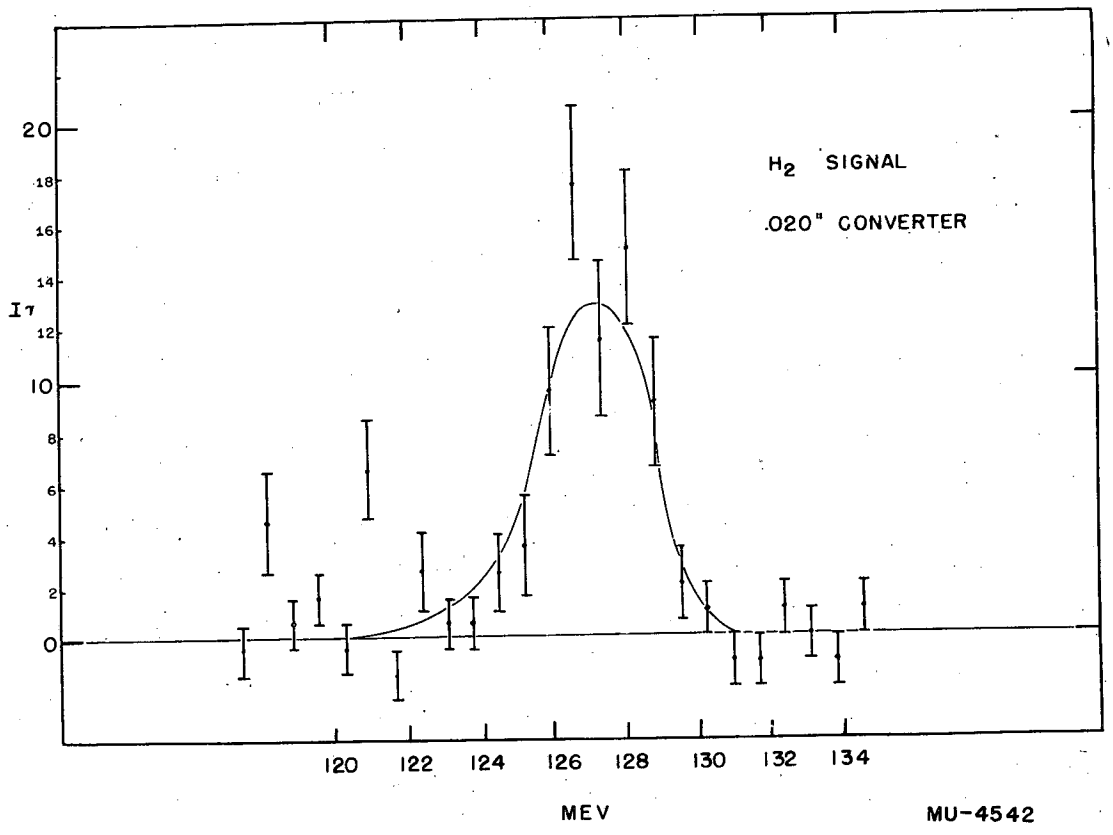
H_2 SIGNAL
.020" CONVERTER
I_7
20
18
16
14
12
10
8
6
4
2
0
120
122
124
126
128
130
132
134
MEV
MU-4542

Fig. 62

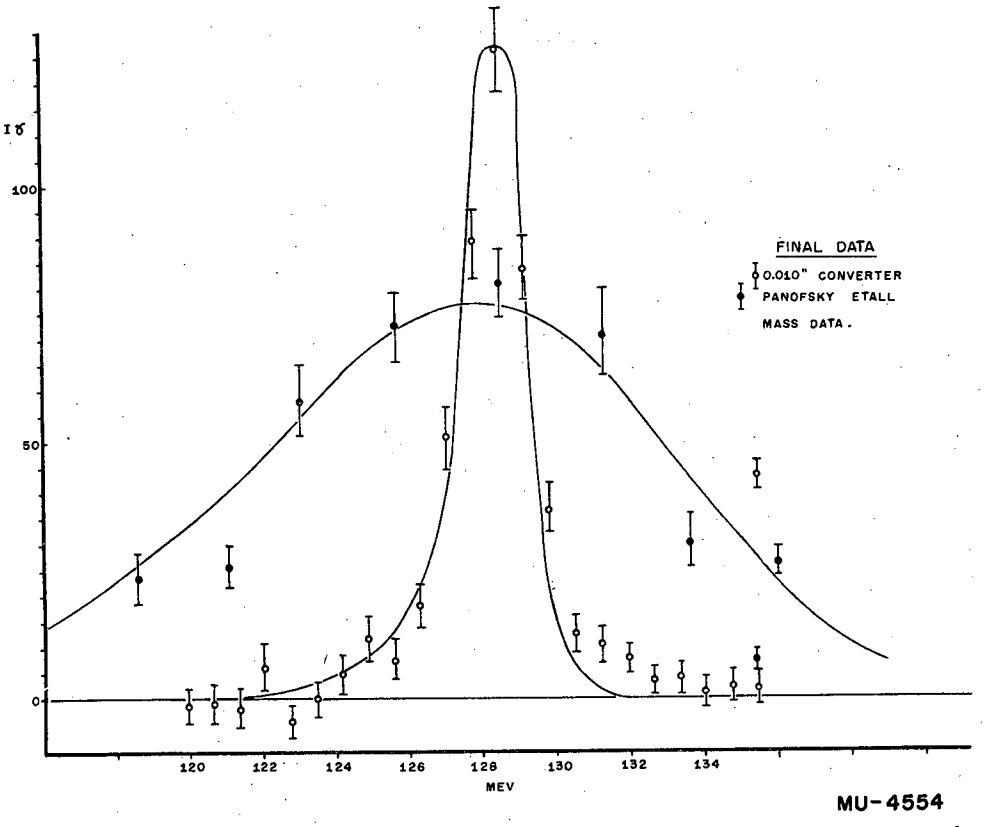
Iδ
100
50
0
120
122
124
126
128
130
132
134
MEV
FINAL DATA
0.010" CONVERTER
PANOFSKY ETALL
MASS DATA.
MU-4554

Fig. 63

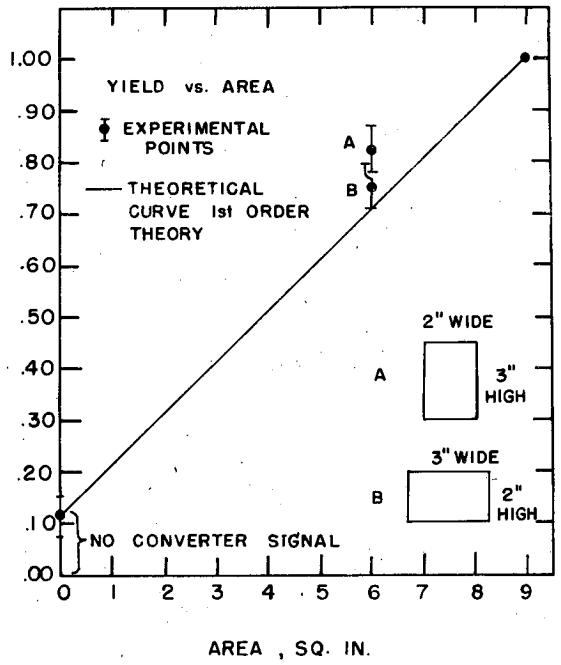

MU-4545

Fig. 64

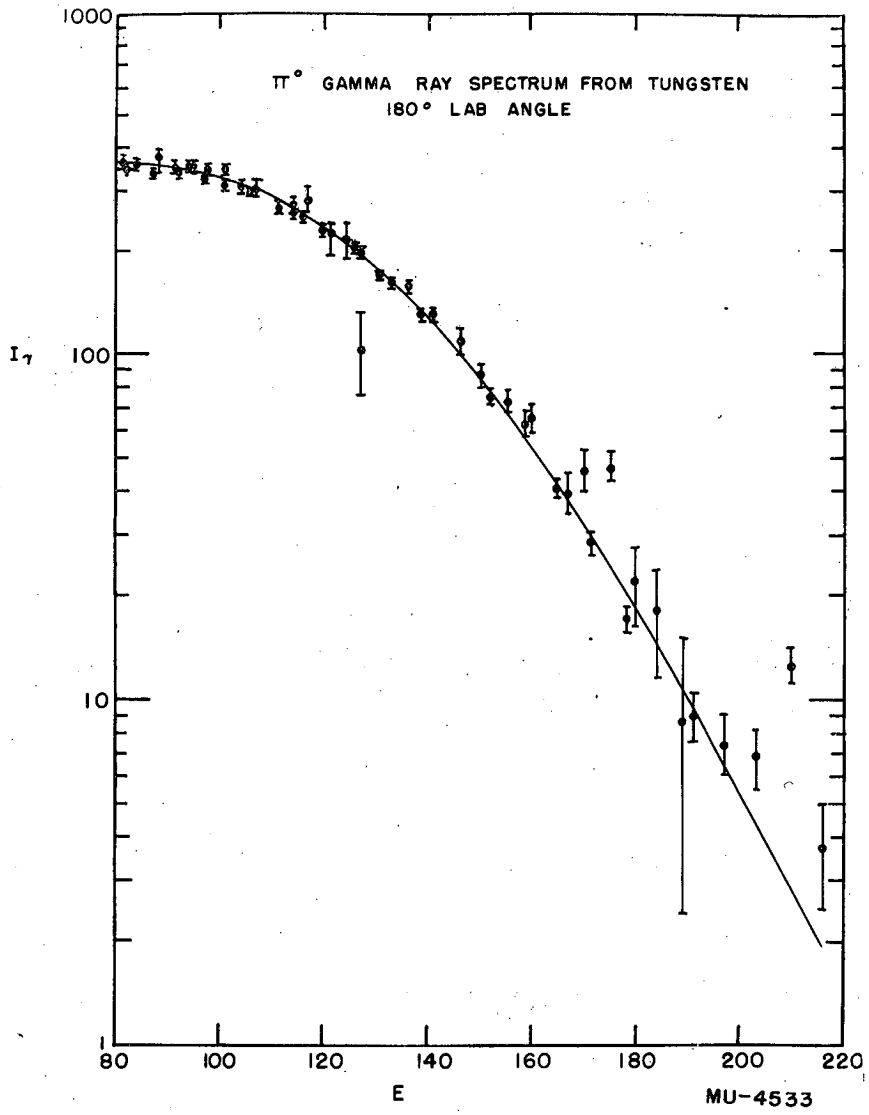
1000
100
10
1
I_γ
π° GAMMA RAY SPECTRUM FROM TUNGSTEN
180° LAB ANGLE
80
100
120
140
160
180
200
220
E
MU-4533

Fig. 65

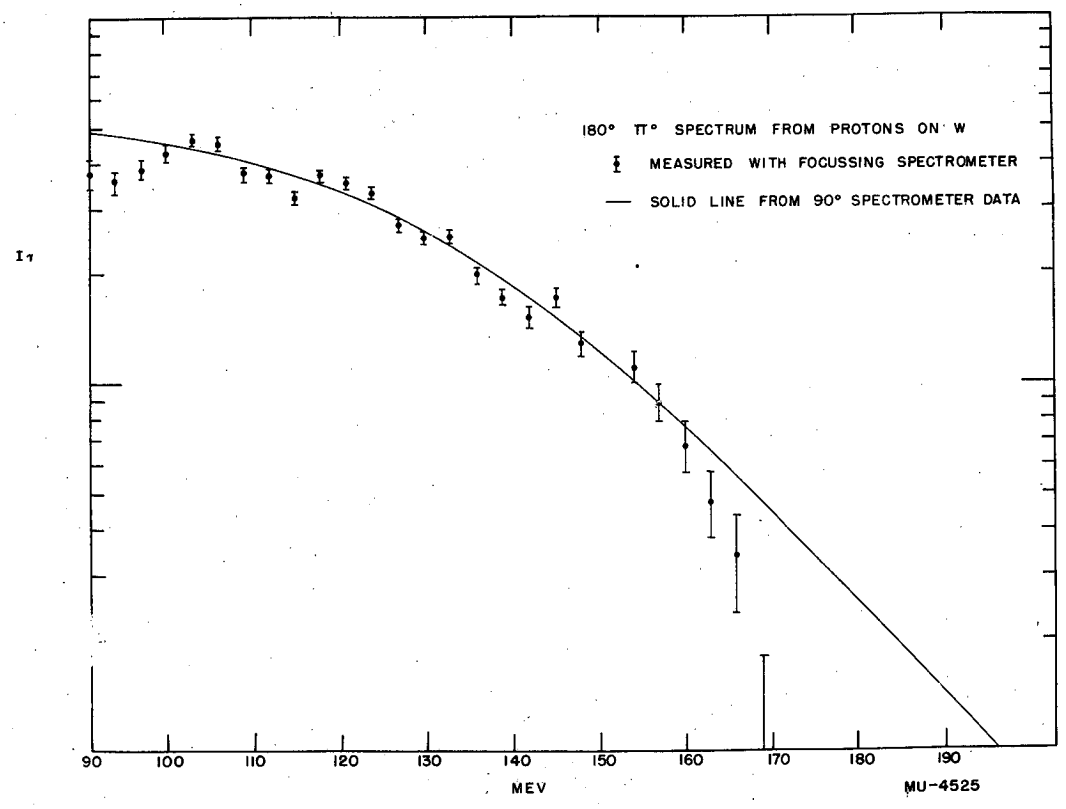
180° π° SPECTRUM FROM PROTONS ON W
MEASURED WITH FOCUSSING SPECTROMETER
SOLID LINE FROM 90° SPECTROMETER DATA
90
100
110
120
130
140
150
160
170
180
190
MEV
MU-4525

Fig. 66

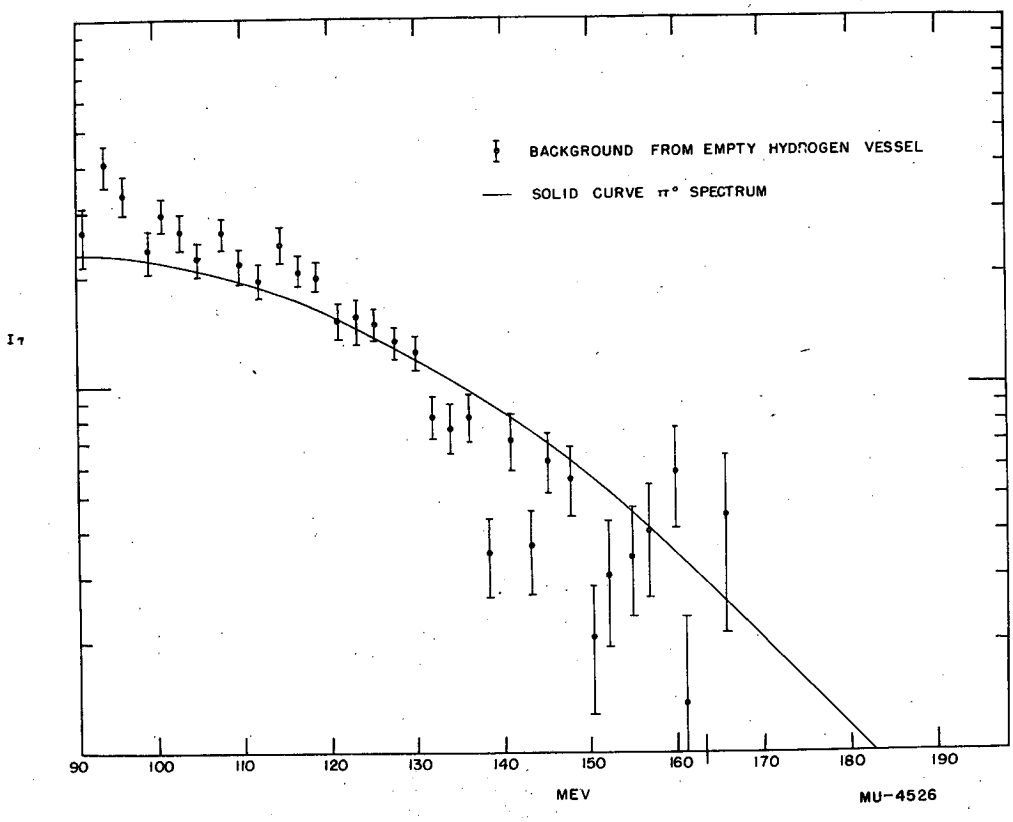
BACKGROUND FROM EMPTY HYDROGEN VESSEL
SOLID CURVE π° SPECTRUM
90
100
110
120
130
140
150
160
170
180
190
MEV
MU-4526

Fig. 67

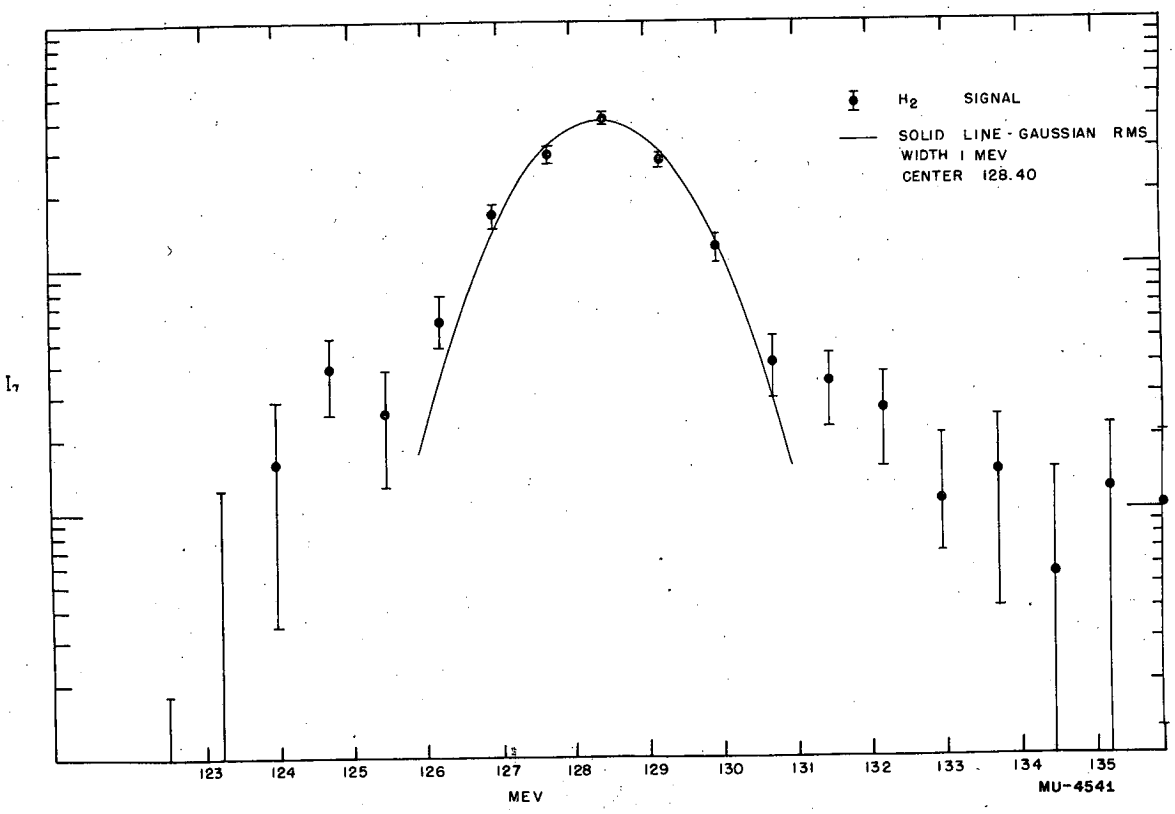
H_2 SIGNAL
SOLID LINE - GAUSSIAN RMS
WIDTH 1 MEV
CENTER 128.40
I_7
123
124
125
126
127
128
129
130
131
132
133
134
135
MEV
MU-4541

Fig. 68